ABSTRACT

Development of an Optical Cavity-based Biosensor for Point-of-Care Diagnostics

Donggee Rho, Ph.D.

Mentor: Seunghyun Kim, Ph.D.

An optical cavity-based biosensor (OCB) has been developed using a differential detection method towards point-of-care (POC) diagnostic applications. The optical cavity consisting of two partially reflective surfaces with a small gap was designed and optimized using a simulation tool, FIMMWAVE/FIMMPROP. The optical cavity samples were fabricated in the cleanroom by using simple and inexpensive processes. Lights from low-cost laser diodes pass through the fabricated cavity and reach a CMOS camera. As proof-of-concept tests, the refractive index measurements and the detection of biotinylated bovine serum albumin (BSA) were performed. Standard refractive index fluids were introduced to the cavity, then the changes in intensities of transmitted lights were measured by the camera. The measurement results matched up well with the simulation results. After the refractive index measurements, spin-on-glass layers were added for the surface functionalization, and the detection of biotinylated BSA with a concentration of 3 μM was performed in real-time. The detection results matched well with the simulation results, and the multiplexability of the OCB was discussed. To demonstrate the biosensing capability and experimentally determine the limit-of-

detection (LOD) of the OCB, streptavidin and C-reactive protein (CRP) detections were performed. The optical cavity design was optimized further, and the surface functionalization process was improved. The polymer swelling was effectively utilized to fine-tune the cavity width and increase the success rate in producing measurable samples. Four different concentrations of streptavidin were measured in triplicate with a LOD of 1.35 nM. Based on the streptavidin detection, biotinylated CRP antibody is employed as the receptor molecules, and the OCB successfully detected three different concentrations of human CRP with a LOD of 377 pM. By reducing the sensing area, improving the functionalization and passivation process, and increasing the sample volume, the LOD of the OCB can be further improved into the femto-molar range. The portability of the OCB was also demonstrated by building a stand-alone system and performing refractive index measurements. To improve the fabrication tolerance, the three-laser system was proposed and validated through refractive index measurements. Overall, the demonstrated capabilities and characteristics of the OCB in this dissertation show great potential to be used as a promising POC biosensor.

Development of an Optical Cavity-Based Biosensor for Point-of-Care Diagnostics

by

Donggee Rho, B.S.

A Dissertation

Approved by the Department of Electrical and Computer Engineering

Kwang Lee, Ph.D., Chairperson

Submitted to the Graduate Faculty of
Baylor University in Partial Fulfillment of the
Requirements for the Degree
of

Doctor of Philosophy

Approved by the Dissertation Committee

Seunghyun Kim, Ph.D., Chairperson

Enrique Blair, Ph.D.

Jonathan Hu, Ph.D.

Linda Olafsen, Ph.D.

Howard Lee, Ph.D.

Accepted by the Graduate School

December 2020

J. Larry Lyon, Ph.D., Dean

Page bearing signatures is kept on file in the Graduate School.

TABLE OF CONTENTS

LIST OF FIGURES

ACKNOWLEDGMENTS

Above all, I am very grateful to God for all the blessings during my Ph.D. study. I would like to express my sincere thanks to my advisor, Dr. Seunghyun Kim, for providing me an opportunity to step into a research field and work as a graduate research assistant. He has supported me with patience and provided not only financial assistance but also invaluable advice and professional guidance on research. Other than that, he has always helped me to learn about God's words or the right way to live as a Christian by spending his spare time. I would also like to thank my other dissertation committee members, Dr. Erik Blair, Dr. Jonathan Hu, Dr. Linda Olafsen, and Dr. Howard Lee, for the heartfelt advice and encouragement. I would like to thank my colleague, Caitlyn Breaux, for a cherished time spent together in the lab and working with me, especially in building a portable system and writing a review paper in charge of WGM-based biosensors. Lastly, I want to use this opportunity to thank my wife, Hwimin, and my family for their constant support, prayer, and love.

CONTRIBUTIONS

- Design and optimization of the optical cavity structure using FIMMWAVE/ FIMMPROP software.
- Development of the fabrication process for optical cavity samples.
- Proof-of-concept demonstrations of the optical cavity-based biosensor.
    - Refractive index detection.
    - Biotinylated BSA detection.
- Demonstration of biosensing capability of the optical cavity-based biosensor with limit-of-detection.
    - Streptavidin detection.
    - C-reactive protein biomarker detection.
- Experimental demonstration of the portable system through refractive index measurements.
- Design and demonstration of the three-laser system through refractive index measurements.
- First author of research articles published in journals.
    - D. Rho and S. Kim, "Low-cost optical cavity based sensor with a large dynamic range," *Opt Express*, vol. 25, no. 10, pp. 11244-11253, May 15 2017, doi: 10.1364/OE.25.011244.
    - D. Rho and S. Kim, "Label-free real-time detection of biotinylated bovine serum albumin using a low-cost optical cavity-based biosensor," *Opt Express*, vol. 26, no. 15, pp. 18982-18989, Jul 23 2018, doi: 10.1364/OE.26.018982.
    - D. Rho, C. Breaux, and S. Kim, "Demonstration of a Low-Cost and Portable Optical Cavity-Based Sensor through Refractive Index Measurements," *Sensors (Basel)*, vol. 19, no. 9, May 12 2019, doi: 10.3390/s19092193.

- D. Rho, C. Breaux, and S. Kim, "Label-Free Optical Resonator-Based Biosensors," *Sensors*, vol. 20, no. 20, 2020, doi: 10.3390/s20205901.
- (Submitted to journal) D. Rho and S. Kim, “Demonstration of a label-free and low-cost optical cavity-based biosensor using streptavidin and C-reactive protein.”

- First author of a conference proceeding.
  - D. Rho and S. Kim, “Large dynamic range optical cavity based sensor using a low cost three-laser system,” 2017 39th Annual International Conference Of The IEEE Engineering In Medicine And Biology Society (EMBC), Jeju, South Korea, July 10-15, 2017.
- Presentations at conferences.
  - D. Rho, J. Lichtenberg, and S. Kim, “Progress toward an optical cavity based sensor with a chained differential detection through refractive index measurements,” 2016 BMES annual meeting, Minneapolis, MN, USA, October 5-8, 2016.
  - C. Joy, D. Rho, and S. Kim, “Preliminary refractive index measurements in a portable optical cavity biosensor,” 2017 Biomedical Engineering Society Annual Meeting, Phoenix, AZ, October 11-14, 2017.
  - D. Rho and S. Kim, “Design and analysis of an optical cavity based biosensor using distributed Bragg reflectors,” 2017 Biomedical Engineering Society Annual Meeting, Phoenix, AZ, October 11-14, 2017.
  - C. Joy, D. Rho, and S. Kim, “Refractive Index Measurements Using a Portable Optical Cavity Biosensor System,” Pittcon 2018, Orlando, FL, USA, Feb 26 – Mar 1, 2018.
  - D. Rho and S. Kim, “Detection of biotinylated BSA with an optical cavity-based biosensor,” Pittcon 2018, Orlando, FL, USA, Feb 26 – Mar 1, 2018 (accepted for oral presentation).
  - C. Joy, D. Rho, and S. Kim, “Biotinylated BSA detection using a portable optical cavity biosensor,” 2018 Biomedical Engineering Society Annual Meeting, Atlanta, GA, October 17-20, 2018.

- D. Rho and S. Kim, “Experimental demonstration of an improved optical cavity-based biosensor through biotinylated BSA detection,” 2018 Biomedical Engineering Society Annual Meeting, Atlanta, GA, October 17-20, 2018.

CHAPTER ONE

Biosensors

Since Leland C. Clark developed the first glucose biosensor in 1962, there have been many efforts to advance biosensor technologies, which stimulates tons of related researches to be launched and progressed [1]. The high and increasing demand for the biosensor research is reflected in the market value, expected to grow up to $31.5 billion by 2024 [2]. Biosensors are employed in a wide range of applications including mainly medical diagnostics, food and environment monitoring, development of drug and vaccine, and military [2-4]. For example, biosensors in the medical field play a crucial role by facilitating early and accurate diagnoses of diseases, such as cancers, cardiovascular diseases, and infectious diseases, and enabling to initiate effective treatments for patients [5-7].

A biosensor is defined as an analytical device used for the identification and quantification of the target biological analyte in a sample fluid by converting a biological reaction into a readable signal. It consists of three elements, bioreceptor molecules, a transducer, and a readout element as shown in Figure 1.1 [8]. The bioreceptor, the biological recognition element, is selectively chosen to have an affinity to a target analyte in a sample fluid. It can be mainly classified into four groups, enzymes, cells, antibodies, and nucleic acids, which are discussed in the section 1.1. For medical diagnostics, the target analyte is present in biological samples such as blood, serum, plasma, urine, and cerebrospinal fluid (CSF) and often called a biomarker. A medical biosensor detects and

quantifies the presence of biomarker to monitor or diagnose a certain disease. For example, Figure 1.2 shows some of biomarkers and corresponding cancers [7]. Prostate-specific antigen (PSA) is one of the first biomarkers identified for diagnosis of prostate cancer. Most of men without prostate cancer have a concentration of PSA under 4 ng/mL in blood, so many doctors recommend further detailed tests if the level is measured higher than that to confirm the presence of cancer [7, 9].

When the target analyte in a sample fluid selectively interacts with the functionalized bioreceptor, the transducer converts a signal produced from the interaction into a signal measurable by a readout element. The commonly employed transducers can be classified into four groups, electrochemical, acoustic, calorimetric, and optical transducers, which are discussed in the section 1.2. The measured signal is lastly processed and analyzed in the readout element to determine the presence of the target analyte and further quantify its concentration.

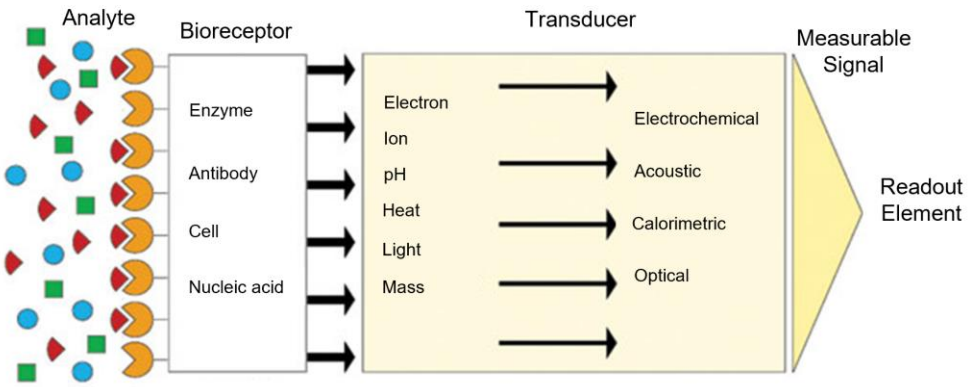

Figure 1.1. Schematic diagram of a biosensor [8]. Reproduced from the image downloaded from the website (www.slideshare.net).

Type of cancer	Biomarker
Breast	BRCA1, BRCA2, CA 15-3, CA 125, CA 27.29, CEA, NY-BR-1, ING-1, HER2/NEU, ER/PR
Colon	CEA, EGF, p53
Esophageal	SCC
Liver	AFP, CEA
Lung	CEA, CA 19-9, SCC, NSE, NY-ESO-1
Melanoma	Tyrosinase, NY-ESO-1
Ovarian	CA 125, HCG, p53, CEA, CA 549, CASA, CA 19-9, CA 15-3, MCA, MOV-1, TAG72
Prostate	PSA

Figure 1.2. Biomarkers for different types of cancer [7]. Reproduced from Open Access article with Copyright © 2011 Bohunicky and Mousa, publisher and licensee Dove Medical Press Ltd.

1.1.Bioreceptors

A bioreceptor is a biological recognition element of a biosensor to recognize and capture the target analyte in a sample fluid [10-17]. The recognition event at the bioreceptor produces a signal detectable by a transducer. Commonly used bioreceptors are enzymes, antibodies, cells, and nucleic acids.

1.1.1. Enzyme

An enzyme is a biological catalyst speeding up the rate of a specific chemical reaction, which catalytically converts a substrate, the target analyte, into a detectable product [10-12]. Enzymes are usually highly specific to the corresponding substrates based on their complementary structures. The enzyme-substrate interactions do not require the consumption of enzyme, which helps to be reusable and produce a large number of reactions. These advantages enable enzymes to be widely employed as an efficient bioreceptor for biosensor research. For example, the glucose biosensor is one of the most extensively developed and commercialized enzyme-based biosensors for diabetes patients. Figure 1.3 shows the schematic diagram of a glucose biosensor utilizing

the immobilized enzymes, glucose oxidase (GO_x). When glucose introduced through the inlet encounters the immobilized GO_x, it is oxidized by the enzymatic reaction consuming oxygen and producing gluconic acid with hydrogen peroxide, which can be monitored to determine the glucose level.

Some limitations on enzymes exist regarding the stability affected by environmental conditions such as pH and temperature. The lifetime and performance of enzyme-based biosensors is directly related with the bioreceptor stability.

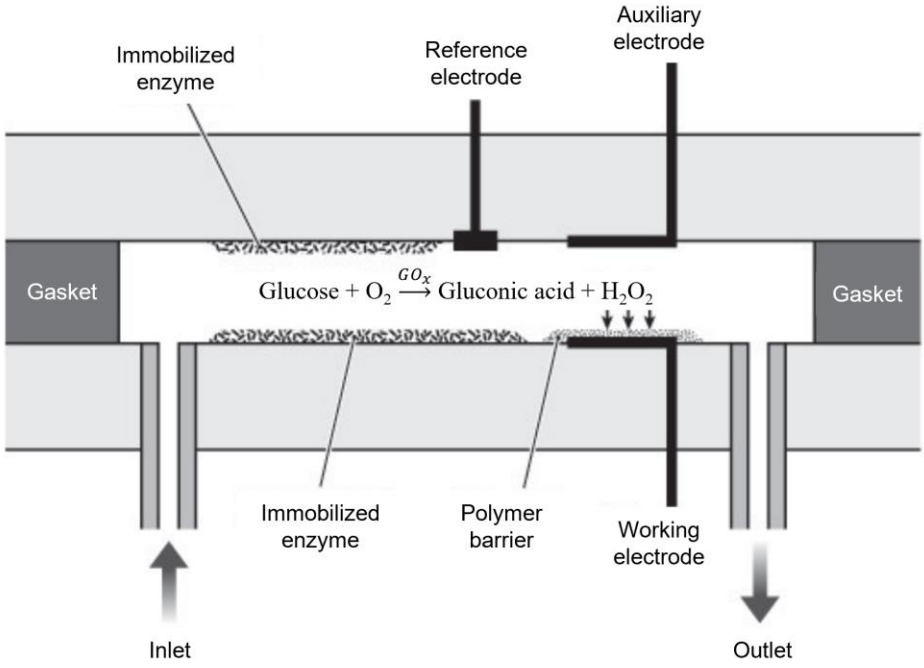

Figure 1.3. Schematic diagram of an enzyme-based glucose biosensor [12]. Reproduced with permission from Caister Academic Press.

1.1.2. Antibody

An antibody, known as an immunoglobulin (Ig), is a protein mainly produced by plasma cells when the immune system responses to the presence of a foreign substance, an antigen. It has a Y-shaped conformation, and each tip contains a paratope, an antigen-binding site, specifically recognizes a particular epitope on an antigen. Therefore, the

antibody-antigen interactions usually show high affinity and high selectivity, which is widely employed in developing a biosensor. For instance, Figure 1.4 shows the schematic of a microcantilever biosensor with the immobilized antibodies on the gold surface to detect prostate-specific antigen (PSA), which is a well-known biomarker of the prostate cancer [18]. As PSA molecules adsorb to the anti-PSA antibodies immobilized on the surface, it generates motion and deflections of the cantilever, which are optically measured.

There are some drawbacks for the use of antibody as a bioreceptor. The antibody preparation including isolations and purifications usually involves costly and time-consuming processes. Also, the antigen-antibody interactions are naturally irreversible, and the binding efficiency is highly dependent on the orientation of immobilized antibodies.

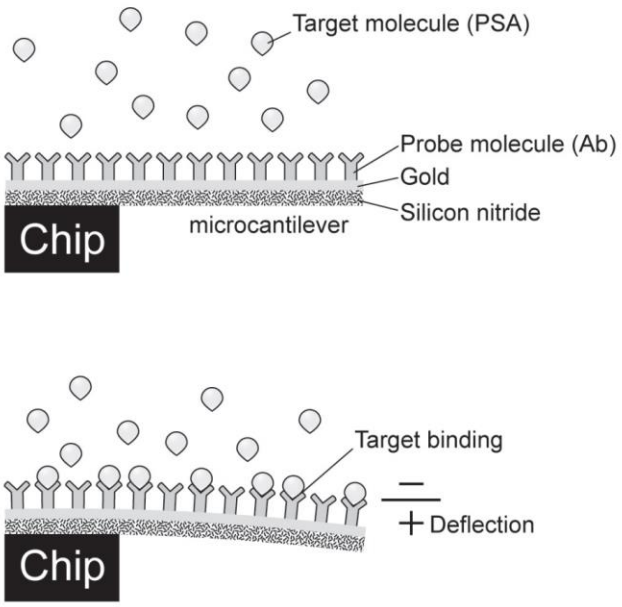

Figure 1.4. Schematic diagram of a microcantilever biosensor with the immobilized antibodies [12]. Reproduced with permission from Caister Academic Press.

1.1.3. Cell

Living cells can be also employed as a biorecognition element of a biosensor [13-15]. Compared to enzymes and antibodies, the preparation of cells requires less effort and expenses without purifications, and the immobilized cells have longer lifetime and more tolerance to be active in a wide range of pH and temperature. The advantages of cell-based biosensors help to be used in variety of applications such as drug screening, environmental monitoring with toxicity assessment, and medical diagnostics. For example, Figure 1.5 shows different types of cell sources and corresponding functional strategies for various applications [14].

Although cells have unique characteristics compared to other molecular bioreceptors, cell-based biosensors have not been popular with some disadvantages including complex structures, long response times, low sensitivity and selectivity, and challenging immobilization methods.

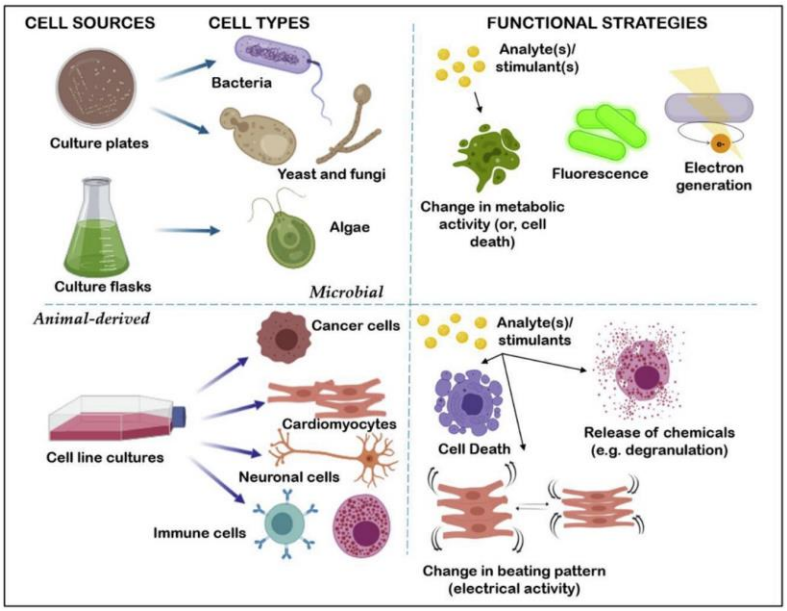

Figure 1.5. Schematic of different cell types (left) and functional strategies (right) for cell-based biosensors. Reproduced from ref. [14] with permission from Elsevier.

1.1.4. Nucleic Acid

A nucleic acid is a chain of nucleotides storing the genetic information in living organisms and transferring it to the next generation. It includes deoxyribonucleic acid (DNA) and ribonucleic acid (RNA). Nucleic acid-based biosensors usually immobilize short DNA or RNA fragments on the transducer surface to detect the complementary target sequence via molecular hybridization [10, 16, 17]. The hybridization event is monitored to determine the presence of target DNA/RNA and its concentration with high specificity and strong affinity. For example, Figure 1.6 shows the schematic of a nucleic acid-based biosensor. The immobilized DNA specifically detect the target DNA sequence, and the current change through the hybridization is measured.

In addition to provide high sensitivity and selectivity, the hybridization is a reversible binding, so nucleic acid-based biosensors can be reusable. However, the applications are only limited to the detection of nucleic acids, and the preparation of a specific nucleic acid probe corresponding to the target sequence can be challenging.

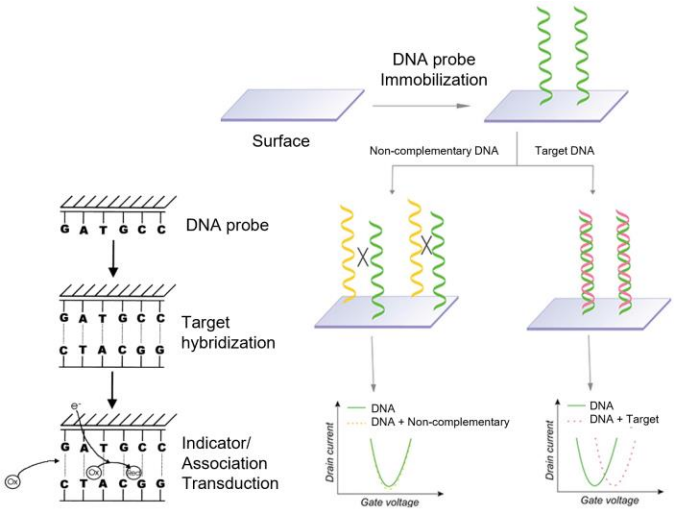

Figure 1.6. Binding between immobilized DNA probe and target DNA sequence via hybridization event leading to current response. Reproduced from refs. [16, 17] with permission from Elsevier.

1.2.Transducers

A transducer of a biosensor system converts the signal generated from the interactions between bioreceptors and target analytes into a measurable signal [19-28]. The signal produced by a transducer can be further processed and analyzed to determine the presence of the target analyte in a sample fluid and quantify the level of it. For the last decade, the most widely employed transducers in biosensor technologies are divided into four groups including electrochemical, acoustic, calorimetric, and optical transducers.

1.2.1. Electrochemical

An electrochemical transducer is based on measuring changes in electrical properties such as current, potential, conductivity, impedance, and field-effect between electrodes [19-21]. Electrochemical transducers normally utilized enzymes as a biorecognition element functionalized on the electrode surface, which involves the production or consumption of electrons or ions during the reaction with target analytes. The electrochemical sensor usually consists of three electrodes, a reference electrode (RE), a working electrode (WE), and a counter electrode (CE). The reference electrode has a known potential used as a point of reference, and the reaction of interest occurs at the surface of the working electrode, which is in conjunction with the counter electrode allowing the current flow. Since the electrode has played an important role in electrochemical transducers, the sensing performance is dependent on the material type, dimensions, and surface characteristics of the electrode. Silver, gold, platinum, carbon materials, and silicon compounds are commonly selected as the electrode material to have conductivity and stability.

For example, Figure 1.7 shows the schematic of the first glucose biosensor using an amperometric transducer developed by Clark and Lyons [22]. The device has two electrodes, a platinum (Pt) WE and a silver/silver chloride (Ag/AgCl) RE. Glucose introduced into a dialysis membrane reacts with the immobilized enzymes, GO_x, on the platinum electrode surface. The enzymatic reaction produces gluconic acid with hydrogen peroxide and consumes the oxygen at the WE leading to a decrease in the current flowing. The current proportional to the oxygen concentration is monitored to determine the glucose level of the medium outside the dialysis membrane.

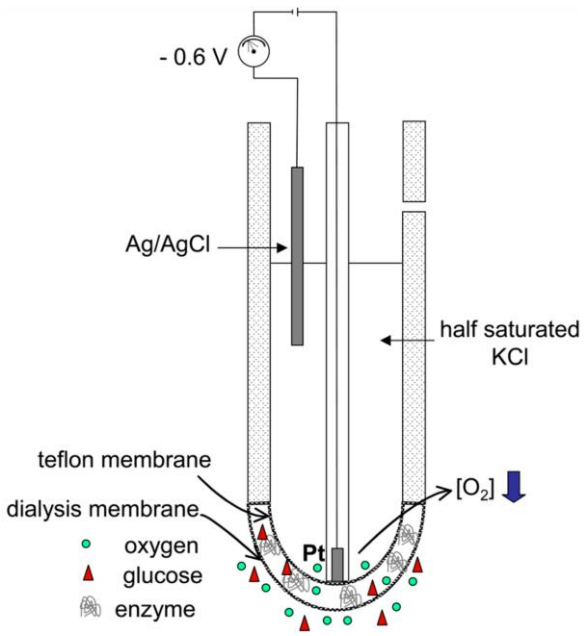

Figure 1.7. Schematic diagram of Clark's glucose amperometric electrode [22]. Reproduced from Open Access article (MDPI).

1.2.2. Acoustic

An acoustic transducer detects changes in physical properties of a surrounding medium utilizing mechanical or acoustic waves [23, 24]. Most of acoustic transducers employ piezoelectric crystals, which produces oscillations at a certain frequency in

response to the applied electric field. The oscillation frequency is sensitive to the change in mass of the crystal. As the target biomolecule adsorb to the crystal surface, the increased mass from the binding causes the frequency to be shifted, which can be analyzed to determine the level of target molecules. Anisotropic crystals without a center of symmetry usually experiences the piezoelectric effect to the mechanical stress, such as quartz, zinc oxide, synthesized lithium niobate, and lithium tantalite. Among them, quartz is the most popularly used for acoustic transducers due to its low-cost from the natural abundance, ease of use, stability, and robustness.

For instance, a quartz crystal microbalance (QCM) is one of the most common acoustic-based biosensors, which measures a mass change on a quartz crystal plate by measuring the frequency shift [25, 26]. A recently developed QCM is described in Figure 1.8 showing the immobilized molecules on a quartz crystal plate for the detection of CD63 exosome. The frequency shift was measured in real-time as the exosome adsorbs to the surface followed by buffer rinse, and the dissipation factor was also measured to analyze the viscoelastic properties of the target analyte.

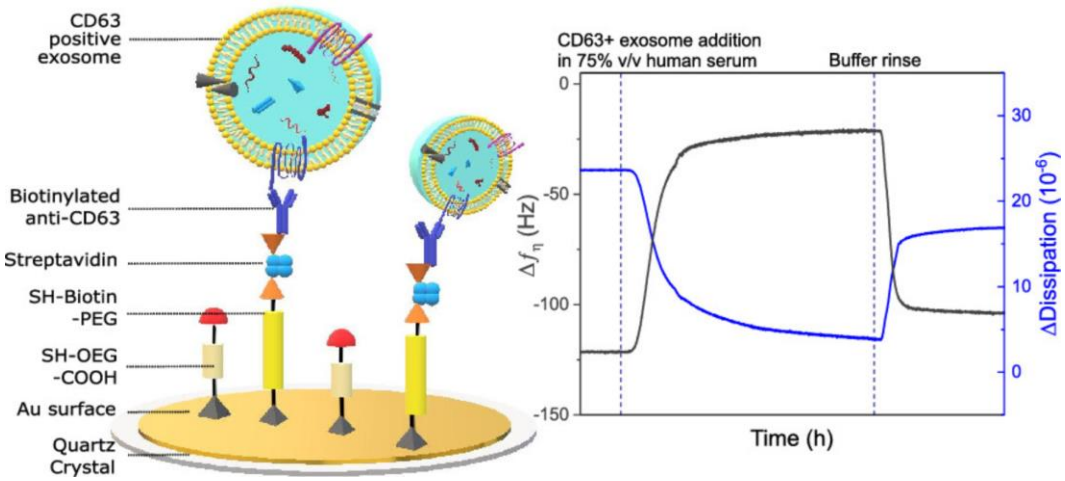

Figure 1.8. Schematic of QCM for the detection of CD63 exosome and corresponding frequency shift. Reproduced from ref. [25] with permission from ACS Publications.

1.2.3. Calorimetric

A calorimetric (thermal) transducer detects the temperature change resulting from the heat absorption or production during the interactions between bioreceptors and target analytes [27, 28]. The temperature changes can be measured by a thermistor or a thermopile and analyzed to determine the concentration of the analyte. For instance, the enzymatic reactions generally release heat into the surrounding medium, which was utilized to develop an enzyme thermistor described in Figure 1.9 [28]. The system is insulated using a polyurethane foam to maintain the temperature inside. A buffer solution is introduced by a peristaltic pump, and a sample fluid is introduced through a injection valve. There are two columns where the fluids passing through, a column with immobilized enzymes, and a reference column. The change in temperature of the column is measured by the connected thermistor.

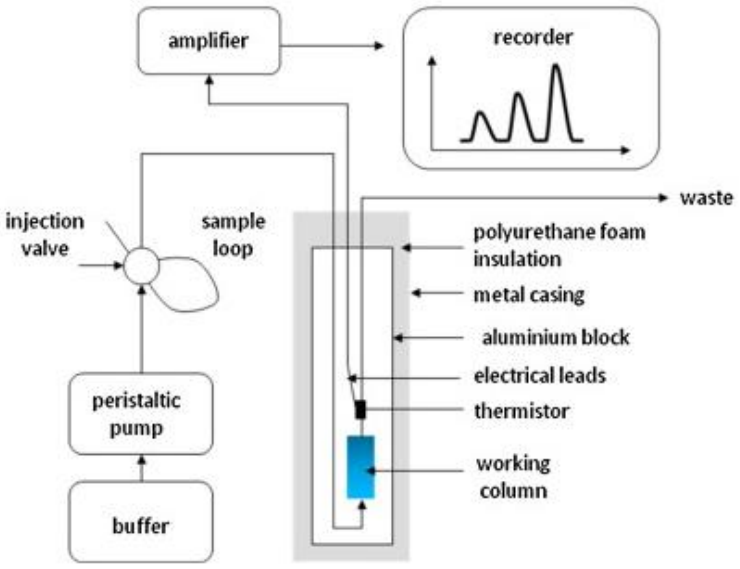

Figure 1.9. Schematic of a conventional enzyme thermistor. Reproduced from ref. [28] with permission from Elsevier.

1.2.4. Optical

An optical transducer utilizes the behaviors of light including fluorescence, luminescence, reflection, refraction, absorption, or interference. Due to the advantages including high sensitivity and selectivity, the optical transduction method is widely and extensively employed in biosensor research. Out of many biosensors employing optical transducers, Enzyme-linked immunosorbent assay (ELISA) and surface plasmon resonance (SPR) are the two most well developed and commercialized biosensors. These two types of biosensors will be discussed in depth in the following section, and in addition to them, optical resonator-based biosensors will be described.

1.3.Optical Biosensors

Optical biosensors can be generally categorized into two groups, labeled and label-free detection methods. Fluorescence or luminescence labeling techniques help to enhance the signal produced by the interactions between the bioreceptor and target biomolecules. For instance, as the most popular format of label-based biosensor, the enzyme-linked immunosorbent assay (ELISA) technique will be discussed further in the first subsection.

In contrast, label-free biosensors allow direct detection of the target analytes which are not labeled or modified. By removing the labeling process, label-free detection can reduce overall time and cost and enable the real-time detection of target molecules. Many optical label-free biosensors are based on the refractive index change induced by the biomolecular interactions, which is correlated with the concentration of the target analyte in the sample. Some of the widespread optical structures utilizing the refractive

index detection including surface plasmon resonance (SPR) and optical resonators will be explained in detail in subsequent sections.

1.3.1. Enzyme-linked Immunosorbent Assay (ELISA)

An ELISA is a commonly used laboratory technique to determine the presence or concentration of a target protein in the sample [29, 30]. ELISA is based on the specificity of the antibody-antigen interaction and the sensitivity of the enzyme reaction. The configuration of ELISA is typically a plate containing 96 wells arranged into 8 rows and 12 columns. Figure 1.10 represents the general process of performing an ELISA test [29]. As the first step, the desired antigen is immobilized on the plate wells, and the coated plate is incubated for a long enough time to improve the adsorption. After coating the plate, a blocking buffer is added in order to cover any nonspecific binding sites and prevent incorrect test results. The immobilized antigens have high affinity with the antibody and specifically bind to added primary antibodies, which are unlabeled. Then, the plate is incubated for enabling primary antibodies to fully bind to antigens at room temperature. An excess of unbound antibodies is washed away with a buffered solution. The secondary antibody conjugated with an enzyme is introduced to the plate and recognizes the primary antibody. The incubation process to improve the binding between primary and secondary antibodies is conducted, and the rinsing step is repeated once more. Next, a chromogenic substrate, which is the chemical compound reacting specifically with the enzyme linked in the secondary antibody, is added to the sample solutions. The enzymatic reaction occurs with a visible color change, which indicates the presence of the target protein in the sample and subsequently allows the quantification of

it. Lastly, the plate is placed in the microplate reader to determine the concentration of the protein of interest by measuring the changed color of the sample wells.

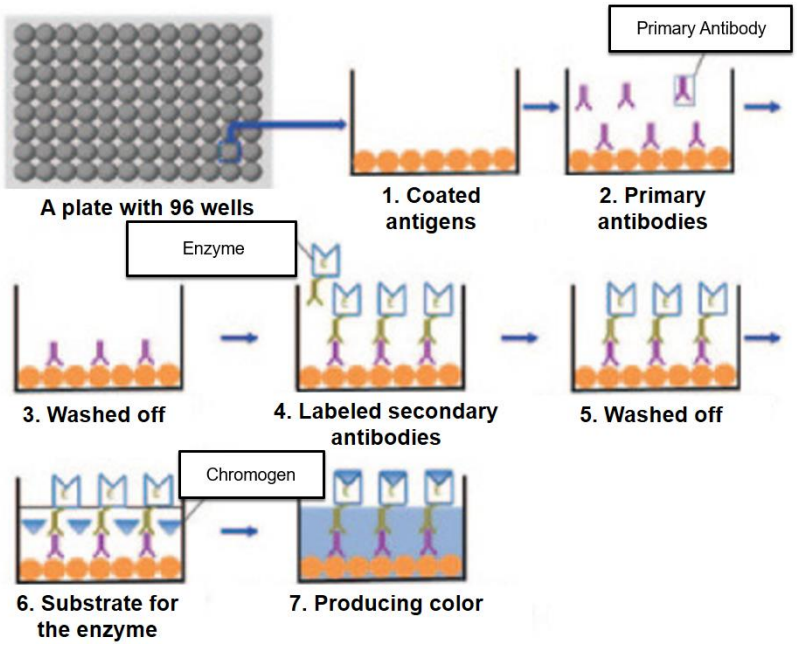

Figure 1.10. Overall procedure of ELISA. Reproduced from ref. [29] with permission from Elsevier.

There are generally four types of ELISA methods depending on the modification of the general procedure as represented in Figure 1.11 [31]. The ELISA process described in Figure 1.10 represents the indirect ELISA detection method quantifying the concentration of the immobilized antigen by using two binding process with different kinds of antibodies, which are unlabeled primary antibodies and enzyme-coupled secondary antibodies. This type of assay is the most common format of ELISA due to its several advantages. The target antigen which is bound by the primary antibody can be detected by more than one labeled secondary antibody, and this makes possible to achieve high sensitivity with the indirect detection method. However, using secondary antibody may cause the nonspecific signal from cross-reactivity [32]. On the other hand,

the immobilized antigen can be detected by the enzyme-conjugated primary antibody without adding secondary antibody, and this method is called direct ELISA. Compared to the other types of ELISA, the direct ELISA is simply and quickly performed since it requires only one antibody and fewer preparation steps. However, it has lower sensitivity and worse flexibility than the indirect detection method.

When the target antigen is not adhesive to the plate wells or not sensed at high level, the sandwich ELISA can be used. The sandwich ELISA technique is used to quantify the sample antigen which is bound between two antibodies as its name implies. The capture antibody is immobilized on the plate first, and the solution containing desired antigens is added. Then, a specific primary antibody is applied so that the antigen is sandwiched between two antibodies. Following that, the enzyme-labeled secondary antibody is added as the detection antibody and bound to the sandwiched molecular complex. By using two antibodies bound to the target antigen, the sandwich ELISA can achieve high sensitivity and specificity. At the same time, however, this type of ELISA requires two matched pair of antibodies to make the sandwich complex. The sandwich ELISA has another benefit in terms of preparing tested samples since the antigen does not need to be purified.

The last type of ELISA uses competitive binding between the target antigen in the sample and the immobilized antigen, so it is called competitive ELISA. The desired antigens are coated on the plate wells, and the incubated sample with the primary antibody is applied. Then, the more antigen of interest bound with the primary antibody during the sample incubation, the less primary antibody can be bound to the antigen in the well. After eliminating any unbound antibody-antigen complexes, the enzyme-

conjugated secondary antibody is added. Therefore, the weaker fluorescent signal indicates the higher concentration of the target antigen in the sample. The main advantage of competitive ELISA is that impure samples can be used.

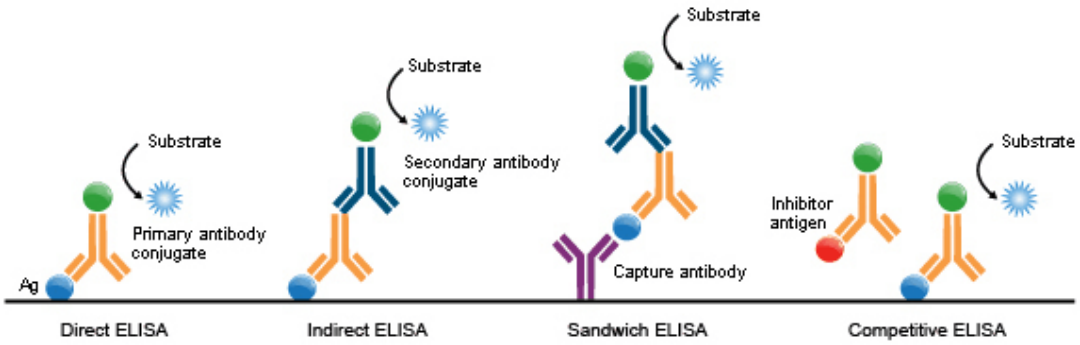

Figure 1.11. Types of ELISA methods [31]. Reproduced from the image in the Abnova webpage.

ELISA has been considered as a standard method for identifying and quantifying the target analyte with high sensitivity and specificity, including antigens/antibodies, proteins, and hormones [33, 34]. For instance, ELISAs are variously used not only to determine the concentration of cancer biomarkers but also to detect potential food allergens and infectious diseases including HIV and cholera [29, 35]. For example, ELISA kits are usually accepted for PSA detection providing sensitive and reliable diagnosis. Commercial ELISA products from many diagnostics companies, including Abbot Diagnostics, Bio-rad, and Roche, are able to detect the level of PSA in a range of between 0.05 to 0.005 ng/mL [32, 36]. However, these tests involve laborious and time-consuming preparation steps with sophisticated and costly instruments that need to be operated by a trained expert working in a centralized clinical laboratory [34, 37-41].

1.3.2. Surface Plasmon Resonance (SPR)

Since the first surface plasmon resonance (SPR) biosensor was demonstrated in 1983 by Liedberg, Nylander, and Lundström, this unique optical transduction method has been widely developed, commercialized, and used as a powerful biosensing platform due to its great advantages such as high sensitivity, high specificity, label-free detection, and real-time monitoring [42-44].

The SPR biosensors exploit the excitation of surface plasmons which are electron oscillations at an interface between a metal (e.g. gold or silver) and a dielectric material [42, 45-47]. The oscillation of free electrons creates a surface plasmon wave which travels along the metal-dielectric interface. The intensity of the propagating electromagnetic wave reaches the maximum at the interface and falls off exponentially away from the surface. This surface plasmon waves can be excited by an incident light wave when the parallel component of light's wave vector matches with the wave vector of the surface plasmon waves. In order to excite the surface plasmon waves by using photons, it requires a certain coupling medium such as a prism, an optical waveguide, or a grating structure. Especially among the prism-based SPRs which are developed by Kretschmann and Otto, the Kretschmann configuration is the most widely used for the excitation of the plasmon wave.

Figure 1.12 represents the schematic illustration of the Kretschmann configuration based SPR sensor utilizing the phenomenon of total internal reflection [48]. An incident light wave is propagated through a high refractive index prism, and the light is then totally reflected at the interface between a thin metal layer and a prism coupler generating an evanescent field into the gold layer. When the surface-parallel wave vector

of the incident light matches with the wave vector of the plasma wave by varying the angle of incidence or the wavelength of the light, the surface plasmon resonance is induced at the metal surface, resulting in energy absorption from the incident light. Therefore, the intensity of reflected light is greatly attenuated at a certain incident angle, which is called the SPR angle, and wavelength where the resonance condition is fulfilled. The intensity of the resulting reflected light is continuously measured in terms of the angle of incidence or the wavelength with a detector [46, 49].

The SPR condition is extremely sensitive to the refractive index change of the dielectric material in the immediate vicinity of the metal surface. The biomolecular interaction between the immobilized receptors on the gold layer and the target analyte in the sample causes an increase in the refractive index, which leads to the changed wave vector of the surface plasmon wave. The wave vector of the light can be then readjusted to match with the plasmon wave vector by changing the incident angle or the wavelength of reflected light. This causes the angle (or the wavelength) at which the minimum intensity occurs to be shifted as shown in a sensorgram representing measured intensities with respect to incident angles shown at the bottom left in Figure 1.12. As a result, the change in the SPR angle is directly proportional to the concentration level of the target analyte in the sample.

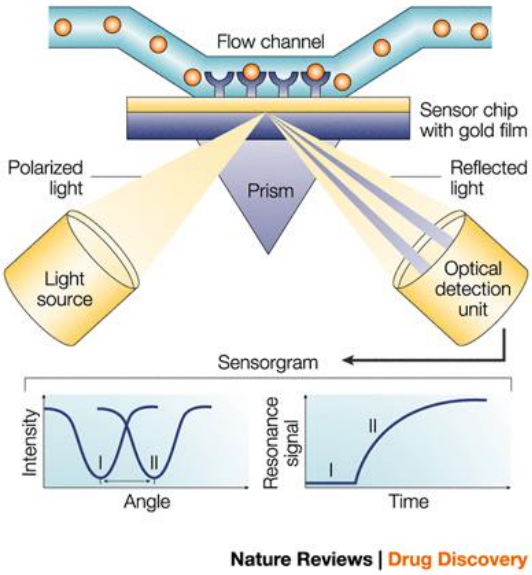

Figure 1.12. General schematic (above) and sensorgram (below) of the prism-based SPR. Reproduced from ref. with [48] permission from Springer Nature.

For the further analysis of the binding interaction, SPR technique allows the real-time monitoring with a sensorgram represented in Figure 1.13. One change of resonance signal, the y-axis of the sensorgram, usually corresponds to the shifted SPR angle of 10^{-4} degree (^{o}). By monitoring and analyzing this graph, the association rate, the dissociation rate, the affinity of interaction, and the concentration of the analyte can be determined [50, 51]. The conventional prism-based SPR sensors are able to detect 1pg/mm^2 of the target analyte and 5 x 10^{-7} of refractive index unit (RIU) change near the surface [49, 52, 53].

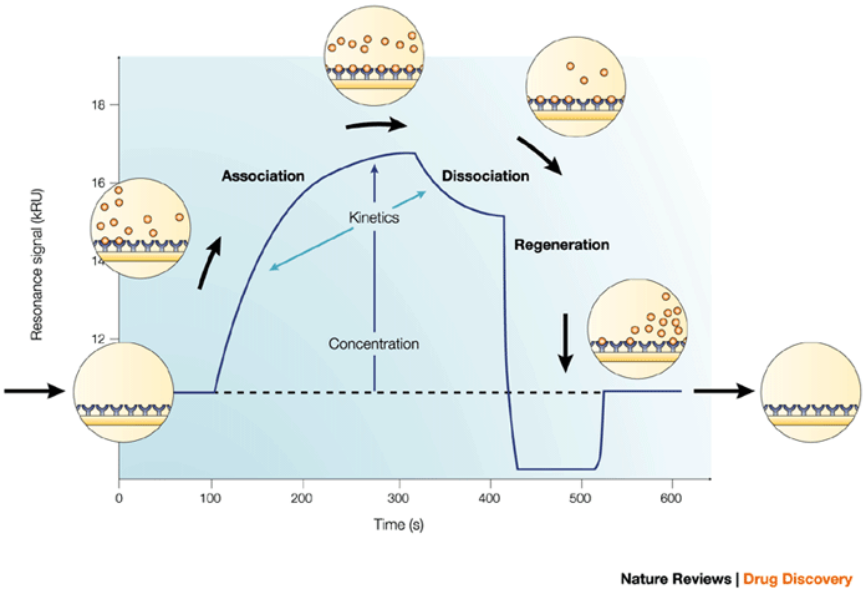

Figure 1.13. Sensorgram representing a binding cycle in SPR. Reproduced from ref. with [48] permission from Springer Nature.

SPR-based biosensors are attractive because of its label-free operation and real-time analysis capability [43, 44, 48, 54-56]. They detect biomolecular interactions occurring on the metal surface with high sensitivity by measuring the shift in the excitation angle of surface plasmon or the optical intensity change. Nonetheless, it requires complicated and expensive settings [57] limiting the possibility to miniaturize the system [42, 58].

CHAPTER TWO

Optical Resonator-based Biosensors

This chapter published as: D. Rho, C. Breaux, and S. Kim, "Label-Free Optical Resonator Based Biosensors," *Sensors*, vol. 20, no. 20, 2020, doi: 10.3390/s20205901 [59].

Optical resonator-based biosensors are actively investigated to achieve a highly sensitive detection down to single bio-molecule interactions without labeling [60-62]. Optical resonators are inherently sensitive to the changes in the surrounding environment due to their strong light confinement capability and resonance characteristics [63]. With the recent development in microfluidic platforms and microfabrication technologies, optical resonator-based biosensors are further miniaturized [64] and regarded as a promising point-of-care (POC) device platform for the early and highly accurate detection of diseases. POC devices allow medical diagnostic tests to be conducted at or near the patients, which eventually increases the chance of early detection of diseases and satisfies the need for in-home healthcare and resource-limited settings [65]. To be effectively used in POC diagnostics, the biosensor must have several characteristics such as label-free detection, low-cost, high sensitivity, high selectivity, simultaneous detection capability of multiple analytes with a small sample volume, and portability [65].

Optical resonator-based biosensors are categorized into two groups, Fabry-Perot Interferometer (FPI)-based biosensors and whispering gallery mode (WGM)-based biosensors, based on the light confinement mechanism [66]. FPI-based biosensors are divided into three sections: (1) FPI with two reflecting surfaces, (2) porous silicon microcavity (PSM), and (3) optical fiber-based FPI. WGM-based biosensors are

categorized into (1) ring and disk resonators, (2) spherical resonators, (3) toroid resonators, and (4) cylindrical or capillary based resonators.

An optical resonator is designed to allow light waves at specific (resonant) frequencies to be confined and stored within the cavity structure [42, 67, 68]. Light waves continuously travel back-and-forth in between two or more interfaces or circulate within the optical resonator structure. At resonant frequency, light waves constructively interfere without suffering significant losses, while light waves at other frequencies are suppressed with destructive interference. The resonant frequencies are determined by the material and geometry of the optical resonator. They are highly sensitive to changes in the temperature, pressure, and refractive index of the surrounding medium. The sensitivity of an optical resonator-based biosensor is related with the sharpness of resonance response which is expressed as the quality factor (Q-factor) of an optical resonator. The Q-factor is defined as

$$\mathrm{Q} = \frac{v_m}{\Delta v} \tag{2.1}$$

where v_m is the resonant frequency and Δv is the full width at half maximum (FWHM) at the resonant frequency [69]. For a specific resonant frequency, the Q-factor increases as the width of the resonant curve is reduced.

For an optical resonator to be used as a biosensor, a bio-recognition element or a bioreceptor, which has a specific affinity to an analyte of interest in a biological sample fluid, is functionalized on it. As the target analytes in a sample fluid attach to the bioreceptor, the effective refractive index of surrounding medium is changed, resulting in a shift in the resonant spectrum. Either a shift of the resonant peak or a change in light

intensity is measured with a readout element to quantify the concentration of the analyte in a sample medium and determine the binding kinetics from a real-time detection data.

Two measures, sensitivity and limit of detection (LOD), are commonly used to determine the quality of an optical resonator-based biosensor. The sensitivity (S) is the amount of shift in resonant frequency (or wavelength) per change in refractive index or molar concentration and calculated by

$$\mathrm{S} = \frac{\Delta\lambda}{\Delta n} \left[\frac{nm}{RIU}\right] \tag{2.2}$$

where $\Delta\lambda$ is the shift in resonant wavelength and Δn is the change in refractive index (RIU: refractive index unit).

The LOD is the minimum detectable concentration of a biosensor. If it is not experimentally determined, the LOD is often estimated. The way to estimate the LOD may differ depending on the signal to noise ratio and governing entity in the respective field of the work [70], but, for the most cases, the LOD of a biosensor is estimated using the standard deviation (σ) by

$$LOD = 3 * \sigma \tag{2.3}$$

while some variations include a coefficient of 3.3 in the place of 3 as suggested by the International Organization for Standardization (ISO), and LCGC Europe [71].

2.1. Fabry-Perot Interferometer (FPI)-based Biosensors

The FPI, called an etalon or an optical cavity, has the simplest structure out of many different geometries of the optical resonators, confining the light between two parallel reflecting surfaces. The simple structure of the FPI allows to be easily combined with a microfluidic system and integrated with other optical materials or components

such as a porous silicon or an optical fiber [72-74]. FPI-based biosensors boast a high sensitivity compared to other interferometric biosensors based on Mach-Zehnder and Michelson interferometers due to its resonance characteristic through a large number of reflections [75, 76].

The incident light onto the FPI undergoes multiple reflections and transmissions at two reflecting surfaces, creating numerous reflected and transmitted waves as shown in Figure 2.1(a).

The transmittance (T) of the optical cavity can be represented as

$$\mathrm{T} = \frac{I_t}{I_i} = \frac{(1-\mathrm{R})^2}{(1-\mathrm{R})^2 + 4\mathrm{R}\sin^2\left(\frac{\delta}{2}\right)} \tag{2.4}$$

where I_t and I_i are the transmitted intensity and incident intensity, respectively, and R is the reflectance of the surfaces, assuming the reflectance of the reflecting surfaces are the same. The phase difference (δ) is given by

$$\delta = \left(\frac{2\pi}{\lambda}\right) \cdot 2nl\cos\theta \tag{2.5}$$

where λ is the wavelength of light in vacuum, n is the refractive index inside the optical cavity, l is the distance between reflecting surfaces, and θ is the angle of the light propagating inside the cavity. If the phase difference is equal to an integer multiple of 2π, the transmittance becomes maximized where the constructive interference occurs. However, the transmitted waves will destructively interfere with each other when the phase difference becomes an odd integer multiple of π, leading to the minimized transmittance. Therefore, the transmission spectrum as a function of the wavelength

shows a cyclic resonance characteristic with peaks and valleys as represented in Figure 2.1(b).

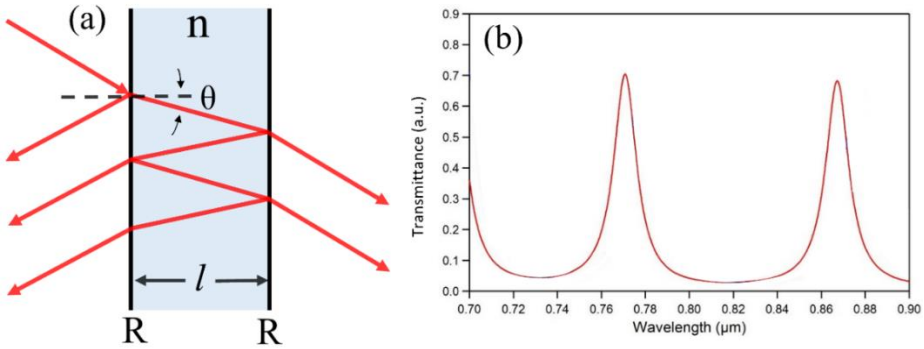

Figure 2.1. (a) Structure of FPI. (b) Transmission spectrum of FPI.

Under normal incidence, the resonant frequencies (v_m) can be calculated by

$$v_m = \frac{c}{2nl} m \tag{2.6}$$

where c is the speed of light in vacuum and m is the integer, which represents the resonator- mode order. The corresponding free spectral range (FSR), the peak-to-peak separation, is also obtained as

$$\mathrm{FSR} = v_{m+1} - v_m = \frac{c}{2nl} \tag{2.7}$$

A sample fluid usually flows through the optical cavity with the bioreceptor-functionalized internal surface. When target molecules are attached to the immobilized bioreceptors, the local refractive index, where the binding event happens, and the electric field distributions inside the optical cavity are changed. This, in turn, causes the resonance spectrum to be shifted. Most FPI-based biosensors measure the shift in the resonance peak using a spectrometer or a tunable laser while some technologies measure the intensities at a single or multiple wavelength(s).

2.1.1. FPI-based Biosensors with Two Reflecting Surfaces

There have been efforts to develop optical biosensors utilizing the simple structure of FPI to have characteristics such as an easy fabrication process, simple test setup, and cost-effectiveness [72-84]. For example, You *et al.* developed a microfluidic enhanced FPI-based biosensor to detect glucose, sodium chloride (NaCl), and potassium chloride (KCl) for diabetes patients [74]. The reflecting surfaces are fabricated by depositing silver (Ag) and silicon dioxide (SiO_2) thin films as shown in Figure 2.2(a). The different concentrations of glucose, NaCl, and KCl from 5% to 25% were measured by detecting the peak shift using a spectrophotometer. The resolution for the bulk refractive index detection of the proposed device was 10^{-5} refractive index unit (RIU) while the minimum detectable concentrations were determined to be 0.01% glucose, 0.00769% KCl, and 0.00555% NaCl solutions.

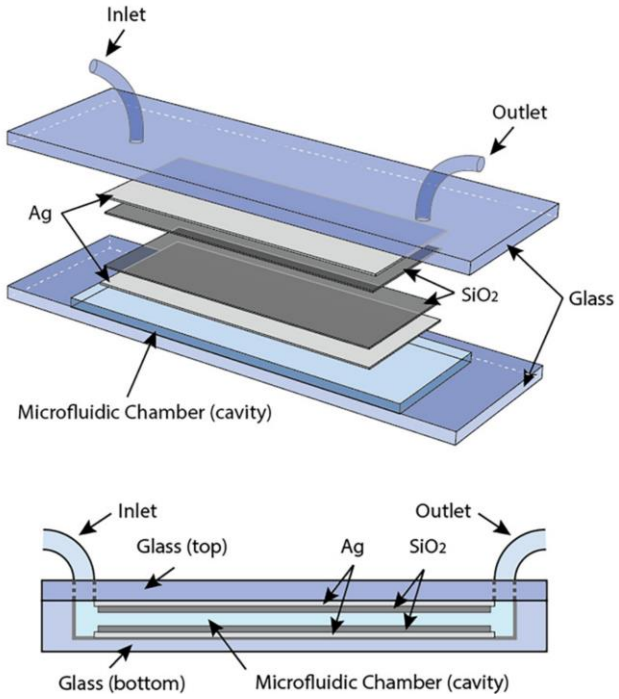

Figure 2.2. Schematic of an FPI-based biosensor with two planar-parallel reflecting surfaces. Reproduced from ref. [74] with permission from Elsevier.

Some researchers have tried to modify the FPI structure to enhance the sensitivity of the FPI-based biosensor further. For example, Tu *et al.* reported a micromachined-FPI (μFPI) with a perforated gold layer with nanohole arrays on a reflecting surface to increase the sensing surface area as shown in Figure 2.3(a) [77]. The nanohole arrays has a diameter of 200 nm and a period of 500 nm fabricated using a focused ion beam (FIB) milling. The sensitivity of refractive index detection was obtained to be 593 nm/RIU with a Q-factor of 128.4. Dielectrophoresis (DEP) technique was employed to concentrate molecules near the nanoholes using an external electric field as illustrated in Figure 2.3(b). With this technique, the concentration of BSA was measured down to 1 pM. In a similar work, Zhang *et al.* developed a nanostructured-FPI (nanoFPI) device with an embedded nanopore layer inside the cavity [78]. The Au-coated nanopore layer with a size of 50 nm is created to increase the sensing area and enhance the sensitivity as shown in Figure 2.3(e). The same research group employed the nanoFPI to detect beta-amyloid (Ab42) and total tau (T-tau) biomarkers in cerebrospinal fluid (CSF) for the diagnosis of Alzheimer's diseases [79]. One sensor chip has four nanoFPIs as shown in Figure 2.3(d), and each of them has its own sub-inlet and sub-outlet to functionalize two different antibodies, allowing the multiplexed detection of Ab42 and T-tau. They were able to detect Ab42 and T-tau in buffer down to 7.8 pg/mL and 15.6 pg/mL, respectively, validating the specificity by introducing Ab42-buffer to the T-tau antibody-functionalized sensor and vice versa. The CSF samples spiked with the Ab42 concentrations from 31.25 pg/mL to 500 pg/mL and the T-tau concentrations from 125 pg/mL to 2000 pg/mL were measured showing the potential to monitor the multiple biomarkers in clinical samples.

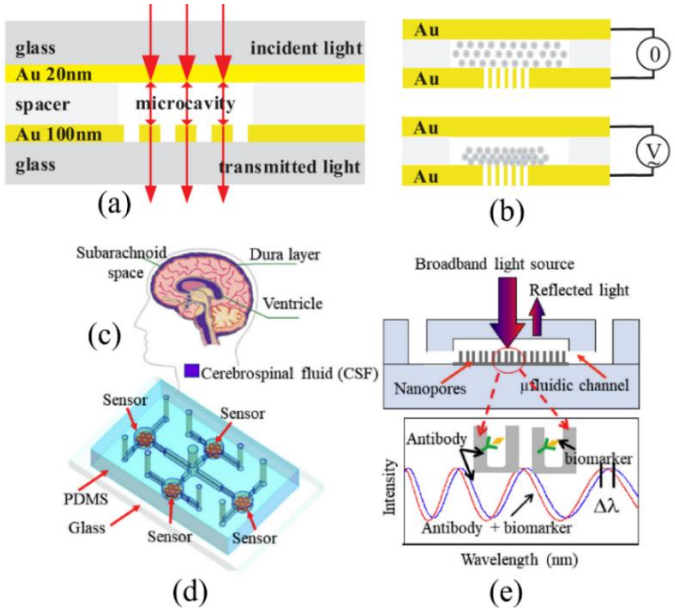

Figure 2.3. Nanostructures employed at one side of the FPI. (a) Schematic of the μFPI. (b) Concept of DEP. Reproduced from ref. [77] with permission from Elsevier. (c) The indicated location of CSF. (d) Schematic of a chip with four nanoFPIs. (e) The working principle of nanoFPI. Reproduced from ref. [79] with permission from Elsevier.

A cascaded FPI sensor is also proposed to achieve the improved sensitivity of the FPI-based biosensor [85]. It consists of a tunable laser source, a reference cavity, an optical fiber between cavities, a sensing cavity, and a power sensor as shown in Figure 2.4(a-b). The transmission spectrum of the cascaded FPIs shows a higher Q-factor and a larger FSR due to the Vernier effect. The different concentrations of NaCl were measured in triplicate, and the sensitivity of bulk refractive index change was obtained as 23,794.6 nm/RIU for the resonant wavelength shift, which corresponds to the LOD of 8.4×10^{-7} RIU. For the intensity-based measurement at a fixed wavelength, the LOD was obtained to be around 1.3×10^{-5} RIU. Different concentrations of Streptomycin-BSA conjugate antigen in the range of 1-7 ng/mL were detected with the cascaded FPI biosensor. For the experiments, Streptomycin-BSA is mixed with Streptomycin monoclonal antibody and introduced into the channel. The refractive index difference due to the different

concentration of Streptomycin-BSA produces measurable signal changes. The specificity of the device was also validated by introducing Kanamycin and phosphate buffer saline (PBS) to confirm negligible wavelength shifts from their interactions with Streptomycin monoclonal antibody.

Other researchers employed distributed Bragg reflectors (DBRs) as reflecting surfaces for the FPI to achieve a high Q-factor [72, 73, 80]. The DBR consists of two alternating dielectric layers with high and low refractive indices, acting as a highly reflecting region with a low absorption loss. For instance, Wu *et al.* reported an all glass FPI-based biosensor using DBRs as partially reflecting regions as shown in Figure 2.4(c-e) [73]. The DBR consisted of 3.5 pairs of SiO_2 and tantalum pentoxide (Ta_2O_5) deposited on a glass slide. Two of the slides were separated by a coverslip and bonded using UV adhesive. The device was able to detect 15 ng/mL of glucose solution, which corresponds to 2 x 10^{-9} RIU, with the Q-factor of 875.

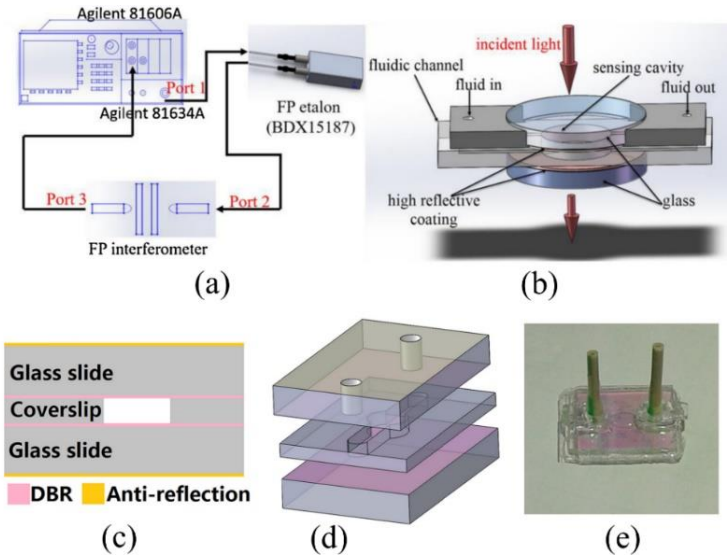

Figure 2.4. (a) Schematic of the two cascaded FPIs system. (b) The sensing FPI. Reproduced from ref. [85] with permission from Elsevier. (c) Schematic of the FPI employing two DBRs. (d) Fabrication process. (e) Image of the fabricated sensor. Reproduced from ref. [73] with permission © The Optical Society of America.

The simplicity of the FPI structure is ideal to develop various configurations by incorporating other structures with it. For example, Takahashi *et al.* utilized an FPI to improve the sensitivity of a microelectrochemical system (MEMS)-based surface stress sensor for label-free biosensing [76]. The FPI structure consists of two gold (Au) layers with a thickness of 50 nm for highly reflecting surfaces. The top Au layer is deposited at the center of the parylene C film, which acts as a movable membrane as shown in Figure 2.5(a). To demonstrate the label-free biosensing, the Au film on the movable membrane was functionalized with BSA antibodies as seen in Figure 2.5(b). As BSA molecules in PBS buffer solution are introduced and captured by the antibodies, the movable membrane is deflected by the surface stress change, which leads to a displacement in the optical cavity length and a shift in the reflection spectrum measured by a spectrometer in the test setup (Figure 2.5(c)). The proposed FPI-based biosensor was able to detect 10 ng/mL of BSA. To evaluate the response from nonspecific binding, 100 ng/mL of avidin was introduced showing 2.4 times smaller deflection than that measured with 10 ng/mL of BSA.

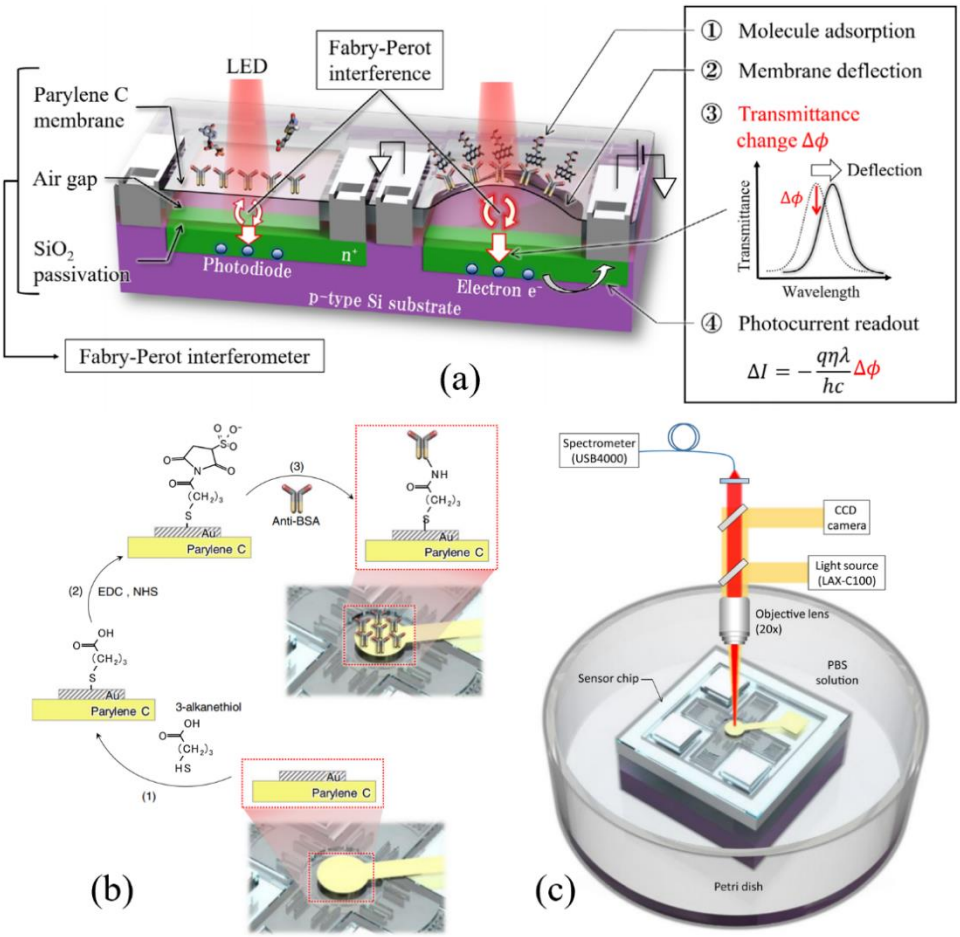

Figure 2.5. Schematics of the FPI incorporated surface stress sensor. (a) Transducing procedure showing the deflection of the movable membrane film as target molecules adsorb to it. (b) Anti-BSA immobilization. (c) Spectrum measurement. Reproduced from ref. [76] with permission from IOPscience.

2.1.2. Porous Silicon Microcavity (PSM)-based Biosensors

Porous silicon microcavity (PSM) is a FPI structure created by two DBRs with a thin layer of porous silicon (PS). PS is inexpensive and easy to fabricate, and has a large sensing surface, so it has been widely investigated to develop label-free optical biosensors [86-96]. The refractive index of a PS layer is determined by the porosity, which can be modulated by adjusting parameters of electrochemical etching such as the etching time and current density. A high porosity produces low refractive index of PS

layer and vice versa. A high surface-to-volume ratio can be obtained by a high porosity, which improves the adsorption of target molecules to the immobilized bioreceptors on the internal pore walls. However, there is a tradeoff between the porosity and the durability of the structure. For biosensing tests, as target molecules in a sample fluid were bound inside the pores, the effective refractive index inside the pores was increased causing a shift in the resonance spectrum.

Li *et al.* developed a PSM-based biosensor for bacterial detection [89]. The DBR layers were optimized to have 8 periods for the top DBR and 20 periods for the bottom DBR showing a narrow resonance peak at around 600 nm with a FWHM of 8 nm as shown in Figure 2.6(a). The pore diameter of the PSM structure was measured to be in the range between 5 and 20 nm, and the quality of the pore was evaluated by checking if any blockage appeared on a cross-sectional image shown in Figure 2.6(b). The surface was modified using undecylenic acid and vancomycin receptor molecules, which have affinity to various types of bacteria. Because the dimension of bacteria is about 2 μm x 1 μm, which is too big to be infiltrated into the PS, the bacteria wall debris molecules with a diameter of 8 nm were generated by pretreatments. The different concentrations of solutions from 10 to 10,000 bacteria/mL were tested showing a LOD of 20 bacteria/mL as described in Figure 2.6(c). Other PSM-based biosensors for DNA detection were also reported [86, 88]. Zhang *et al.* employed a PSM-based DNA biosensor using silicon-on-insulator (SOI) wafer [86]. SOI wafer has benefits in terms of realizing a miniaturized biosensor integrated on a photonic integrated circuit. The PSM on SOI had an average pore diameter of 20 nm to detect 19-base pair DNA with a length of about 4 nm. The reflectance spectrum of the device showed a resonance peak at 1555 nm with a FWHM

of 26 nm. The 3-aminopropyl-triehoxysilnae (APTES) and glutaraldehyde are used to immobilize probe DNAs on PSM. The different concentrations of complementary DNA were measured ranging between 0.625 and 12.5 μM with a LOD of 43.9 nM as shown in Figure 2.6(d).

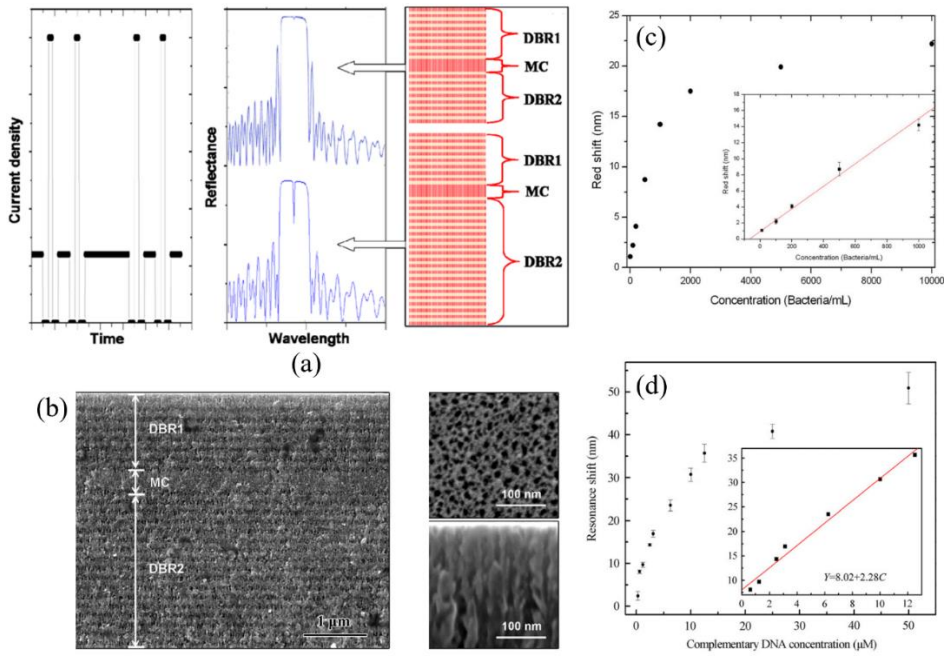

Figure 2.6. (a) (left) Current density used to fabricate two DBRs. (middle-right) Narrow resonance peak using the PSM structure of 8 layers for DBR1 and 20 layers for DBR2. (b) Scanning electron microscope (SEM) images of the PSM. (c) PSM measurement results for bacteria concentrations. Reproduced from ref. [89] with permission from IOPscience. (d) PSM measurement results for DNA concentrations. Reproduced from ref. [86] with permission from Elsevier.

Another research group developed a spectrometer-free PSM-based biosensor [88]. The PSM was fabricated to have a diameter of pores ranging from 10 to 20 nm for the detection of 8-base pair DNA with a length of about 1.76 nm. Instead of measuring the spectrum using a spectrometer, the proposed system employed a goniometer changing the incident angle of the light to the PSM-based biosensor from a single-wavelength laser source as shown in Figure 2.7(a). As the effective refractive index changed in the PSM,

the incident angle at the resonance peak is shifted which can be translated into the shift in the spectrum. The incident angle was measured after each step of the surface preparation confirming the sensing capability of the device and the immobilization of the probe DNA on the pores surface. The different concentrations of the complimentary DNA were measured from 0.3125 to 10 μM, and the LOD of the device was calculated to be 87 nM with the angle resolution of 0.2^{o}. The LOD of refractive index change was 5×10^{-4} RIU. The same research group reported another type of spectrometer-free PSM-based biosensor using transmission angular spectrum [92]. The visible light source was replaced with the near-infrared laser light to reduce the absorption on the PSM and possible damage to biological samples. They demonstrated the transmission angular spectrum-based approach through the detection of hydatid disease antigens. The shift in the spectrum was confirmed by comparing angle measurements obtained from each surface functionalization process and the antigen-antibody interaction as shown in Figure 2.7(b-c). The different concentrations of hydatid antigen from 0.5 to 20 ng/mL in 20 mL solution were infiltrated to the PSM and the LOD is determined to be 0.16 ng/mL as shown in Figure 2.7(d). The specificity of the device with hydatid antibody was demonstrated by observing negligible angle changes from the introduction of non-hydatid antigen.

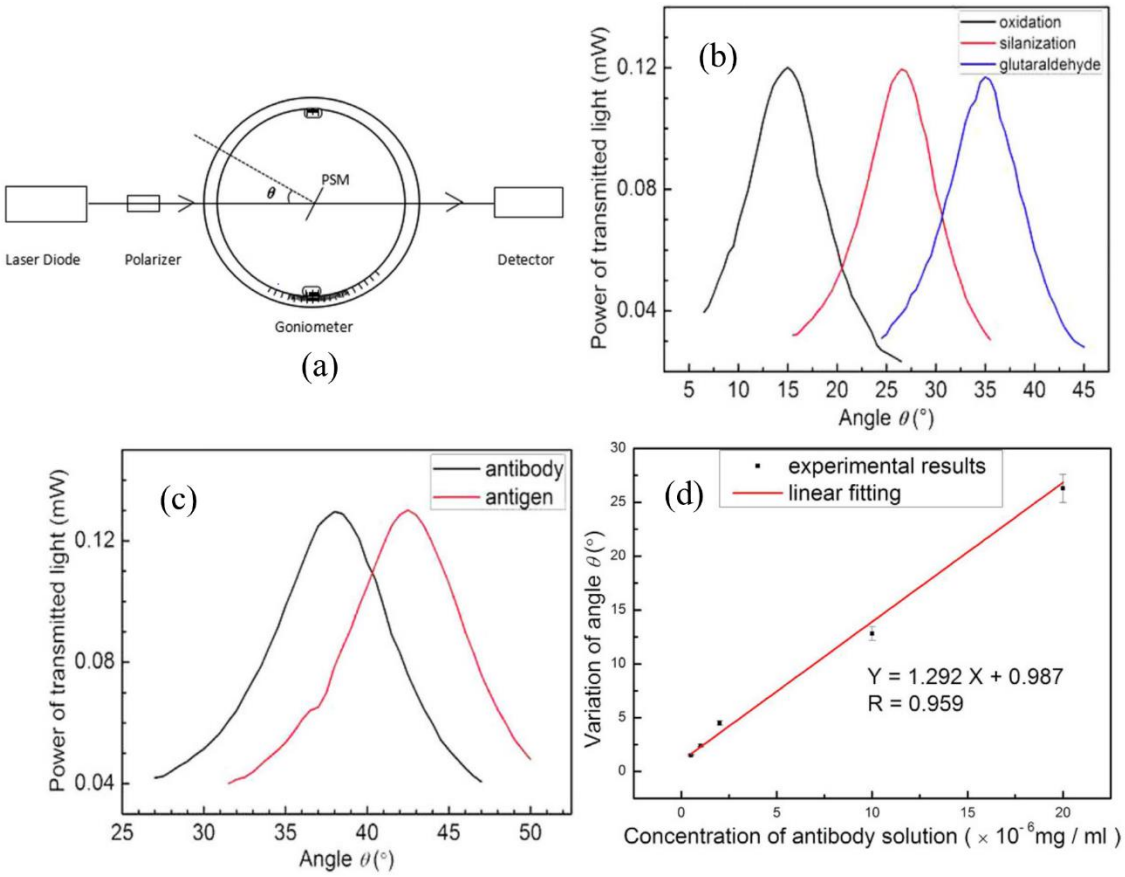

Figure 2.7. (a) Schematic of the spectrometer-free PSM method. (b) Shift in transmission angular spectrum during the surface funtionalization. (c) Shift by the antigen-antibody. (d) Measurement results for the concentrations of hydatid antigen. Reproduced from ref. [92].

Some researchers investigated the potential of PSM-based biosensors for multiplexed, real-time detection, and POC diagnostics [87, 90, 91]. Pham *et al.* presented a PSM sensor to detect two different organic solvents simultaneously and also measure low concentration of pesticide in water [90]. As shown in Figure 2.8(a), the atrazin pesticide was detected at different concentrations from 2.15 to 21.5 pg/mL with LODs of 1.4 pg/mL and 0.8 pg/mL in water and humic acid, respectively. The performance of the real-time and in-flow sensing using PSM-based sensor was evaluated [87]. A fluidic cell incorporated with the PSM was built using poly(methyl methacrylate) (PMMA) for the

purpose of enabling the real-time monitoring of the reflectance spectrum as a sample fluid infiltrated the PSM as described in Figure 2.8(b). The refractive index sensing was done by measuring different concentrations of ethanol in DI water with a LOD of 1000 nm/RIU, corresponding to 10^{-7} RIU. Recently, Cao *et al.* reported a smartphone-based PSM-biosensor for POC diagnostics [91]. The built-in LED with a band-pass filter (BPF) and the camera of a smartphone were used as a light source and a detector of the platform, respectively, as shown in Figure 2.8(c). A shift in the reflectance spectrum from the adsorption of target molecules on the PSM was detected as an intensity change measured by a smartphone camera. To maximize the relative intensity change from the effective refractive index change, the center wavelength of a BPF was selected to 606.5 nm, which is at between the resonance dip of PSM at near 600 nm and the highest reflectance at near 630 nm as represented in Figure 2.8(d). A customized enclosure was designed to facilitate the alignment of a smartphone with a BPF and a PSM-based biosensor and built with a 3D-printer. The resolution of the intensity change was obtained to correspond to a wavelength shift of 0.33 nm, and the sensitivity of the biosensor for the refractive index change was measured as 350 nm/RIU using glucose solutions. The biosensing capability of the system was demonstrated by measuring different concentrations of streptavidin, and the LOD was estimated to be nearly 500 nM as shown in Figure 2.8(e).

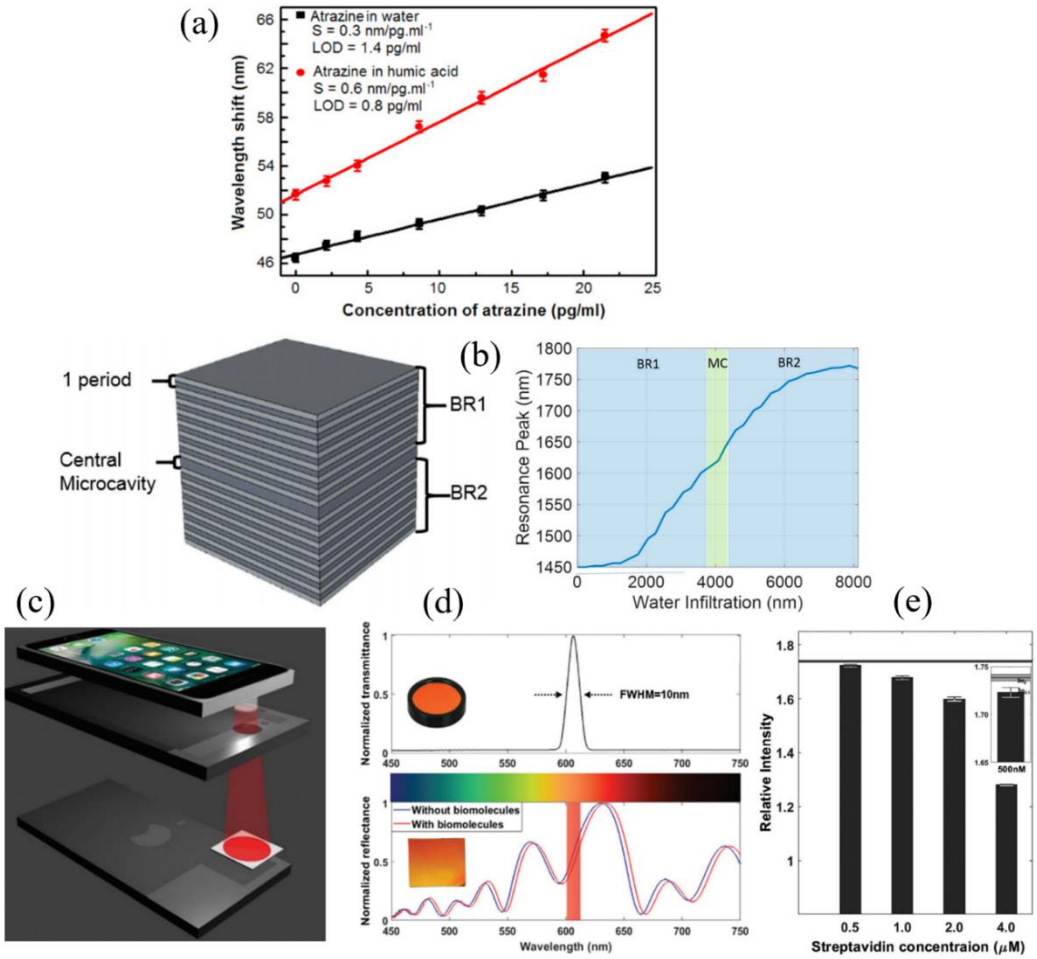

Figure 2.8. (a) Detection of the atrazin pesticide in two different buffers. Reproduced from ref. [90]. (b) Measured resonance peak in real-time as water infiltrated to PSM. Reproduced from ref. [87]. (c) Schematic of the smartphone-based system. (d) BPF spectrum and the change in normalized transmittance with the adsorption. (e) Measurement results for the concentration of streptavidin. Reproduced from ref. [91] with permission from The Royal Society of Chemistry.

2.1.3. Optical Fiber FPI-based Biosensors

The optical fiber was originally developed to guide light waves along the core, which is surrounded by a cladding layer, through the total internal reflection at the interface with negligible loss. Over the last few decades, optical fibers have been extensively investigated for biosensing applications with the intrinsic advantages including flexibility, low-cost, small size, and biocompatibility [75, 97-106]. To be

developed as a biosensor, the structure of optical fiber has modified to maximize the interaction of light with target analytes and increase the sensitivity [97]. Out of various types of optical fiber-based biosensors, optical fiber FPI-based biosensors have been considered as a promising sensing platform [99, 100, 107-109]. The FPI in the optical fiber is created by splicing it with a different type of optical fiber or depositing a thin reflective layer on the tip. As the effective refractive index or the optical path length between two reflectors of the optical fiber changes, the resonance peak is shifted and measured to determine the concentration of target analytes.

Liu *et al.* reported an inline optical fiber FPI-based biosensor for label-free immunoassay [100]. The FPI structure was fabricated by cleaving both ends of a hollow-core photonic crystal fiber (HCPCF) and splicing to two single mode fibers (SMFs), defining three reflectors, as shown in Figure 2.9. The refractive index sensitivity of the sensor was obtained to be 7 x 10^{-5} RIU [101]. To evaluate the proposed device as a label-free immunosensor, the end tip of the SMF was functionalized with goat anti-rabbit immunoglobulin (IgG) using the APTES silanization and glutaraldehyde solution. The concentration of rabbit IgG of 100 ng/mL in PBS was detected in real-time.

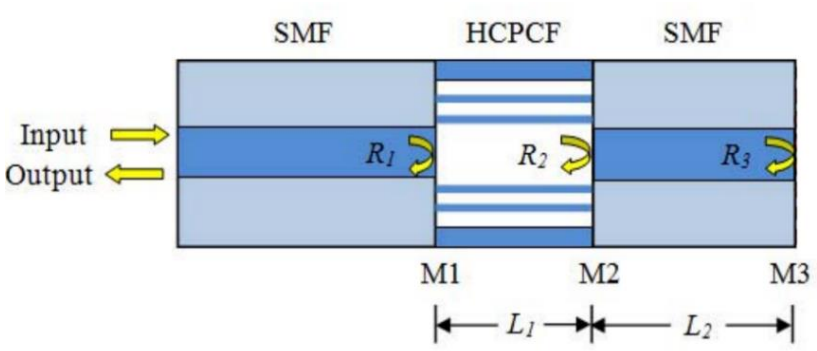

Figure 2.9. Schematic of the optical fiber FPI. Reproduced from ref. [101] with permission from Elsevier.

Without the need of cleaving or splicing, Wu *et al.* introduced an optical fiber FPI-based biosensor by using a hydrogel to detect bio-toxins [102]. As shown in Figure 2.10(a), two reflective interfaces of this optical fiber FPI-based biosensor are created by the hydrogel layer with a thickness of around 100 μm in between an optical fiber and a glass. The hydrogel was initially fabricated to be water-insoluble with a crosslinker chosen to be cleaved by a specific agent. The target bio-toxin molecules react with the crosslinker, making it water-soluble. The hydrogel degrades, which causes changes in its optical properties. Dithiothreitol (DTT) solutions with different concentrations were applied to the hydrogel, and the resonant spectrum change induced by the degradation of the hydrogel was monitored in real-time. They were able to detect DTT down to 50 μM. Cano-Velazquez *et al.* also reported a polydimethylsiloxane (PDMS)-coated optical fiber FPI as shown in Figure 2.10(b) [103]. The PDMS has been widely used to fabricate optical and microfluidic devices by the virtue of the transparency, easy-of-use, and biocompatibility. The hydrophobic PDMS surface was functionalized with mycobacterial lipid antigens, used for tuberculosis diagnosis. The functionalized optical fiber tip was then immersed into Pre-immune serum (PS) and Hyper-immune serum (HS), and the shifts in the resonance peak due to the binding of mycobacterial lipid antigens to anti-lipid antibodies in PS and HS serums were measured in real-time. PS was prepared before immunization having no antibodies, and HS was obtained after immunization with high concentration of antibodies. After compensating the thermal expansion of PDMS, the bio-layer thicknesses created for PS and HS serums were estimated to be 10.78 nm and 30.61 nm, respectively. The antigen coating on the PDMS tip was confirmed to be

preserved after exposing it to protein denaturation washes. The results show the potential to realize label-free and real-time detections using a reusable optical immunosensor.

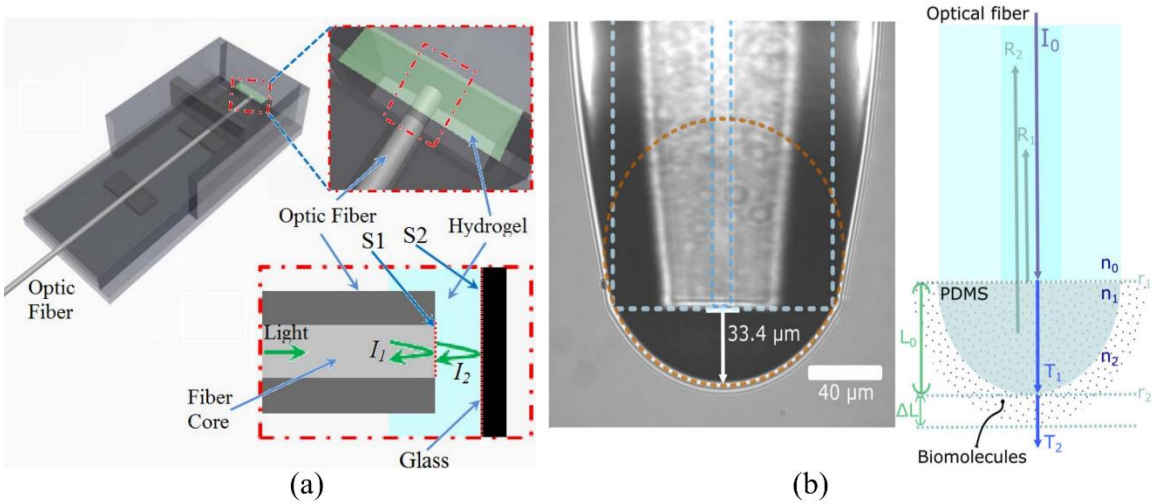

Figure 2.10. (a) Schematic of optical fiber FPI-based sensor using hydrogel. Reproduced from ref. [102] with permission from IEEE. (b) Schematic of optical fiber FPI-based sensor using PDMS. Reproduced from ref. [103] with permission © The Optical Society of America.

Recently, biolayer interferometry (BLI) has been considered as one of the most promising techniques for optical fiber-based, label-free, and real-time detection of biomolecular interactions [110-124]. BLI includes two reflective surfaces forming a FPI created by a reference layer at an optical fiber tip and the surface of immobilized bioreceptors as shown in Figure 2.11 [121]. When white light is propagating toward the fiber tip, the light beams reflected at each of the two surfaces interfere with each other producing a resonance response in the reflectance spectrum. As the tip of BLI with bioreceptors is dipped into a sample fluid, the target biomolecules bind to the surface, which increases the thickness of the layer and the effective optical length of the FPI causing the shift in the spectrum. A detector measures the reflectance spectrum in real-time enabling binding kinetics analyses. BLI has been employed in a wide range of

biosensing applications from the study and development of drugs and vaccines [112, 114] to the detection of various biomolecules [116-118, 120, 122-125].

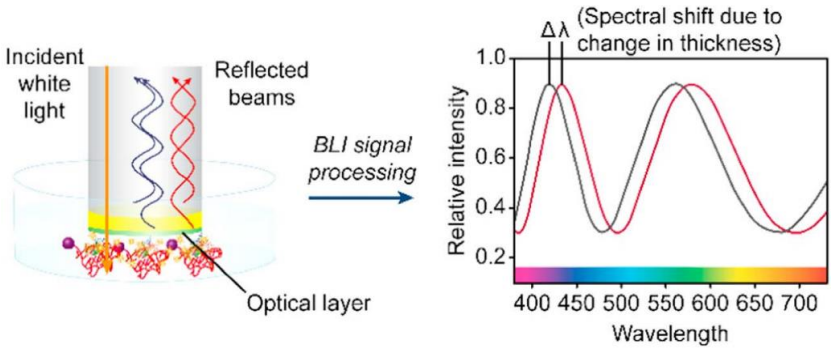

Figure 2.11. Schematic of BLI. Reproduced from ref. [121] with permission from Elsevier.

For example, Ziu *et al.* employed the BLI to detect tau441 protein, which is one of biomarkers for the neurodegenerative diseases [111]. One of commercially available BLI-based biosensors, BLItz instrument (ForteBio, USA), was used for the experiments. The tip was functionalized with streptavidin molecules and biotin aptamers. The concentrations of tau441 protein prepared in MES buffer was measured from 0 to 64 nM, with a LOD of 6.7 nM. The selectivity of the sensor was evaluated by confirming negligible signals obtained from other proteins including amyloid-b_{40}, a-synuclein, and BSA. The detection of tau441 in a complex sample, fetal bovine serum (FBS), was conducted using a concentration of 21 nM. The result showed the wavelength shift was similar to the shift obtained from the result using 21 nM of tau441 in MES buffer. Another work employed the BLItz platform to analyze the interactions between proteins and nucleic acids to characterize CRISPR-Cas systems [120]. The BLI sensor tip is functionalized with streptavidin and biotinylated oligonucleotides. Figure 2.12 shows the real-time detection results of ribonucleoprotein (RNP) complexes. The complex consists

of a CRISPR RNA (crRNA) and CRISPR-associated (Cas) proteins and interacts with a specific anti-CRISPR (Acr) protein. The detection of Acr protein for two different complexes, the Type I-Fv and the Type I-F, was performed with a concentration of 500 nM.

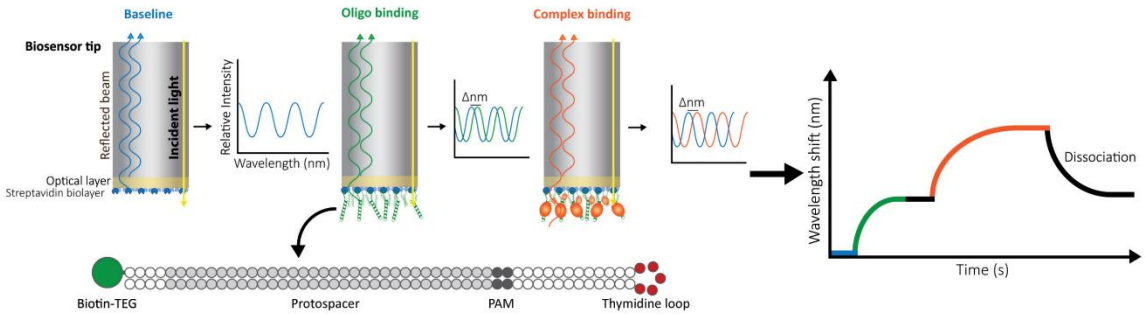

Figure 2.12. Real-time detection for the tip immobilization procedure. Reproduced from ref. [120] with permission from Frontiers.

The Octet platform (ForteBio, USA) is an another commercial BLI-based biosensor, which is capable of detecting biomolecules with a molecular weight of 150 Da, using up to 384-wells for high throughput [110, 113, 117, 126]. The LOD is given by the manufacturer in the range between nM and μM [117]. Gao *et al.* reported the detection of Gonyautoxin 1/4 (GTX1/4) aptamer with an Octet platform [123]. It is one of the most well-known neurotoxins causing paralytic shellfish poisoning (PSP). The GO18-T-d aptamer was used as the bioreceptor, and the concentrations of GTX1/4 were measured in the range from 0.2 ng/mL to 200 ng/mL as shown in Figure 2.13(a-b). The LOD was determined to be 50 pg/mL, and the selectivity of the sensor was evaluated by confirming the negligible cross-reactivity with other toxins, saxitoxin (STX), neoSTX, and GTX2/3 as shown in Figure 2.13(c). The same author also performed the detection of STX with the M-30f anti-STX aptamer using an Octet platform [122]. The different

concentrations of STX were measured with a LOD of 0.5 ng/mL. The reusability of the sensor was also evaluated by verifying the remaining sensing capability through four repeated tests.

Another work employing an Octet platform was proposed to quantitatively detect testosterone levels [124]. Biotinylated double-stranded DNA (dsDNA) fragments of operator 1 (OP1) and OP2 were immobilized to the streptavidin-coated surface. Repressor (RepA) proteins attach to the dsDNA OP1 resulting in resonant wavelength shift for different concentrations as shown in Figure 2.13(d). The presence of testosterone causes a structural change of the RepA protein leading to the decrease in binding of it to dsDNA. Figure 2.13(e) shows the real-time measurement results of different concentrations of testosterone down to 2.13 ng/mL, showing the negative correlation with the signal.

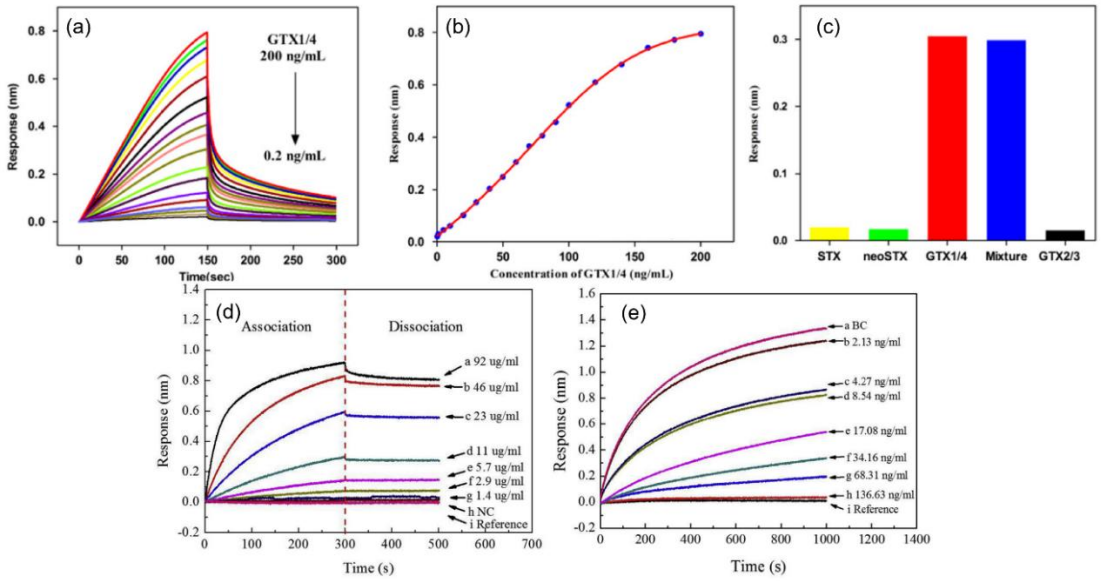

Figure 2.13. (a) Real-time detection after introduction of GTX1/4 at concentrations in between 0.2 and 200 ng/mL. (b) Response versus concentrations. (c) Evaluation on specificity of the sensor using other toxins. Reproduced from ref. [123] with permission from Elsevier. (d) Binding of RepA protein to the dsDNA OP1. (e) Measurement results of testosterone. Reproduced from ref. [124] with permission from Elsevier.

2.2. Whispering Gallery Mode (WGM)-based Biosensors

Another increasingly pronounced class of high sensitivity optical resonators for use in biosensors is whispering gallery mode (WGM) resonators. Most works employing WGM resonators cite high Q-factors, high sensitivity, and rapid results, within micro- to nanoscale feature sizes. WGM-based biosensors are composed of a closed, radial cavity critically coupled to a prism, waveguide, fiber on its side or on the tip of a fiber as shown in Figure 2.14 [127-132]. WGM resonators confine light waves in any radial or polygonal enclosed surface, including rings, disks, spheres, cylinders, fibers, rods, or toroids for example. They may also be categorized as either passive WGM or active WGM resonators, based on lasing capability and coupling method. Active resonators make up the class which are capable of lasing, such as doped materials or resonators made of a gain medium. These are capable of being pumped remotely and collecting their spectra separately. Passive WGM must be directly coupled to a tunable laser source and detectors via fiber or waveguide [130, 131]. These types do not generate light, but their resonance spectrum is tracked from the output transmission.

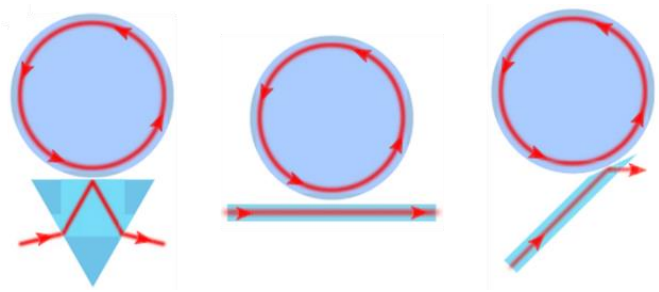

Figure 2.14. Coupling methods for WGM resonators. Reproduced from ref. [127] with permission from Elsevier.

In a passive WGM resonator, the critical coupling condition is met when the light source's resonant wavelength and linewidth match that of the resonator, as indicated

by a transmission minimum in its spectra. The resonant wavelength of the resonator, λ_{res}, is given by

$$\lambda_{res} = \frac{2\pi r n_{eff}}{m} \tag{2.8}$$

where r is the radius of the curvature, m is the mode number (integer value), and n_{eff} is the effective refractive index which changes with interactions on the resonator surface. The coupling (interaction) length (shown in Equation 9) is proportional to the Q-factor of the resonator and its resonant wavelength.

$$L = \frac{Q\lambda_{res}}{2\pi n} \tag{2.9}$$

where L is the coupling length, Q is the Q-factor, and n is the refractive index of the resonator material. Light waves travel the circumference via total internal reflection at the external barrier. Neglecting absorption or losses, the waves would continuously reflect along the boundary of the cavity. The surrounding material must be of a lower refractive index so that total internal reflection can occur. These travelling light waves eventually interfere constructively or destructively with newly arriving light waves from the waveguide. Physiochemical changes, such as those in bio- detection, modify the optical path length. The increased optical path length affects incoming light interactions with existing WGMs [128, 129, 131, 133, 134]. One or more detectors may be used to monitor spectral shifts, which are detectable when binding occurs on the surface of the resonator. The resonant wavelength shift due to such binding event can be expressed as

$$\frac{\Delta\lambda}{\lambda} = \left[\frac{\alpha_{ex}\sigma}{\varepsilon_0(n_r^2 - n_b^2)r}\right] \tag{2.10}$$

where λ and Δλ are the resonant wavelength and resonant wavelength shift, respectively, while α_{ex} is excess polarizability of molecules and σ is the surface density due to binding activity. The permittivity in a vacuum is ε_0, r is the radius of the curvature, and n_r and n_b are the resonator and buffer refractive indices, respectively [131].

With respect to the system in which WGM resonators are equipped, advances such as transduction and data-processing or filtering techniques [62], dynamic referencing [135], surface functionalization [136-138] and the integration of microfluidics have been reported. Many WGMs are integrated into microfluidic chips to streamline testing with small sample volumes [128]. The resulting spectra is received through a detector typically in real-time. Figure 2.15 shows the system typically constructed around a WGM resonator. For example, an input waveguide is coupled to the resonator, and the spectral output from both the input waveguide and resonator are recorded at separate detectors.

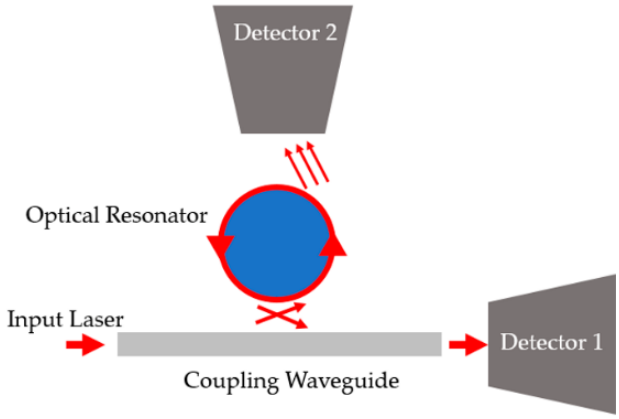

Figure 2.15. Example WGM resonator system as mentioned in [131]. Reproduced from Open Access Article (MDPI).

WGM biosensors are highly sensitive to changes in the surface conditions and refractive index and they have been developed for single-molecule detection [61, 62,

139], pico- to atto-molar scale detection [62, 136, 137, 140-145], and monitoring biological processes [146-149] or enzymatic reactions [150, 151]. In recent studies, researchers have also taken advantage of geometric modifications [152, 153] and material doping [140, 142, 143, 154-157] to improve the Q-factors and sensitivity of WGM-based resonators. Geometric differences in most resonators may depend on fabrication capabilities or desired optical qualities, such as mode confinement, increased binding surface area, simpler fabrication techniques, or material choice.

In the following sections, recently reported WGM resonator biosensors are organized by most to least common geometry. Novel material use, methods of fabrication, functionalization and optical configurations are discussed, in addition to demonstrated biosensing capability, if any. A tabulated summary of the following is also provided in Table 2.

2.2.1. Ring and Disk-based WGM Biosensors

Disk and ring resonators have been investigated in a considerable number of recent studies. Figures 2.16 and 2.17(a) below are sample SEM images of ring and disk geometries.

Cascaded-micro ring resonators (CMRR) have been proposed to improve sensitivity of the ring resonator-based biosensors [136]. In a recent work by Xie *et al.*, cascading was used to exploit the expansion of the FSR due to the Vernier effect, thus amplifying the measured signal changes. The CMRRs modified with molecularly imprinted polymers (MIPs) were used to detect progesterone. The waveguide and ring structures were first fabricated on SOI wafers via photolithography and etching processes, then the MIPs were formed using photopolymerization. The Q-factor for the

reference ring was 1.7 x 10^3 while that of the sensing ring was 1.0 x 10^3, which is reduced further upon interaction. Non-imprinted polymer samples (NIPs) were exposed to the same post treatment and testing for the specificity test. The tunable laser light source is coupled to the CMRR chip's input waveguide through a fiber array. Reference and output spectra are monitored using a power meter at the pass and drop ports, respectively as shown in Figure 2.16(a). An integrated microfluidics system was used to inject solutions into the chip. The normalized output power over time for the introduction of various progesterone concentrations was monitored in real-time, resulting in a linear relationship between log concentration of progesterone and the normalized output power as shown in Figure 2.16(f). The average test time in these experiments under 10 minutes with a LOD of 83.5 fg/mL. There was no significant power output change for Testosterone and NIP samples, which demonstrates the devices specificity and the non-imprinted samples as a control as shown in Figure 2.16(e).

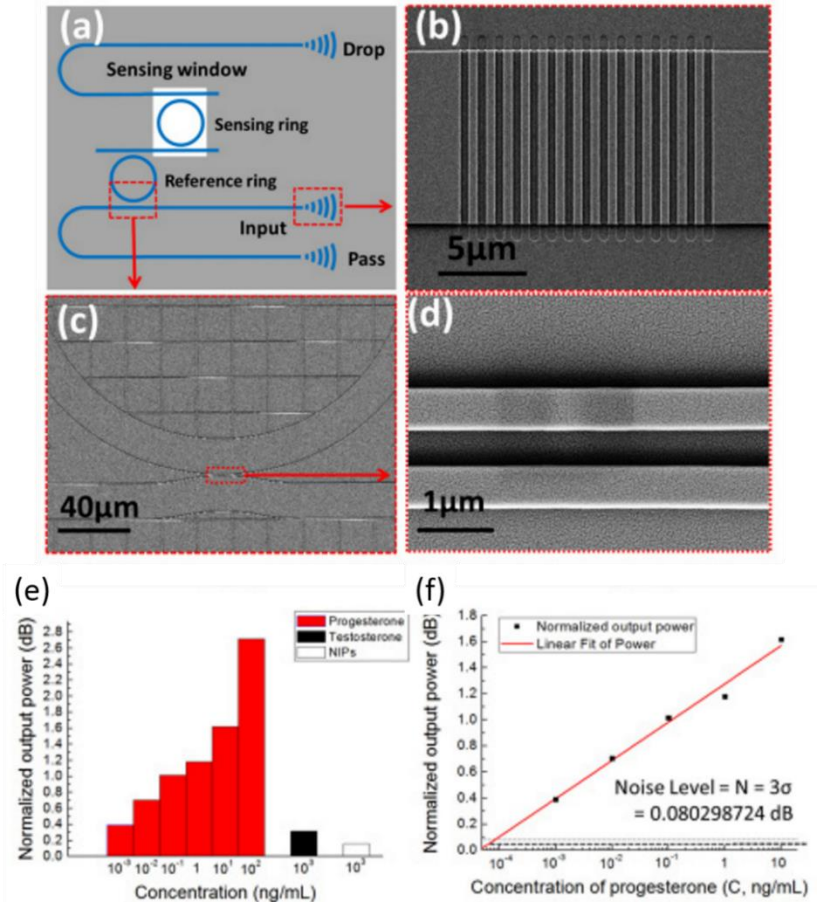

Figure 2.16. (a) Schematic of the CMRR setup. (b, d) SEM images of the grating used as couplers in different areas of the sensor, and (c) SEM of the reference ring coupled to the input waveguide. (e) NOP changes as a result of varying concentrations of progesterone (red), testosterone (black), and the NIP control (white), to demonstrate specificity. (f) Linear fit of power versus progesterone concentration. Reproduced from ref. [136] with permission © The Optical Society of America.

Structural modifications that increased mode confinement and/or increase the available binding surface area were desirable [138, 152, 153]. For example, Taniguchi *et al*. implemented a slot waveguide structure into ring resonators for label-free detection of PSA [138]. The silicon nitride (SiN) ring resonator, which has a superior thermal stability to a silicon ring resonator, is used as shown in Figure 2.17 (a-b). The slot width needed to be at least twice that of the experimental analyte to prevent steric hindrances and its ideal dimension was determined by simulations. The ring was functionalized with protein G,

and then PSA antibody through silicon tagging (Si-tag) as the crosslink between Protein G and the SiN ring surface as depicted in Figure 2.17(c). Protein G was preferred in this case due to its greater binding efficiency with antigens. The resulting PSA detection limit was 10 ng/mL, which is near the clinical value (1 ng/mL).

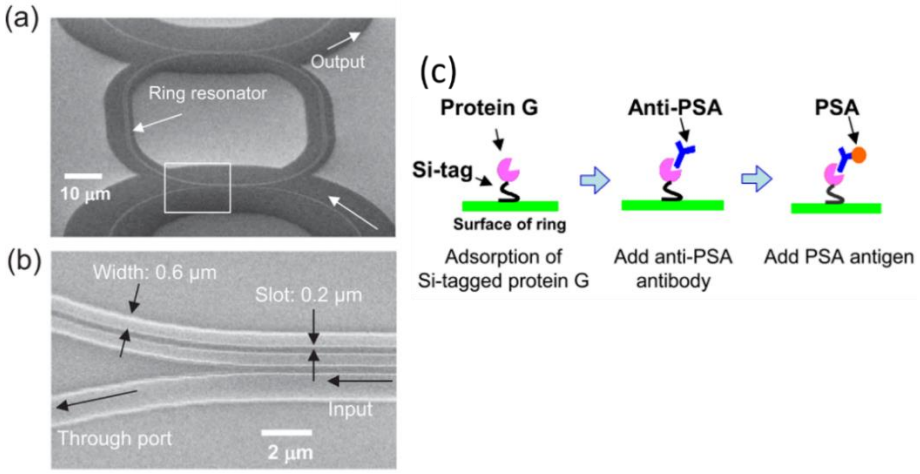

Figure 2.17. (a) SEM overview of the slotted ring coupled to the input and output waveguides. (b) a magnified image of the coupling point between the ring and input waveguide. Reproduced from ref. [138] with permission from Elsevier.

Subwavelength gratings (SWG) shown in Figure 2.18(a) have also been reported to enhance the Q-factor and sensitivity of SOI ring resonators in biosensing [152]. Grating modification increased the evanescent field overlap with attached analytes, thus increasing the sensitivity to binding events. The SWG ring resonators of various sizes and their respective circuitry were fabricated using electron beam lithography. The measured Q-factor of this system was 7000 and had a bulk sensitivity of 405 nm/RIU, for a probe wavelength of 1575 nm. The system's best detection limit was 2.47 x 10^{-4} RIU using the resonator with a duty cycle (the ratio of the pattern width to the period of the grating) of 0.7. A sandwich assay of immunoglobulin (IgG), anti-streptavidin, streptavidin (SA), and biotinylated BSA was used to demonstrate biosensing capabilities by monitoring

wavelength shifts in real-time. As shown in Figure 2.18(b), the total wavelength shift was nearly 2 nm, which is on comparative order to most other works in this review.

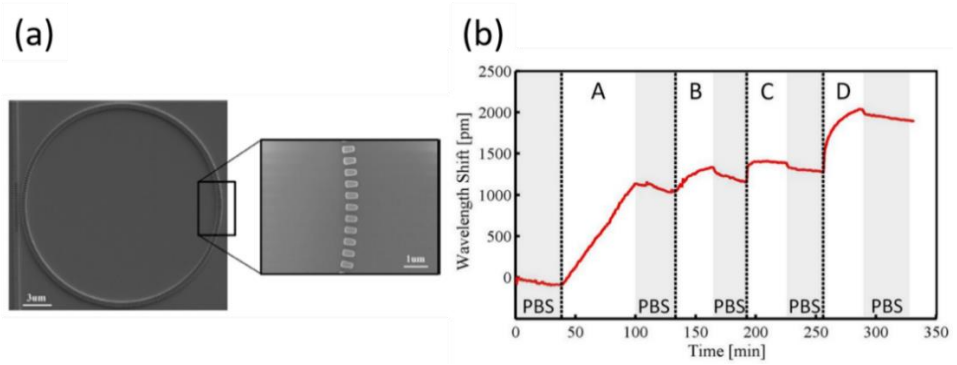

Figure 2.18. (a) SEM images of SWG ring resonator; (b) Wavelength shifts as a result of anti-streptavidin (A), BSA (B), streptavidin (C), and biotinylated BSA (D) as the target analyte. The shaded gray lines along the graph indicate PBS rinsing. Reproduced from ref. [152] with permission © The Optical Society of America.

Another work introduced combining embedded silicon nanoclusters and a nano-gap in the on-chip resonator with a free-space optical pumping method [153]. Disks are formed on a substrate from silicon-rich silicon nitride (SRSN) film, and nanoclusters are formed from the SRSN film layers using an annealing process. Two disks at a time are arranged atop each other, with a 25 nm nano-gap between them as shown in Figures 2.19(a-b). Sensitivity enhancement is achieved through mode confinement in the nano-gap as presented in Figure 2.19(c). The microdisk array is then formed inside the PDMS microfluidic channel as shown in Figure 2.19(d). Demonstration of the sensor was done using a streptavidin-biotin complex at four different streptavidin concentrations. The chip is set under a focused argon laser (457.9 nm) and resulting spectra are collected at a spectrometer arranged perpendicularly to the resonator as seen in Figure 2.19(e). The Q-factor using the Ar laser was around 15,000 with a sensitivity of 0.012 nm/nM. Resonant shifts can be seen in real-time within a few minutes. The LED source was used in a

simpler setup as shown in Figure 2.19(f), but it was not used for the assay due to possible denaturation of proteins by UV. LED light pumping was reported to have refractive sensitivity of 226.67 nm/RIU.

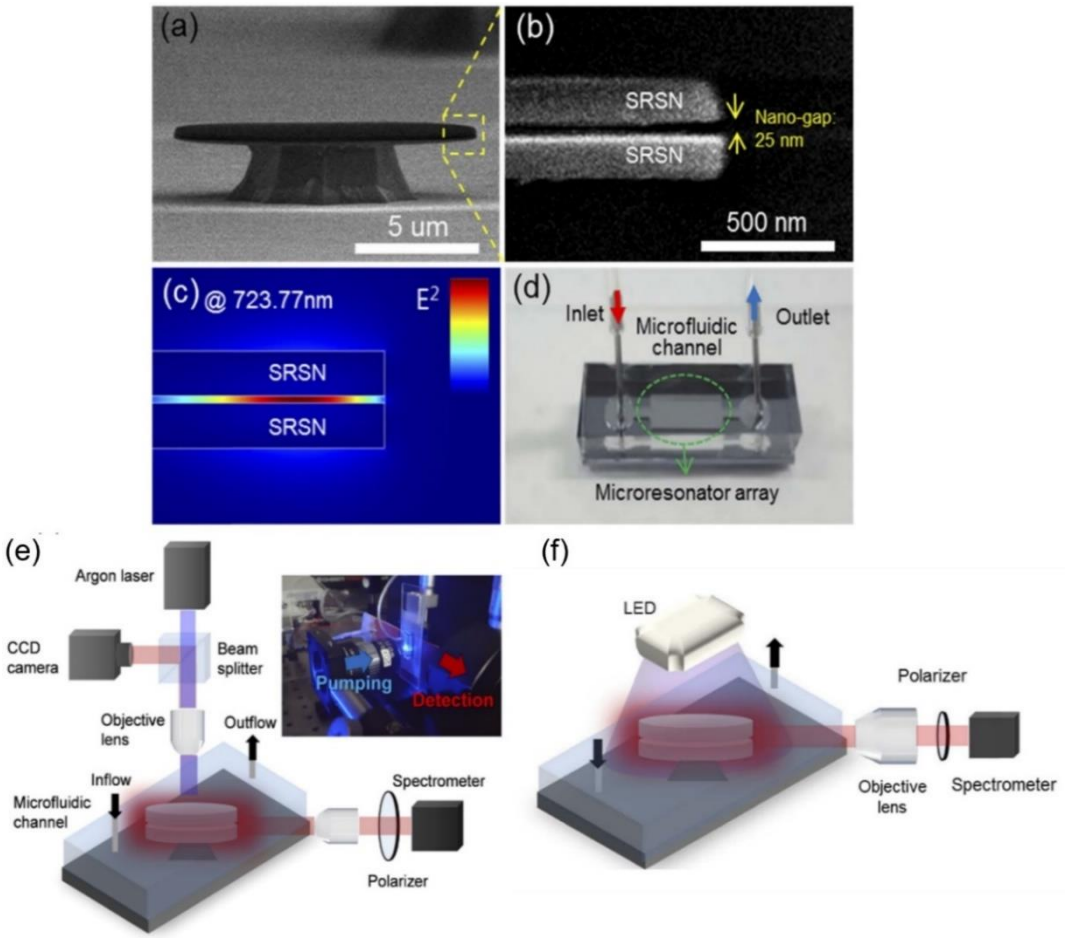

Figure 2.19. (a-b) SEM image of the microdisk resonator with a slot. (c) Intensity profile between the disks. (d) Microfluidic channel with the microdisk arrays. (e) Schematic of the proposed system. (f) Schematic of the system based on LED source. Reproduced from ref. [153] with permission © The Optical Society of America.

In another study, researchers achieved successful label-free, specific detection of *Staphylococcus Aureus* using a lysine K-functionalized WGM microdisk, giving way to an on-site, low cost, and rapid sensor for the virus [137]. Lysine K (Lys-K) is a capture antibody for *S. Aureus*, and it was specific to this bacteria, in an *E. coli*-spiked dilution.

Non-specific detection of bacteria has been demonstrated before, but the specific detection of bacteria in the presence of others is still currently being sought [158, 159]. Silicon microdisks were first fabricated via photolithography followed by buffered oxide and dry etching steps. After, the surface was prepared for binding with hydroxylation, followed by PEG-Amine to attach Lys-K molecules. Transmission spectra were collected at a photodetector coupled to an oscilloscope. A probe wavelength of 630 nm was introduced to the microdisk using a tapered optical fiber. Over the course of 25 minutes, the maximum wavelength shift for *S. Aureus* was 0.22 nm. As anticipated, no shift occurred for *E. coli* detection. Subsequent testing for 4 different concentrations of S. Aureus were performed to determine the LOD. Based on those experiments and estimated surface density, the system was able to detect a minimum of 20 bacteria from a solution of 5 x 10^6 CFU/mL. This translates to a LOD of 5 pg/mL.

Active WGM was demonstrated in a rhodamine-B doped silica microdisk in [140]. One advantage offered by active WGM devices over passive is natural excitation. Active types exploit inherent lasing properties, allowing remote excitation and collection of transmission. The sensor in this work successfully detected BSA and human IgG, in PBS and artificial serum. This is the first work integrating a silica microdisk on a hyperboloid drum (HD) trunk composed of silicon and dye-doped SU8 as the gain medium. Figure 2.20(a) presents the overall structure of the HD and Figure 2.20(b) highlights the simulated mode field location. In their simulations, it was found that a certain wedge angle allowed for greater light-matter interaction and where the lasing occurred. The predicted Q-factor of this resonator was 10^5. For experiments, the whole HD-microdisk surface is functionalized, but the WGMs are confined in the inner drum

where the doped photoresist was. Bulk refractive index experiments were performed and produced a sensitivity of 18.2 nm/RIU. GOPTS (3-glycidoxypropyltrimethoxysilan) was used to silanize the microdisks in preparation for BSA and IgG testing. The corresponding wavelength interrogation results for IgG in both PBS and artificial serum are shown below (Figure 2.20 (c-d)). The detection limits of BSA in PBS and human IgG in both solutions were 4.5 ag/mL and 9 ag/mL, respectively. Compared to other references for their work, the HD microdisk in this study ranks among the lowest detection limits.

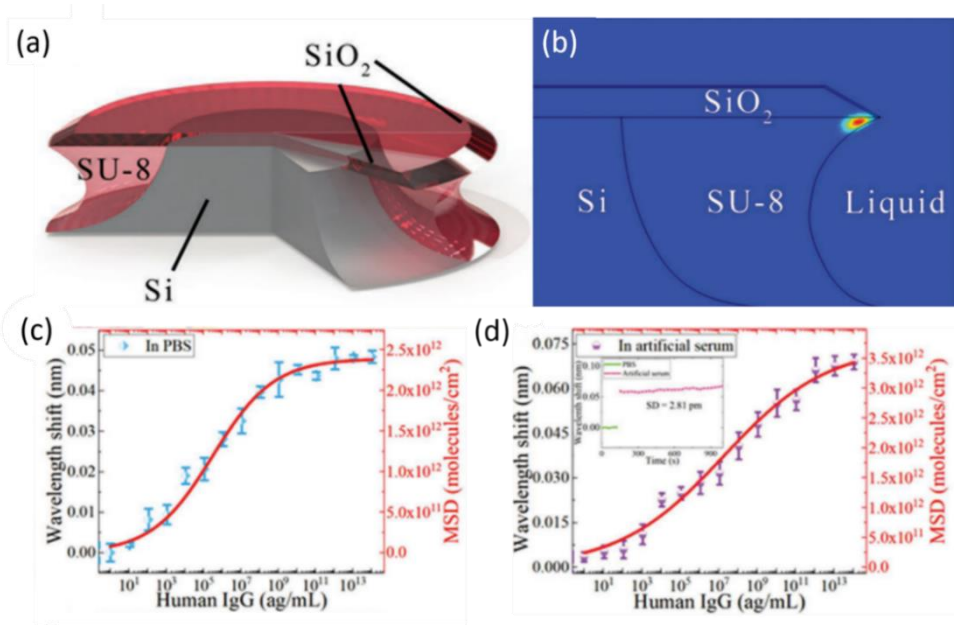

Figure 2.20. (a) HD structure. (b) mode field location based on FEM simulations. (c) Shift in spectrum with human IgG in PBS. (d) Shift in spectra for human IgG in artificial serum. Reproduced from ref. [140] with permission from Wiley.

Another such work doped an aluminum oxide microdisk laser with Ytterbium ions (Yb^{3+}) for active WGM sensing [141]. To fabricate the disks, radio frequency (RF) reactive cosputtering was used to form the Al_2O_3:Yb^{3+} film on silicon. Lithography and a reactive ion etching process were then used to form the desired geometry. Then they were

integrated onto PDMS chips containing microfluidic channels. Bulk refractive index and biodetection tests were performed after being placed to their optical setup. The quality factor of this device was 1.2×10^5 and a sensitivity of 20.1 nm/RIU and LOD of 3.7×10^{-6} RIU were obtained from refractive index tests. A LOD of 300 pM was demonstrated for protein rhS100A4 (a tumor biomarker) in urine as shown in Figure 2.21. One major source of noise discussed in this work was its temperature sensitivity. This temperature sensitivity is less than that of silicon microdisks and its own refractive index sensitivity, however. The refractive index sensitivity for the sensor was 5.74 THz/RIU (6.02 pm/K), while the temperature sensitivity was an order of magnitude less, at 1.72 GHz/K (20.1 nm/RIU).

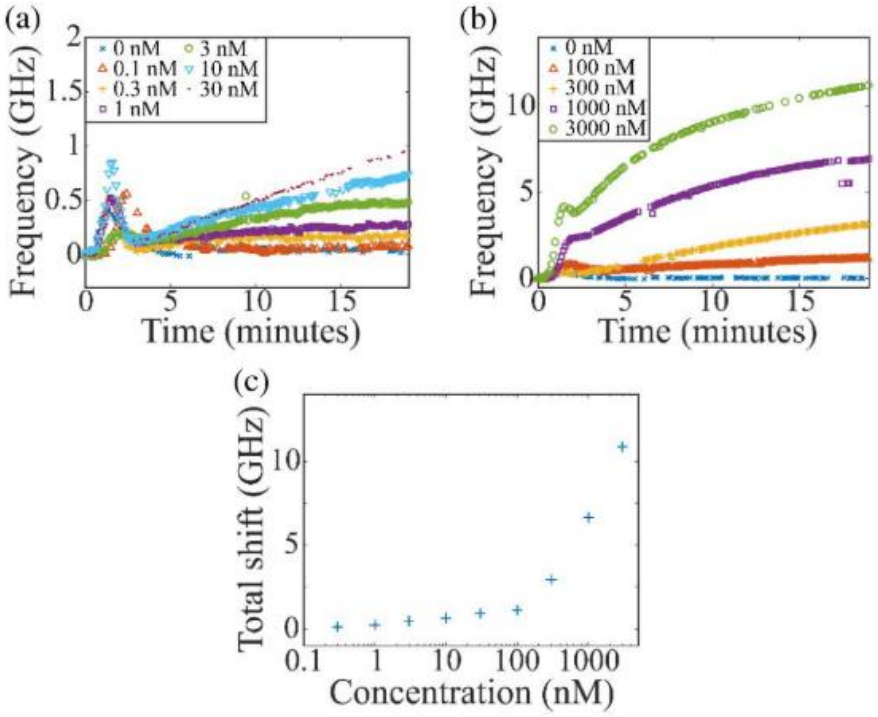

Figure 2.21. Frequency shifts as a result of protein rhS100A4 binding. (a) depicts the low set of concentrations ranging from 0-30 nM, while (b) depicts higher order concentrations up to 3000 nM. (c) is the calibration curve for log concentrations versus the total frequency shift. Reproduced from ref. [141] with permission © The Optical Society of America.

2.2.2. Spherical WGM-based Biosensors

Spherical resonators provide some of the highest Q-factors among other geometries. These are typically based on microbubbles, microspheres, or microdroplets. Some notable modifications were label-free surface functionalization [144, 147, 160, 161], doping [142, 143], and self-referencing [135, 144].

2.2.2.1. Solid microbubble and microsphere WGM-based biosensors. Lead ions were specifically detected using a microbubble and GR-5 DNAzyme functionalization [144]. Fu *et al.* utilized a self-referencing method proven to reduce noise in an earlier separate work by Zhang *et al.* [162]. The self-referencing technique is employed by tracking the transmission from a reference mode, then applying a polynomial fit to produce a repeating saw-tooth pattern that can be subtracted as the "noise" from the sensing mode. With this, the group was able to achieve a LOD for lead ions that is well under the environmentally safe threshold. The microbubble was formed by heating a capillary tube and applying compressed air to expand the center into a microbubble. The bubble's walls were then etched using an acid to thin the walls and allow for the desired mode distribution. The inside of the microbubble was then functionalized using positively-charged poly-L-lysine solution (PLL) bonded to negatively charged GR-5 DNAzyme. Then substrate strands were bound to the DNAzyme strands for lead ion detection. The lead ions were shown to cleave the substrate strands from the surface. For testing, the microbubble and capillary were connected to a syringe to introduce analytes. A tunable laser source supplied light through a tapered fiber coupled to the side of the tube. The wavelength shifts were monitored through the other side of the tapered fiber at a photodetector and data acquisition program. Lead ion solutions of concentrations

ranging from 0.1 pM to 100pM were introduced, which established the sensitivity and LOD for lead in water solutions. The sensitivity was 0.4726 pm/pM and the LOD was 15 fm. The Q-factor was 4.67 x 10^4. Then, to demonstrate specificity, competing ions (Na^+, $Ca2^+$, Zn^{2+}, K^+, Cu^{2+}, Fe^{3+}, Fe^{2+}, and Mn^{2+}) were introduced in equal concentrations to the lead ions, 1 µM. For lead, the wavelength shift exceeded 20 pm, while the rest of the ions did not exceed 1.1 pm shift. Lastly, 100pM lead ion spiked- and non-spiked filtered river water was compared. A blueshift of over 1 pm occurred for the spiked river water, while no significant shift was detected for the non-spiked river water.

Real-time, label-free DNA detection using a PLL functionalized optofluidic microbubble WGM biosensor was demonstrated by Wada *et al.* in 2018 [160]. The system consisted of a tunable laser, filter and polarizers, tapered fiber coupled to microbubble, photodetector and a DAQ software on computer. For their label-free surface preparation following piranha cleaning, the probe ssDNAs are immobilized on the inner wall of the microbubble using PLL through electrostatic binding. Non-complementary, target, and mismatch ssDNA's in PBS buffer solution were introduced to detect the wavelength shift. Real-time shift in wavelength was monitored, and it took about 10 minutes per test. Results show that this device can differentiate between target, non-complementary and mismatch DNA with high selectivity. The LOD of the target ssDNA was 10 nM with a 4.46 pm wavelength shift (Figure 2.22(a)), while the shift for single-nucleotide mismatch and non-complementary strands were 3.28 and 0 pm, respectively (Figure 2.22(b-c)).

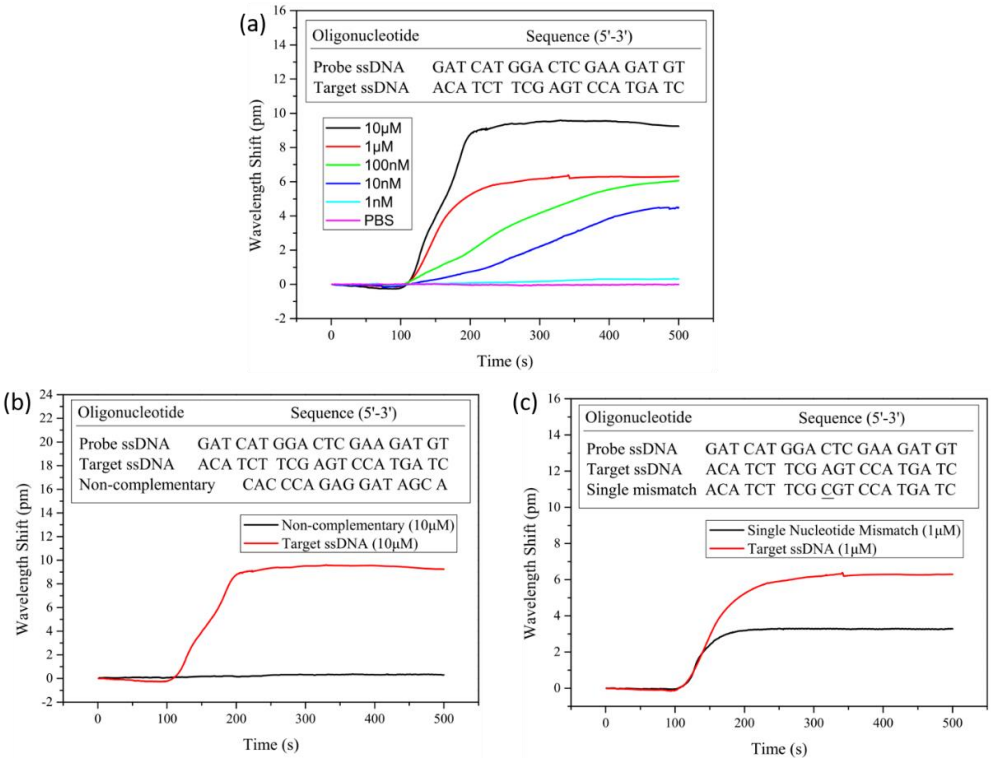

Figure 2.22. (a) Wavelength shifts from Target ssDNA binding over time. (b) Target ssDNA wavelength shift compared to equal concentrations of non-complementary strands and (c) single nucleotide mismatch strands from. Reproduced from ref. [160] with requested permission to SPIE.

In another work, acrylate microspheres are used for label-free, real-time detection toward testing drugs/treatments using a non-invasive approach [147]. Cytochrome C (Cyt-C) is released by Jurkat cells in the body as a response to staurosporine, an anti-cancer drug. It is released upon cell apoptosis. A syringe pump is used to continuously flow the drug solution through a microfluidic chip containing the sample cells. Dying Jurkat cells release the analyte, which flows through a tube to the functionalized, acrylate polymer microbead. The microbead is positioned on a prism. Light from a 1310 nm laser is directed to the prism and bead setup, and the resulting reflected light is received at a photodiode. The microbead is treated by biotin-dextran so that biotinylated antibody-streptavidin compound can be immobilized on the biotin while

dextran passivates the surface to minimize nonspecific binding. An estimated LOD in complex media was 6.82 nM. To demonstrate real-time test capability, the Cyt-C emissions from treated, non-treated, and control cells were monitored over 5 hours. There were significant changes in mass loading over 5 hours for treated cells. A mass loading of over 600 pg/mm^2 was recorded for drug treated cells as a 300 pg/mm^2 increase over the untreated group. The reception of Cyt-C and the increased mass loading from the WGM signal was confirmed by the decrease in cell viability in the MTT (3-(4,5-dimethylthiazol-2-yl)2,5-diphenyltetrazolium bromide) assays which was used an alternate standard to verify the metabolic activity results gathered by the sensor.

2.2.2.2. Liquid crystal microdroplet WGM-based biosensors. A liquid crystal (LC) microdroplet WGM resonator was used to detect heavy metal (HM) ions in real-time [143]. The LC 5CB microdroplet solution was composed of 1% 4-cyano-4'-pentylbiphenyl (5CB) in n-heptane, with equal doping of 0.01% stearic acid and fluorescent dye (DCM). As shown in Figure 2.23(c), one microdroplet was suspended at a time from a tapered microtube in the host solution. Then DCM doped microdroplets were pumped using a frequency-doubled pulse laser, through a tapered single mode fiber. WGM lasing spectra were collected using a spectrometer. Increased environmental pH was shown to change the anchoring state of the 5CB molecules at the LC/aqueous interface and increased the amount of deprotonated stearic acid. Deprotonated stearic acid consequently provides a receptor site for heavy metal ions, as demonstrated in Figure 2.23(a). In this figure, the insets are images of the microdroplet taken using a polarized light microscope, illustrating the anchor state changes of LC as the pH increases without heavy metal ions and then repolarizes upon HM introduction. The WGM lasing spectra

recorded for microdroplet sizes ranging from 30-80 µm for a constant pH, to optimize microdroplet size based on the desired transverse electric (TE) modes. As shown in Figure 2.23(b), the experiments for the detection of copper (II) chloride were conducted for concentrations ranging from 0 to 400 pM using 60 µm droplets, resulting in an LOD of 40 pM, which is substantially less than the threshold set for water quality. Other heavy and light metal ions were also introduced at 400 pM to demonstrate a broad range of functionality as well as specificity to heavy metal contaminants. The most responsive in this system were mercury ions, with the least being magnesium and calcium (little to no toxicity) as presented in Figure 2.23(d).

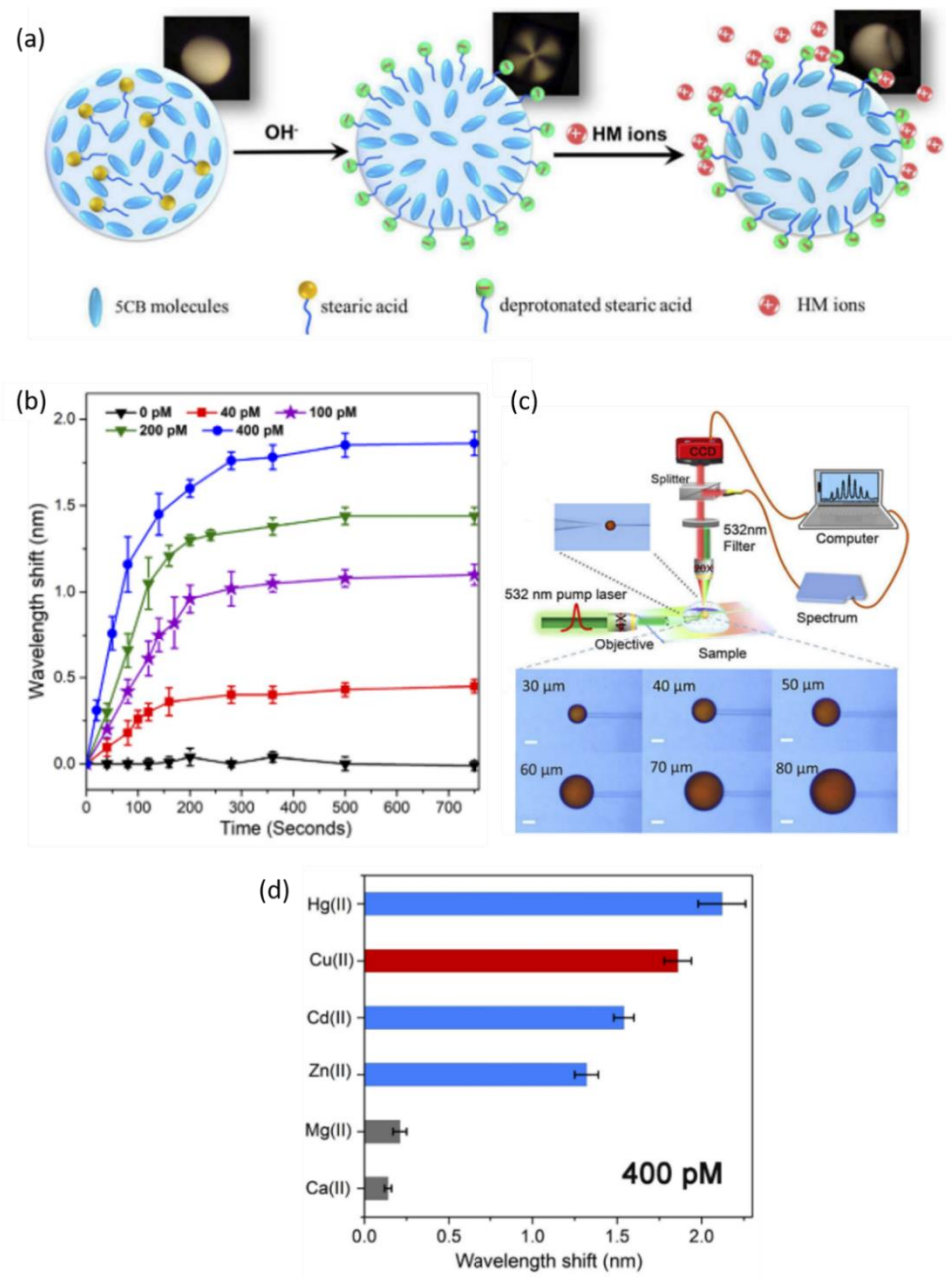

Figure 2.23. (a) Schematic of 5CB microdroplets detecting heavy metal ions. (b) Wavelength shifts associated with increasing concentrations of Cu(II) ions. (c) Schematic of the experimental setup used for HM ion detection. Droplets are fixed to the capillary connected to a syringe pump to control the droplet size in the medium. It is pumped by the laser shown through a tapered optical fiber. (d) specificity results for other heavy metals (blue), Cu(II), and acceptable minerals found in water (gray) at 400 pM concentrations. Reproduced from ref. [143] with permission © The Optical Society of America.

A year later in 2020 [161], the same research group demonstrated urea detection at a LOD of 0.1 mM with the same type of active LC microdroplet-based WGM biosensor using the stearic acid doping method. The same research group also reported urease detection using the LC microdroplet-based WGM resonator alongside a different functionalization method with 4-cyano-4'-biphenylcarboxylic acid (CBA) [151]. CBA was produced through UV exposure of the microdroplet, rather than adding a doping material. The resulting detection limit reported was 0.5 µg/mL. The sensor was specific to urease over other enzymes tested.

In 2019, Duan *et al.* developed an active LC microdroplet-based WGM biosensor for real-time, label-free detection of acetylcholinesterase (AChE) and two pesticides (fenobucarb and dimethoate) [142]. The 5CB is employed again to enhance the WGM response while fluorescent dye DCM is used for active WGM biosensing. Using an automated micropump, the droplets were formed in the medium. A fiber was used to pump light to the microdroplet, and the resulting emission was recorded with a spectrometer. The microdroplet is also visually monitored using a polarized light microscope. AChE hydrolyzes Myristoylcholine (Myr) on the microdroplet surface which in turn changes the orientation of the liquid crystals and the dielectric constant. These changes result in the shift of the WGM lasing spectrum (Figure 2.24(a)) which then can be used to determine the concentration of AChE. As shown in Figure 2.24(b), the detection limit for AChE was found to be 0.0066 U/mL from tests in a range of concentrations. Two pesticides, fenobucarb and dimethoate, are detected with this active LC microdroplet-based WGM biosensor using the inhibitory effects on AChE. In the presence of those pesticides, AChE's function to hydrolyze Myr was limited which was

detected by the WGM lasing spectrum shift. The LODs for the fenobucarb and dimethoate are determined to be 0.1 pg/mL and 1 pg/mL, respectively.

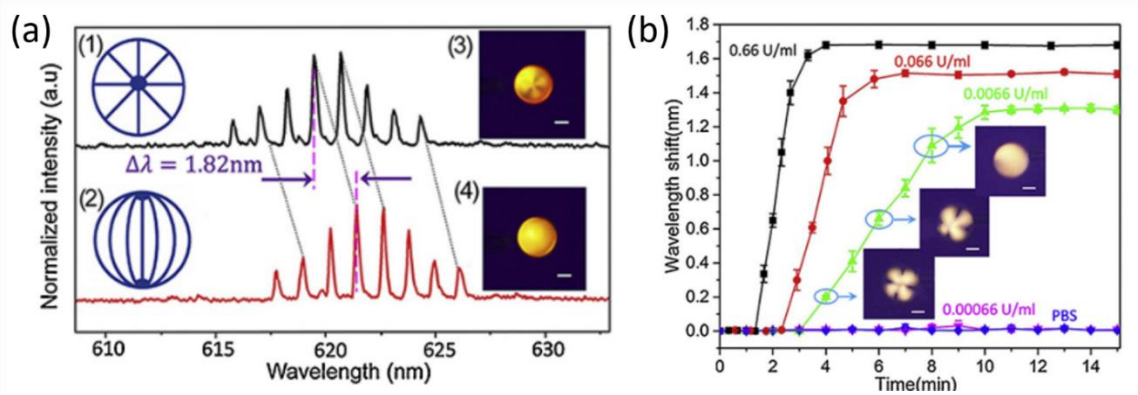

Figure 2.24. (a) Spectral shifts for corresponding configurations. (b) shift response for increasing concentrations of AChE. Reproduced from ref. [142] with permission from Elsevier.

2.2.3. Toroid WGM-based Biosensors

Alternative to the preceding structures is the microtoroid, which have shown to have the highest Q-factors of recent studies, on the orders of 10^5 – 10^7.

Toren *et al*. recently accomplished the detection of Exotoxin A using a microtoroid WGM resonator [163]. Pseudomonas aeruginosa exotoxin A is a viral biomarker commonly indicative of cystic fibrosis (CF). The silicon microtoroids were formed using a UV photolithography, followed by wet and dry etching processes. These were functionalized for biodetection using 3-(trihydroxysilyl) propyl methylphosphonate (THPMP) using EDC in MES, then anti-Exotoxin A was covalently bonded. A 1550-nm laser source was coupled to the microtoroid slide via tapered optical fiber and resonant wavelength shift was measured in real-time as shown in Figure 2.25(a). Baseline and artificial Exotoxin-A spiked sputum samples resulted in spectral shifts of 8.49 pm and 20.04 pm, respectively, within 5 minutes. As shown in Figure 2.25(b), the LOD for

Exotoxin A using their unique surface functionalization method was 2.45 nM, with high specificity in diluted artificial sputum.

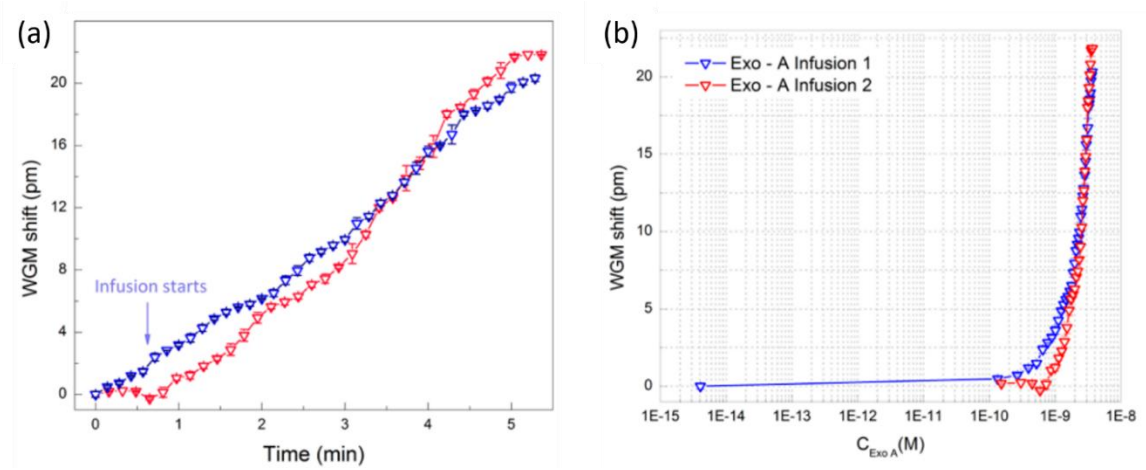

Figure 2.25. (a) Real-time responses of 2 different α-Exotoxin A conjugated microtoroid batches to Exotoxin A infusions in artificial sputum. (b) Wavelength shifts as a function of increased Exotoxin A concentration in artificial sputum. Reproduced from ref. [163] with permission from ACS Publications.

Single-molecule detection was accomplished using a microtoroid-based frequency-locked optical whispering evanescent resonator (FLOWER) with an improved signal-to-noise ratio [62]. This was accomplished using a balanced photodetector, a frequency laser-locking pre-filter, and post filtering in data acquisition. Solutions containing nanoparticles were introduced to the chip via syringe pump. A step-finding algorithm was used for accurate detection of single particle binding events. First, particle detection tests over a range of sizes (2.5 nm was smallest) were performed to characterize their system, then biosensing validation tests using exosomes, ribosomes, mouse IgG, and human interleukin-2 were conducted. The magnitudes of resonance shifts corresponded to the respective nanoparticle sizes and number of binding occurrences. Silica nanoparticles were detected at a minimum concentration of 0.2 pM in water. FLOWER

was later used for the label-free detection of human chorionic gonadotropin (hCG) in simulated urine samples [145]. These researchers also used post processing and electronic feedback control to improve their signal-to-noise ratio. Similar to their earlier work, the frequency of the resonator is tracked during testing and increases the data acquisition rate, rather than constantly scanning a laser wavelength. The disks were fabricated via wet then dry etching processes from silicon wafers with an oxide top layer. Only microtoroids found to have Q-factors of 10^7 or greater were functionalized and used for testing. The toroids were treated with a silane linker, anti-hCG IgG antibody, and then were mounted to the measurement stage. Around this, a chamber was built to house sample fluids, as depicted in Figure 2.26(b). Solutions of hCG and simulated urine were introduced. Instead of repeated solution introduction, hCG was simply infused into the pre-existing solution. After 30s of each infusion, the resonant wavelength was recorded. The measured resonant wavelength shifts (dotted lines) and their corresponding linear fittings (solid lines) are depicted in Figure 2.26(a). Figure 2.26(c) is the concentration curve developed from the aforementioned test, resulting in a LOD of 120 aM. Subsequently, real human urine samples diluted in the same simulated urine were tested. The lowest detectable hCG concentration with simulated and human samples were 1 fM and 3 fM, respectively.

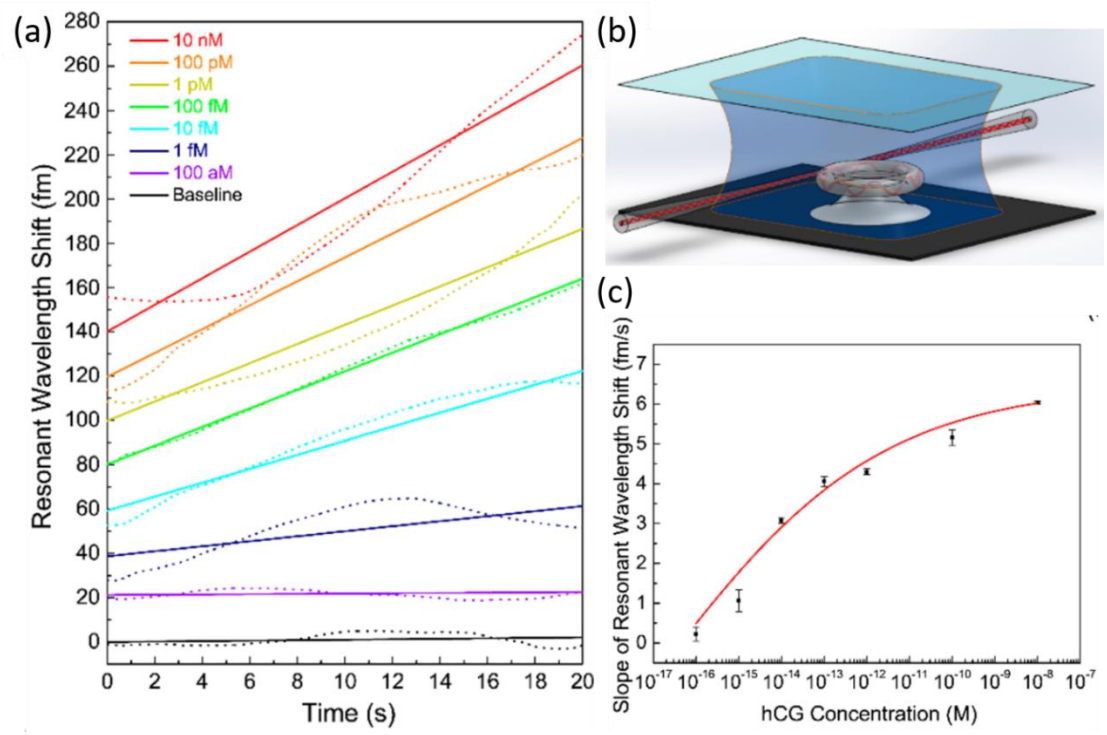

Figure 2.26. (a) Corresponding wavelength shifts over 20 sec for concentrations of hCG, ranging from 100 aM to 10 nM. (b) Schematic of the microtoroid chamber and optical fiber. (c) concentration curve resulting from (a). Reproduced from ref. [145] with permission from ACS Publications.

2.2.4. Capillary-based WGM Biosensors

Capillary, or fiber-based WGM sensors have also been explored due to their ease of integration with microfluidics, large binding surface area, and high Q-factor [146, 164]. Using a microcapillary (MC) fabricated from optical fiber, Wan *et al.* [164] were able to detect the concentration of glucose. The wall thickness of the capillary was optimized for sensitivity, based on the FDTD method for a capillary filled with a fluid. The MC was fabricated using an inflation and tapering method to achieve the dimensions depicted in Figure 2.27(a). The capillary was excited using a tapered optical fiber attached to the tunable laser source. Spectra were recorded at a photodetector. The baseline sensitivity of 23.36 nm/RIU was established by introducing blank fluids of

increasing refractive index. Once the capillary was functionalized using glucose oxidase and coupled to the fiber, fluids are introduced via a syringe pump. Transmission was monitored for a range of glucose concentrations from 2.78 to 16.67 mM as shown in Figure 2.27(c). This produced a sensitivity of 0.966 pm/mM; the respective concentration curve is depicted in Figure 2.27(b).

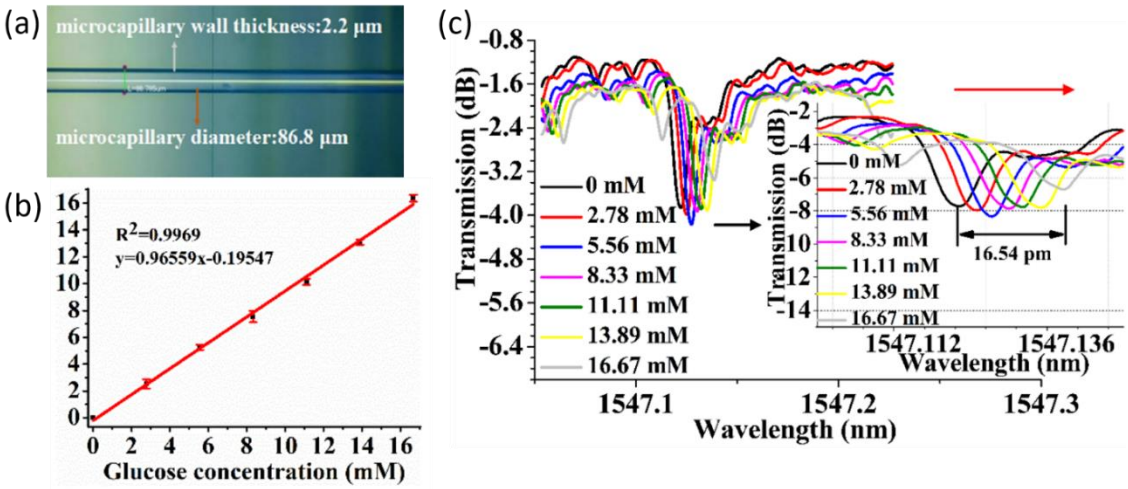

Figure 2.27. (a) Microscope image of the microcapillary resonator. (b) linear fitting for glucose concentration test performed in (c). (c) Measurement results for glucose detection. Reproduced from ref. [164] with permission © The Optical Society of America.

Using a biocompatible MC integrated with a microfluidic channel, Wang *et al.* were able to monitor conformational changes of G-quadruplex in real time [146]. The use of a MC to monitor DNA restructuring alleviates challenges associated with labeling and complex detection systems. G-quadruplex is currently being studied in other works for their role in cancer therapies. The folding of potential G-quadruplex forming sequences (PGQS), or formation of G-quadruplex, is involved in oncogene regulation [165]. After thinning the walls of a silica capillary with hydrofluoric acid, it was silanized, then PGQS were immobilized using streptavidin-biotin conjugate. The capillary was fixed to a glass

slide, and connected to a syringe pump by polyethylene tubing. Light from a tunable laser was coupled into the MC by a tapered optical fiber. Transmission was received at an optical power meter. A sensitivity of 995.63 nm/RIU was derived from simulation. K^+ ions of increasing concentrations were introduced to induce folding of PGQS into the stable G-quadruplex structure, and the resulting wavelength shifts were collected. As more ions were introduced, the slope of the relative wavelength shift over time decreased from -18.85 x 10^{-5} nm/s at 1 µM KCl, to -2.03 x 10^{-5} nm/s at 10000 µM KCl, due to reduced unfolded, single-stranded oligonucleotide availability as the experiment progressed. This work demonstrates the ability of a silica microcapillary WGM sensor as alternative candidate in the future for monitoring bodily responses to drug treatment.

CHAPTER THREE

Optical Cavity-based Biosensor: Proof-of-Concept

This chapter published as: D. Rho and S. Kim, "Low-cost optical cavity based sensor with a large dynamic range," *Optics Express*, vol. 25, no. 10, pp. 11244-11253, May 15 2017, doi: 10.1364/OE.25.011244 [171],
D. Rho and S. Kim, "Label-free real-time detection of biotinylated bovine serum albumin using a low-cost optical cavity-based biosensor," *Optics Express*, vol. 26, no. 15, pp. 18982-18989, Jul 23 2018, doi: 10.1364/OE.26.018982 [169].

Receiving an accurate diagnosis and treatment at an early stage are the most essential steps in curing cancer and other disease. Figure 3.1 shows the relationship between the 5-year survival rates, the percentage of patients who live at least 5 years after their cancer is diagnosed, and the stage when cancer is diagnosed. For all types of cancers in the figure, the chances for survival become greatly lowered if they are diagnosed at an advanced stage, and this fact clearly demonstrates the importance of early detection.

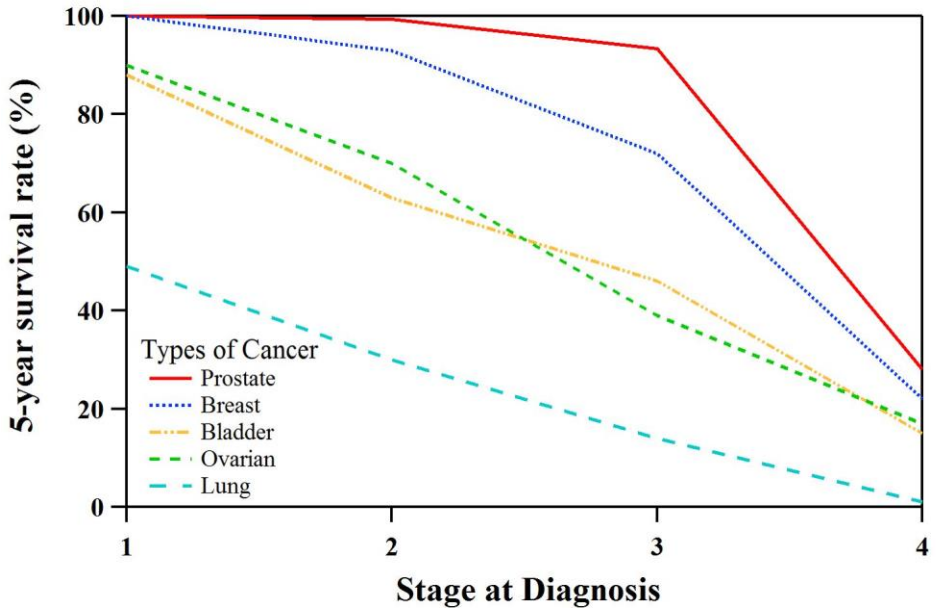

Figure 3.1. 5-year survival rates versus the stages of cancer at diagnosis [166].

With the current clinical diagnostics which are usually performed at centralized laboratories involving specialized staff, costly and time-consuming processes, people are experiencing difficulties having regular medical checkups for their health condition and exposed to the chance of being diagnosed with cancer at late stage. The situation becomes worse for people who are in financial difficulties or living in underdeveloped countries where medical facilities are limited. To address these issues, the development of a diagnostic device which can be easily and cheaply used by people is required, and a POC biosensor would be an effective solution for early detection of diseases. The most popular examples of commercially available point-of-care biosensors are the blood glucose monitoring devices and pregnancy test strips.

We have proposed an optical cavity-based biosensor (OCB) using a differential calculation for the application of point-of-care diagnostics [167-173]. This means our design aims to have high sensitivity, multiplexability, and easy integration with a microfluidic system and be label-free, low-cost, portable, and stand-alone. The final diagnostic device from our research will be beneficial in the field of medical diagnostics by providing the aforementioned advantages toward point-of-care applications. To demonstrate our system with standardized materials without ambiguity, we have firstly performed refractive index measurements using standard refractive index liquids (Cargille) in the range 1.3–1.395 with an interval of 0.005. The optical cavity structure is designed to provide a linear change in differential values near the refractive index of 1.33 that is close to the refractive index of typical biological sample fluids [174, 175].

3.1. Refractive Index Detection

3.1.1. Schematic

Figure 3.2 shows a schematic diagram of the optical cavity sensor [171]. Two laser diodes are used as light sources at wavelengths of 780 nm and 850 nm. These are chosen from available low-cost off-the-shelf laser diode wavelengths such as 780 nm, 808 nm, 832 nm, 850 nm, 880 nm, 904 nm, and 980 nm. After the light waves from the laser diodes are collimated using collimators, they are combined by a 50:50 ratio beam splitter. The light waves propagate through the optical cavity structure along the same path and reach the CMOS camera. The images captured by the camera are then processed to determine the intensities for both wavelengths.

The equation to calculate differential value using the measured intensities is given by

$$\eta = \frac{I_1 - I_2}{I_1 + I_2} \tag{3.1}$$

where I_1 and I_2 are the optical intensities of 780 nm and 850 nm laser diode, respectively. A differential detection method has been used to enhance the signal change and improve the dynamic range [171, 172]. In the range where I_1 and I_2 are changing in opposite directions, the change in the differential value using Equation 3.1 is enhanced. We employ it for the optical cavity sensor to improve the responsivity (i.e., the slope of the quantity used for either biosensing or refractive index measurement) of the proposed low-cost system.

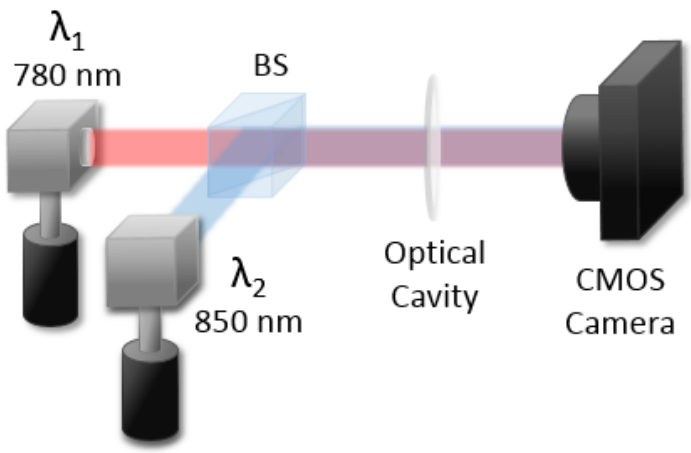

Figure 3.2. Schematic diagram of proposed optical cavity biosensor [171].

3.1.2. Simulation Results

The optical cavity structure for the two-laser system is optimized for refractive index measurements using FIMMWAVE /FIMMPROP (Photon design) so that intensities (or efficiencies for the simulation) of 780 nm and 850 nm change in the opposite directions near the refractive index of 1.33. Figure 3.3 shows the simulation results of the optimized structure, which has a cavity width of 2.2 μm and a silver thickness of 8 nm. The differential value has a linear change with a slope of 30.743/RIU (refractive index unit) in the refractive index range of 1.32 and 1.345 ($\Delta_{diff} = 0.025$). We defined the dynamic range (Δ) as the refractive index range where the measured or calculated quantity is changing linearly. Compared to the slope and the dynamic range of the differential value, the efficiencies of 780 nm and 850 nm have smaller slopes (17.241/RIU and 18.028/RIU, respectively) in the smaller dynamic ranges of 1.336–1.354 ($\Delta_{780} = 0.018$) and 1.316–1.334 ($\Delta_{850} = 0.018$), respectively. Therefore, the differential detection method results in a larger responsivity and a larger dynamic range than the efficiency of an individual wavelength.

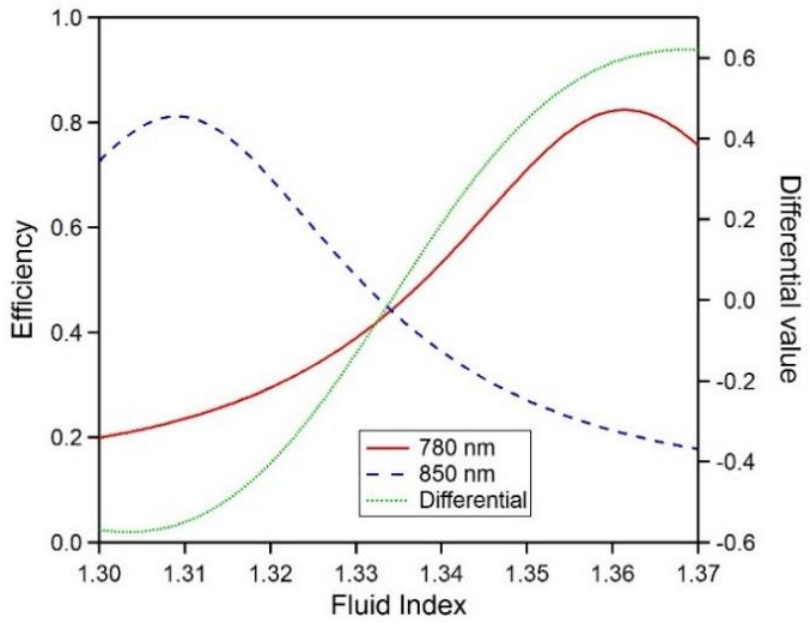

Figure 3.3. Efficiencies of 780 nm and 850 nm and the differential value of the optimized optical cavity structure for the two-laser system in the refractive index range of 1.3–1.37 (red solid line: efficiencies of 780 nm, blue dashed line: efficiencies of 850 nm, and green dotted line: differential values).

3.1.3. Fabrication Process

The optical cavity for the refractive index measurement is fabricated using photolithography and an SU-8 to SU-8 bonding process [168]. The fabrication process is illustrated in Figure 3.4. The first step is drilling holes for the inlets and outlets of index fluid on the 4-inch glass substrate. After the cleaning process, the drilled glass substrate and a glass slide are sputter coated with silver in order to make two partially reflecting mirrors. Subsequently, channels are fabricated on the glass slide using SU-8 2002 negative photoresist. SU-8 2002 is spun on the top of a silver layer, and soft baked on a hot plate. Then, SU-8 layer is placed in the mask aligner and exposed to UV light through the designed mask to define the fluidic channel. Next, the UV exposed SU-8 layer is heated again on the hot plate for the post exposure bake. Then it is immersed in SU-8

developer for removing the unexposed area of the SU-8 layer. The developed SU-8 layer is rinsed with IPA and blown dry.

SU-8 2000.5 is spun on a glass substrate with holes in order to create an SU-8 bonding layer. The holes of the glass substrate and patterned fluidic channels on the glass slide are aligned and sandwiched together. To make strong SU-8 to SU-8 bonding, the sandwiched sample is placed on the hotplate at the temperature above the glass transition temperature of the SU-8. During the heating, we applied pressure manually around the channel to form a strong bond. Once the bonding process is done, metal pins connected with tubes are attached to the other side of the glass substrate by applying epoxy glue around the interconnection holes.

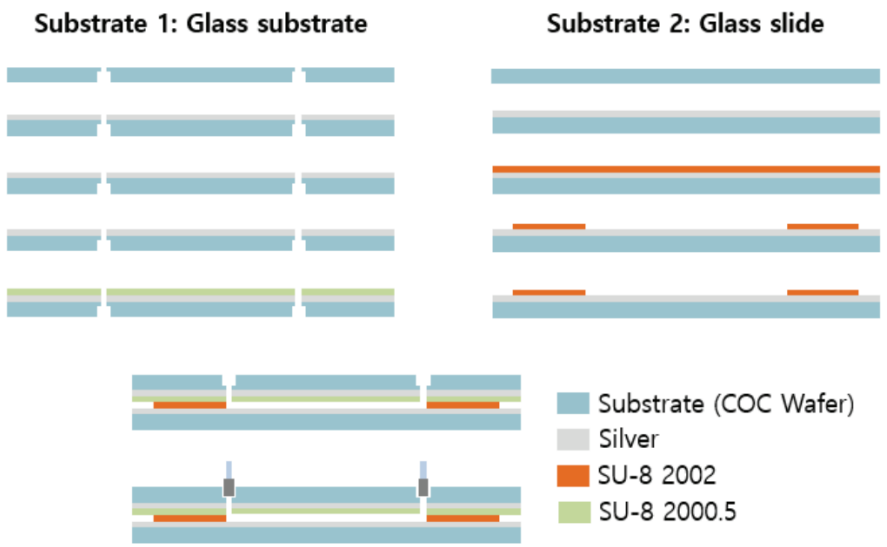

Figure 3.4. Fabrication process of the optical cavity structure [168].

3.1.4. Test Setup

Figure 3.5 shows the test setup for the refractive index measurements. Two laser diodes with collimators, beam splitter, sample with sample holder, and sCMOS camera

are placed on the optical table. Computer controlled laser diode drivers control the laser diodes. For measurements, we first found the fluid channel of the fabricated sample which was mounted in a 3-D printed sample holder. We collected the CMOS images before we introduce sample fluids. Next, the channel was filled with an index fluid by the use of a syringe pump. After an index fluid filled the channel, we took images for the two wavelength lasers again in order to get the intensities and a differential value. We continued this process until we completed the measurements.

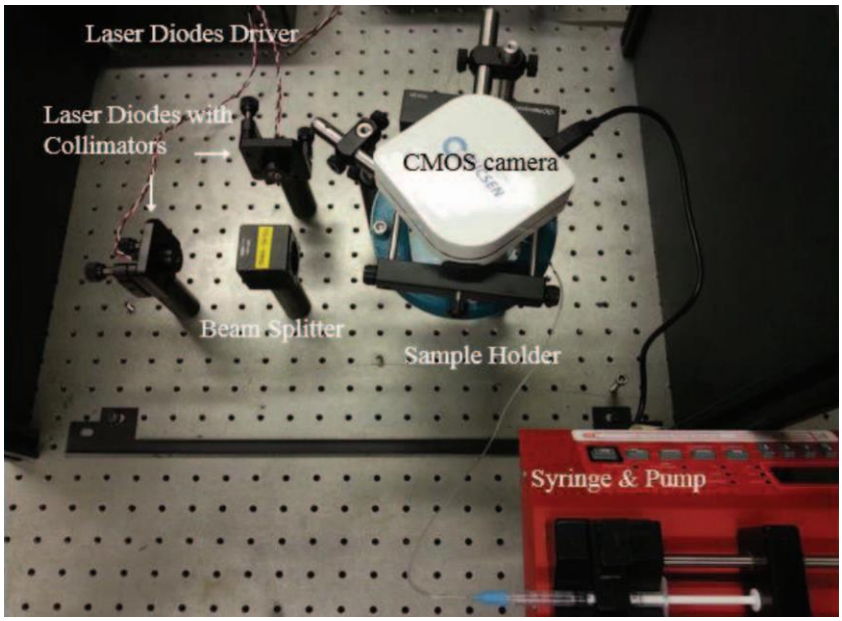

Figure 3.5. Test setup for the refractive index measurement.

3.1.5. Measurement Results

Once a refractive index fluid filled the fabricated optical cavity, we collected 170 CMOS images for about one minute for 780 nm laser diode and calculated the average intensity over an area of 150 x 150 pixel array near the center of the beam. Then, we repeated this process for 850 nm. The differential value was calculated using average intensities of 780 nm and 850 nm. This procedure was repeated for different refractive

index fluids until the measurement was completed. Figure 3.6 shows the measured intensities of both laser diodes and calculated differential values as a function of the refractive index of liquids. As the refractive index is changing from 1.315 to 1.35, the intensity of 780 nm is increasing while the intensity of 850 nm is decreasing, which is consistent with the simulation results. The calculated differential value has a linear region between the refractive index of 1.32 and 1.345 with a slope of 32.943/RIU. These measurement results match very well with simulation results. The results shown in Figure 3.6 include error bars with standard deviations from collected 170 CMOS images, but it is too small to appear.

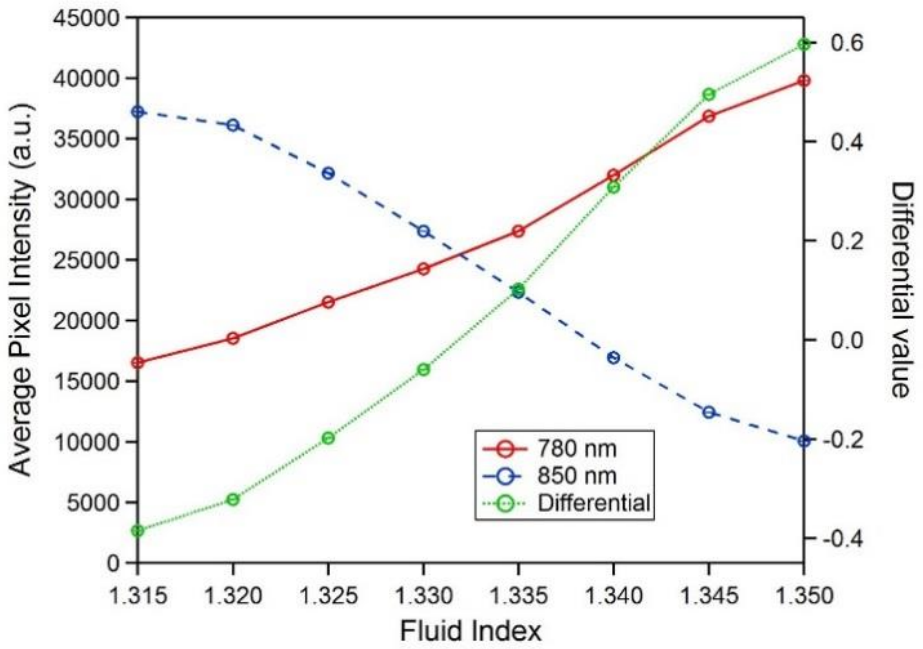

Figure 3.6. Measured results of the optical cavity sensor with the two-laser system as a function of refractive index from 1.315 to 1.35 (red solid line: 780 nm, blue dashed line: 850 nm, and green dotted line: differential value).

3.2. Biotinylated-BSA Detection

3.2.1. Schematic

A schematic diagram of the proposed OCB is shown in Figure 3.7(a) [169]. As described earlier, 780 nm and 850 nm laser diodes are collimated, combined with a beam splitter, and propagate through the optical cavity. Figure 3.7(b) shows the cross-sectional view of the optical cavity structure including a spin-on-glass (SOG) layer on top of top and bottom silver layers. SOG layers are coated to maximize intensity changes upon the binding of the target analytes on the receptor molecules, facilitate the surface functionalization process, and protect the silver films from possible damages during the sample fabrication process and test. For designing the optical cavity structure, we employed the fixed index model [176]. The fixed index model uses a refractive index value for the sensing layer and its thickness corresponds to the number of the biomolecules on the sensing area. The initial sensing layer thickness is 0 (no biomolecule is bound) and it changes up to the monolayer thickness of the biomolecules (the sensing area is fully occupied by the biomolecules). We used 1.45 for simulations as the refractive index of the sensing layer [177-180].

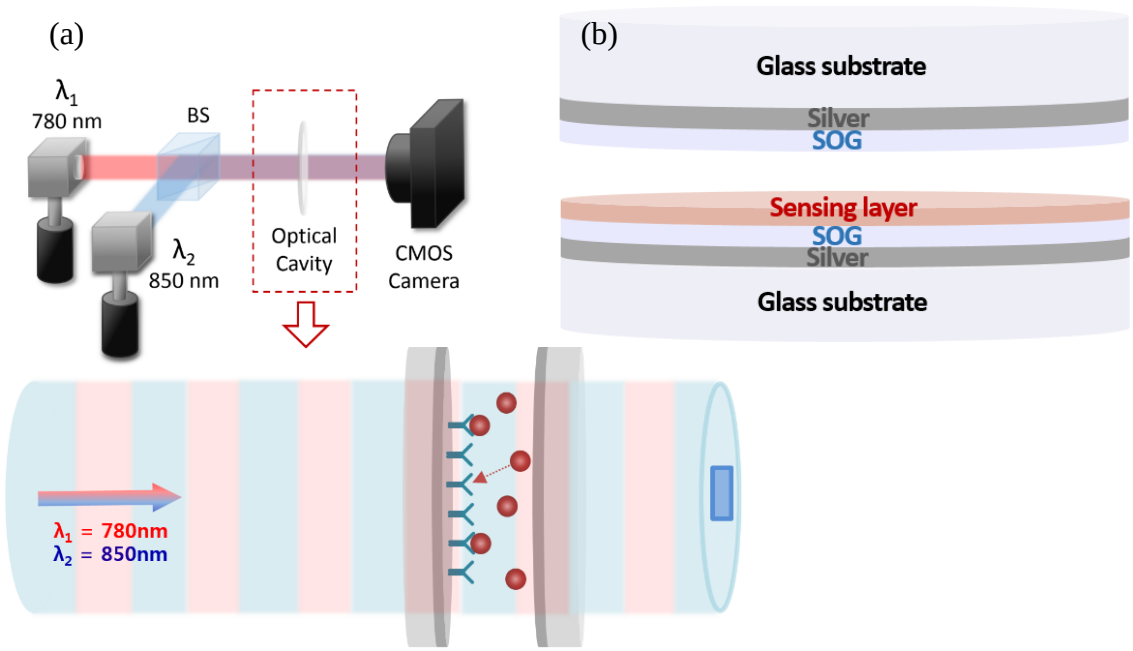

Figure 3.7. (a) Schematic diagram of the proposed biosensor. (b) The optical cavity structure [169].

3.2.2. Simulation Results

We employed the differential detection method for which differential values (η) are calculated with an equation shown below, which is simply the difference of the intensity rate changes of two wavelengths.

$$\eta = \frac{I_1 - I_{10}}{I_{10}} - \frac{I_2 - I_{20}}{I_{20}} \tag{3.2}$$

I_1 and I_2 are the optical intensities at 780 nm and 850 nm wavelengths, respectively, and I_{10} is the initial value of I_1 while I_{20} is the initial value of I_2. The optical cavity structure is designed specifically for two wavelengths' intensities to change in opposite directions as the sensing layer thickness increases. Therefore, the differential detection method enhances the responsivity (i.e., the change due to the increase of the sensing layer thickness). In addition to the enhanced responsivity, differential values always start at

zero regardless of the intensities of two laser diodes by equalizing intensity levels of two wavelengths, which helps to obtain consistent results between tests.

The optical cavity structure is optimized to have the most changes in intensities of two wavelengths in opposite directions for the sensing layer thickness change from 0 nm to 20 nm. The final optimized design has a cavity width of 2.5 μm, a silver thickness of 14 nm, and a SOG thickness of 100 nm. The simulation results of the optimized optical cavity structure are shown in Figure 3.8. As the sensing layer thickness increases, the efficiency of 780 nm increases linearly from 0.1613 to 0.1809 (ΔI_1 = 0.0195), and the efficiency of 850 nm decreases linearly from 0.1859 to 0.1616 (ΔI_2 = 0.0243). For the same range, the calculated differential value changes from 0 to 0.252, which is more than ten times greater than the changes in both wavelengths.

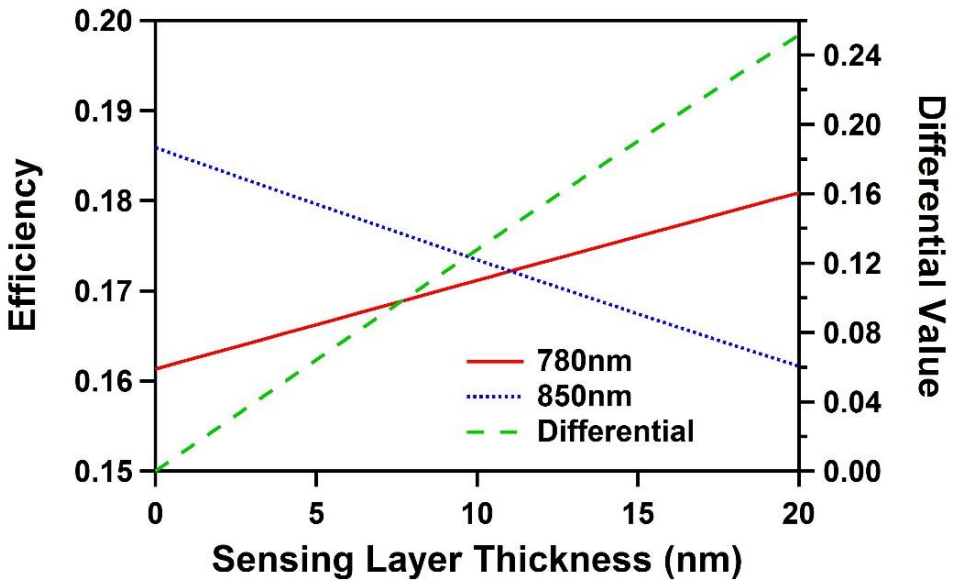

Figure 3.8. Efficiencies of 780 nm (red) and 850 nm (blue) and differential value (green) vs. the sensing layer thickness.

3.2.3. Fabrication Process and Experimental Process

The fabrication process of the OCB structure is shown in Figure 3.9 [169]. A 3-inch glass substrate was drilled using a 1 mm drill bit to make a channel inlet and an outlet. Thin silver layers were deposited on both the drilled glass substrate and one plain glass substrate. SOG was spin-coated on the silver layer of both substrates and cured on a hot plate. On top of the SOG layer of the plain glass substrate, an SU8 layer was patterned using a photolithography process to define the microfluidic channel and the gap between SOG layers. We then used an UV curable epoxy (Norland Products) to bond the drilled and plain glass substrates. The UV epoxy was spin-coated on a glass substrate. The SU8 pattern was stamped on the UV epoxy layer, and then aligned and brought into contact with the drilled glass substrate followed by UV exposure [181].

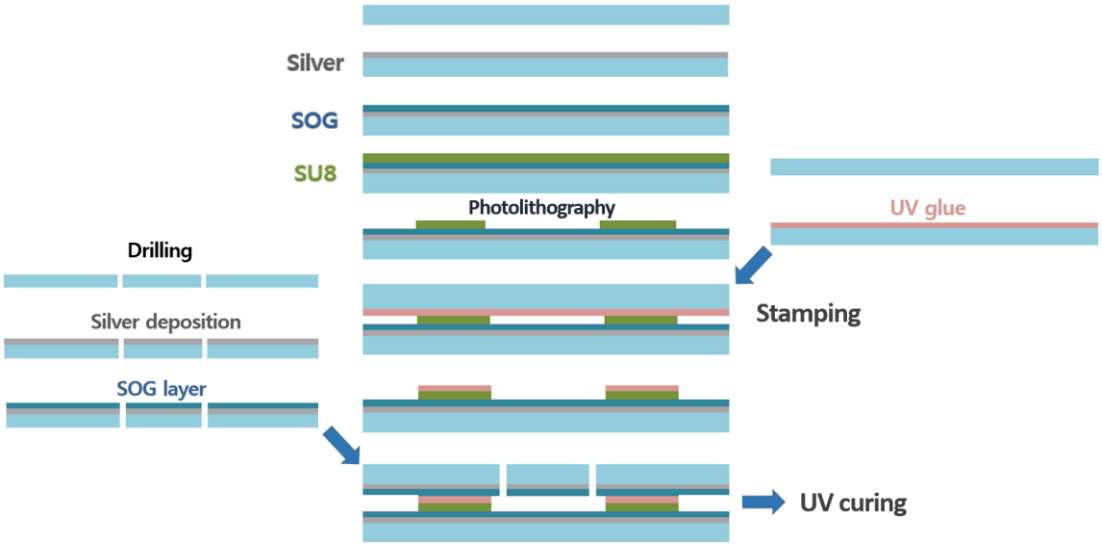

Figure 3.9. Fabrication process of the OCB structure [169].

Before the UV bonding, the SOG surface of the glass substrate with the SU8 pattern was treated with oxygen plasma to increase the number of hydroxyl groups. Then, 5% of 3-aminopropyltriethoxysilane (APTES) was applied to the center area of the

channel (i.e., sensing area) and incubated for 30 minutes to form APTES layer on the SOG surface. The unbound APTES molecules were then rinsed out with DI water. After the bonding, 2 μL of streptavidin is introduced into the channel and incubated for an hour to allow bonding to the APTES via electrostatic interactions [182]. After the incubation, unbound streptavidin was rinsed out by flowing DI water with a vacuum pump. Finally, 2 μL of biotinylated BSA with a concentration of 3 μM was introduced and incubated for 50 minutes while we were performing the real-time measurements. Streptavidin and biotinylated BSA were diluted in DI water, and Tween-20 with a concentration of 0.2% was added to all fluids to facilitate fluid flows. Each functionalization step was experimentally confirmed by using fluorescent streptavidin and biotin with a fluorescent microscope beforehand.

3.2.4. Test Setup

Figure 3.10 shows the test setup on an optical table including two laser diodes with collimators at the wavelength of 780 nm and 850 nm, a 50:50 beam splitter, a mirror, a fabricated optical cavity sample placed in a 3-D printed sample holder, a 3-D printed beam blocker operated by a servo motor, and a CMOS camera. The beam blocker rotates to alternately block the light from one laser diode at a time at one-second intervals. This allows us to monitor both intensities with a CMOS camera and calculate differential values in real-time. Total cost of the test setup with off-the-shelf products is ~$1,000 (excluding optical mounts and posts). The fabrication process is very simple and does not require expensive equipment or materials as described in Figure 3.9. Therefore, the proposed OCB is a low-cost system.

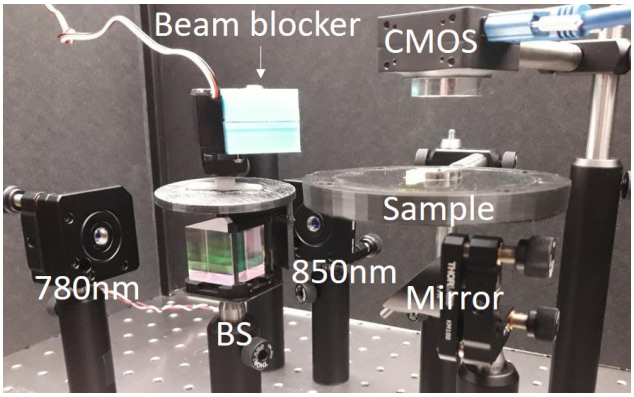

Figure 3.10. Test setup for biosensing with the OCB.

3.2.5. Measurement Results

The fabricated optical cavity sample is aligned for both collimated beams of two wavelengths to pass through the center area of the microfluidic channel. The area of a 50 × 50 pixel array from the CMOS images near the center of the microfluidic channel was selected as a sensing area, and further processing was performed only in that area. Because the size of a pixel of CMOS camera is 3.6 μm × 3.6 μm, the total sensing area is 180 μm × 180 μm. Figure 3.11 shows the average intensity values of 780 nm and 850 nm in the sensing area with the calculated differential values during the biotinylated BSA incubation time. There was not much change in the first 10 minutes. However, both 780 nm and 850 nm show changes after 10 minutes where we believe the binding of biotinylated BSA on streptavidin started. As expected in the simulation results shown in Figure 2, the intensity of 780 nm is increased while the intensity of 850 nm is decreased. The total change of differential value over 50 minutes incubation time is 0.179. Compared with the simulation results, the differential value of 0.179 corresponds to the sensing layer thickness of 14.1 nm. Considering the estimated size of a BSA molecule is

4 nm × 4 nm × 14 nm [183], the measurement results of biotinylated BSA sensing match very well with the simulation results.

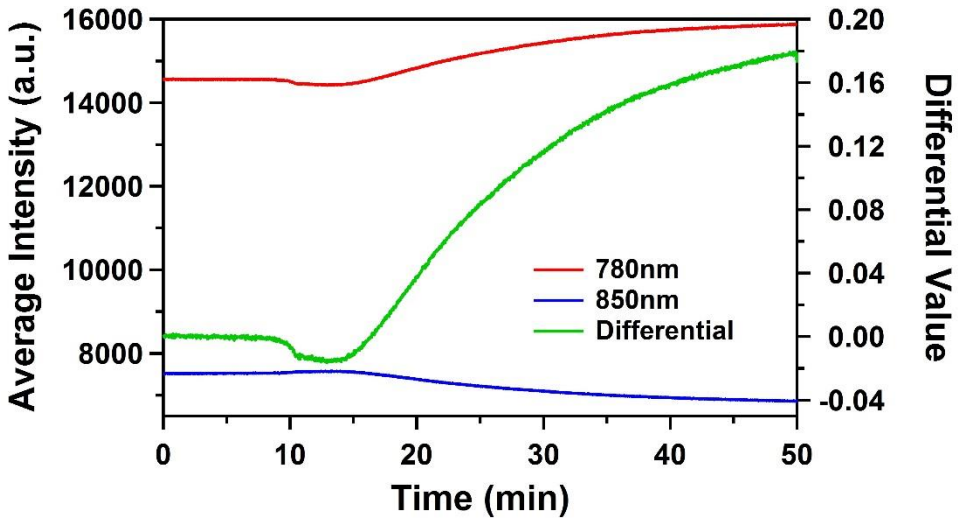

Figure 3.11. Measured average intensities for 780 nm (red) and 850 nm (blue) and corresponding differential values (green).

Based on the measurement results, we attempted to estimate the limit of detection (LOD). Even though we used a high concentration of biotinylated BSA (3 μM) for this experiment, we only need enough molecules to fill the sensing area to get the exactly same results we got. Since the sensing area is 180 μm × 180 μm, the required number of biotinylated BSA molecules to fill the sensing area is then 2.025×10^9, assuming 4 nm × 4 nm side of the biotinylated BSA molecules are densely packed and create a monolayer on the surface. This corresponds to 3.36 femtomole based on the Avogadro's number, 6.022×10^{23}. By using the volume of the sample fluid containing biotinylated BSA used (2 μL), the minimum concentration to fill the sensing area assuming all biotinylated BSA reach to the sensing area is 1.68 nM. Based on the measurement results shown in Figure 5, the calculated standard deviation for the first 5

minutes is 1×10^{-4} and the corresponding minimum detectable change is 3×10^{-4}. Therefore, based on the differential value change of 0.179, the minimum concentration of 1.68 nM, and the minimum detectable change of 3×10^{-4}, the estimated LOD is 2.82 pM. In summary, if we use 2 μL of sample fluid with 1.68 nM concentration of biotinylated BSA, we will be able to see the differential value change of 0.179 as long as we incubate long enough for all biotinylated BSA molecules reach to the sensing area. However, even a concentration as small as 2.82 pM will produce a detectable change with the OCB for the 180 μm × 180 μm sensing area, assuming all biotinylated BSA reaches to the sensing area. This LOD can go down further with a smaller sensing area, even in the fM range, with the tradeoff of a longer incubation (i.e., sensing) time.

This low-cost OCB not only has label-free real-time detection capability with high sensitivity, but also multiplexability. Figure 3.12 show differential values of a 50 × 50 pixel array at t=0, 17, 30, and 50 minutes. These images show the biotinylated BSA binding does not happen uniformly across the sensing area over time, and 50 minutes incubation time may not be sufficient to cover the entire sensing area. In addition to that useful information, these images show we can extract information in a local pixel area as small as one single pixel. Therefore, these images clearly prove that, by properly immobilizing various biomarker-specific receptors on different locations within the sensing area, we can detect the multiple target biomarkers in the sample fluid simultaneously.

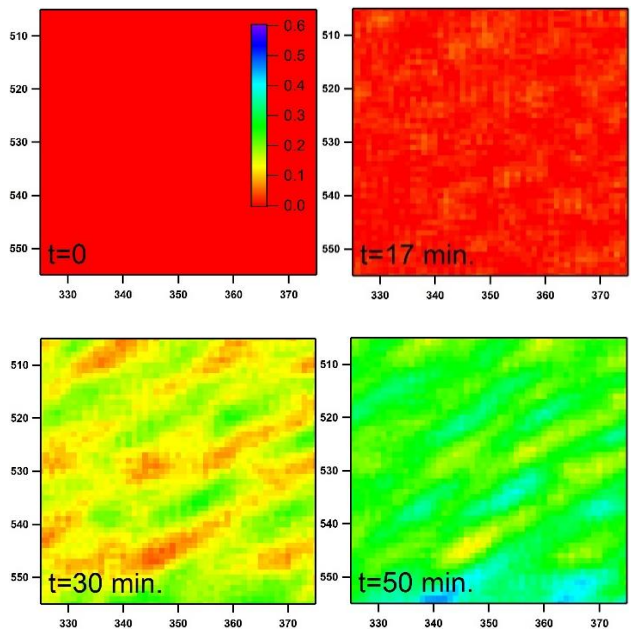

Figure 3.12. The intensity changes in the sensing area for the differential value at 0, 17, 30, and 50 minutes.

CHAPTER FOUR

Demonstration of Biosensing Capability of Optical Cavity-based Biosensor

This chapter will be published as: Donggee Rho and Seunghyun Kim "Demonstration of a label-free and low-cost optical cavity-based biosensor using streptavidin and C-reactive protein"

We demonstrated the OCB with streptavidin and C-reactive protein (CRP) and determine the limit of detection (LOD) for them. The optimized optical cavity design with simulations, surface functionalization steps, testing procedures, and measurement results are discussed in this chapter.

4.1. Schematic

An improved schematic of the OCB is shown in Figure 4.1(a). Two low-cost laser diodes at different wavelengths are used as light sources operated by laser diode drivers with the constant current mode. The laser beams are collimated, combined by a 50:50 beam splitter (BS), and alternatively propagating with one-second intervals using a rotating beam blocker. A neutral filter (NF) is placed in the light path to attenuate the intensities of laser beams in order to avoid saturation of a CMOS. Figure 4.1(b) shows each layer of the OCS structure, while Figure 4.1(c) shows the cross section of it. The receptor molecules are functionalized at the center area of the microfluidic channel, creating a sensing area. To introduce fluids to the OCS without air bubbles, a syringe pump is used to add drops of fluids into the 3D printed input port (volume capacity: 20 μL) through a bent syringe tip, while a low-cost vacuum pump is attached to the 3D

printed output port through tygon tubing to pull fluids from the input port through the microfluidic channel.

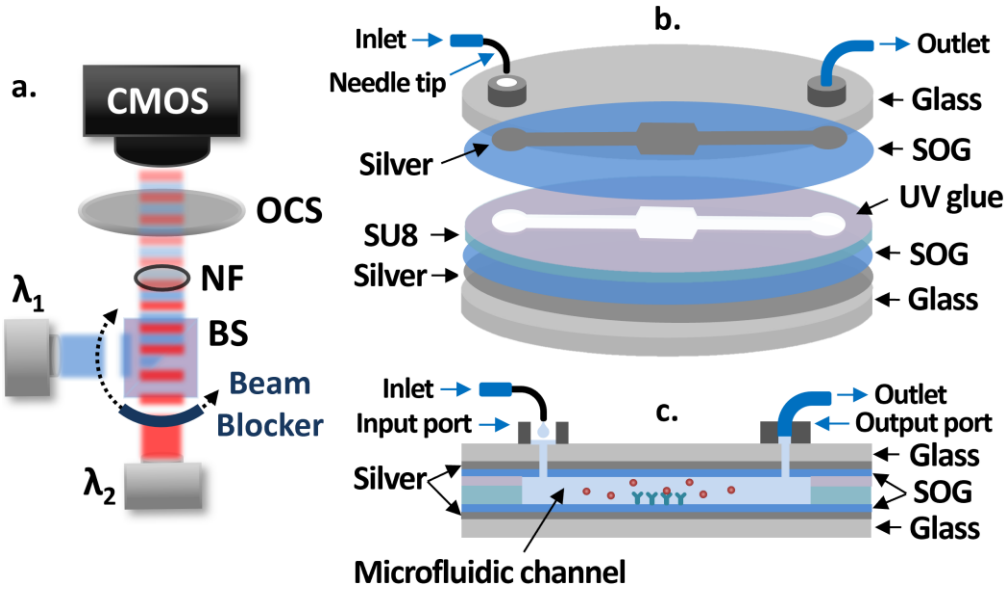

Figure 4.1. (a) Schematic diagram of the OCB showing two laser beams at two different wavelengths (λ_1 (blue) and λ_2 (red)) alternatively propagating through the OCS with an interval of one second and reaching the CMOS camera. (b) Structure of the OCS showing each layer and connected input and output ports. (c) Cross-sectional view of the OCS showing the target biomolecule in a sample fluid being introduced into the microfluidic channel and attached to the receptor molecules on the SOG surface.

4.2. Simulation Results

As illustrated in Figure 4.1(c), the target biomolecules in the sample fluid attach to the receptor molecules which, in turn, causes output intensity changes of two laser diodes. To achieve the largest differential value change, we searched for the optimal cavity width at which the efficiencies of two different wavelengths (out of available low-cost laser diodes in the market) change the most in the opposite directions for the sensing layer thickness increase. Since many different possible solutions exist, we narrowed our search to using a silver thickness of 20 nm with the microfluidic channel height ranging between 5 µm and 10 µm. We chose this channel height range to limit the required fluid

volume to fill the channel without significant fluid flow resistivity. Since the fluid flow resistivity is inversely proportional to the third power of the height, if the height is too small, then the flow rate is slower, and a stronger vacuum pump is necessary to handle the fluids. Considering the typical size of proteins is less than 20 nm, we focused on the simulation for the sensing layer thickness up to 20 nm. From the simulation results, we found the differential value change depends on the SOG thickness. This means the local refractive index change due to the sensing layer change is more influential to the resonant characteristic at certain locations inside the cavity, which must be related to the electromagnetic field distribution in the cavity. Based on the spin curve of the SOG, we considered the SOG thickness in the range of 150 nm to 450 nm.

The simulation results for the optimized optical cavity structure are shown in Figure 4.2. For the wavelengths of 830 nm (λ_1) and 904 nm (λ_2), the optimized optical cavity design has a cavity width (silver-to-silver distance) of 8 μm and a SOG thickness of 400 nm with a silver thickness of 20 nm. As the sensing layer increases from 0 to 20 nm, the efficiency of 830 nm is decreasing from 0.18 to 0.137 (-0.043), while the efficiency of 904 nm is increasing from 0.063 to 0.077 (+0.014). With this opposite changing trend of two wavelengths, the corresponding differential value changes from 0 to 0.481, showing a significantly larger change compared to the individual wavelengths with a better linearity.

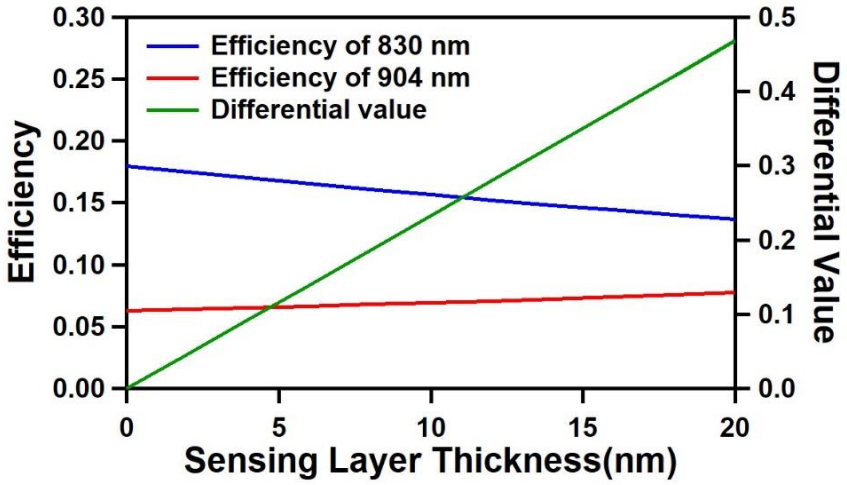

Figure 4.2. Simulation results showing efficiencies of 830 nm (blue) and 904 nm (red) wavelengths and differential values (green) versus the sensing layer thickness in the range between 0 and 20 nm.

4.3. Sample Fabrication and Surface Functionalization Process

A top-view image of the fabricated optical cavity microfluidic channel is shown in Figure 4.3(a). The typical layer thicknesses of fabricated devices are, on average, 22 nm (silver), 410 nm (SOG), 6.4 µm (SU8), and 1.08 µm (UV glue). The microfluidic channel has a total length of 5 cm, a height of 7.5 µm (distance between SOG surfaces), and a width of 500 µm, while the width at the sensing area is 1 mm. The sensing area is 2.5 mm^2, and the dotted circular area at the center with a diameter of 160 µm represents the area used for the data processing calculating the average intensities and differential values.

Figure 4.3(b) illustrates the functionalization steps on the SOG surface on the drilled substrate. The oxygen plasma treatment was applied for 5 minutes to create hydroxyl groups on the SOG surface. We used vapor-phase deposition of APTES by placing a substrate in a desiccator with 0.5 ml of 99% APTES in a small container placed at the bottom [184]. The entire desiccator was placed on a hot plate at 90°C for 24 hours

to create terminal amine groups (-NH_2) on the surface. After the overnight incubation, unbound APTES molecules were removed with DI water in an ultrasonic bath for 7 minutes, and the glass substrate was baked at 110°C for 10 minutes. To functionalize the sensing area, 5 mg/mL of sulfo-NHS-biotin mixed in DI water was applied using a micropipette. It was then incubated for 1 hour to covalently immobilize biotin on the surface through amide bonds, while other areas were passivated with 1% BSA. The surface was then ready for the streptavidin detection experiment. BSA was also applied for the plain substrate with the SU8 pattern to passivate the bottom and side walls of the channel to minimize the nonspecific binding of streptavidin and other biomolecules.

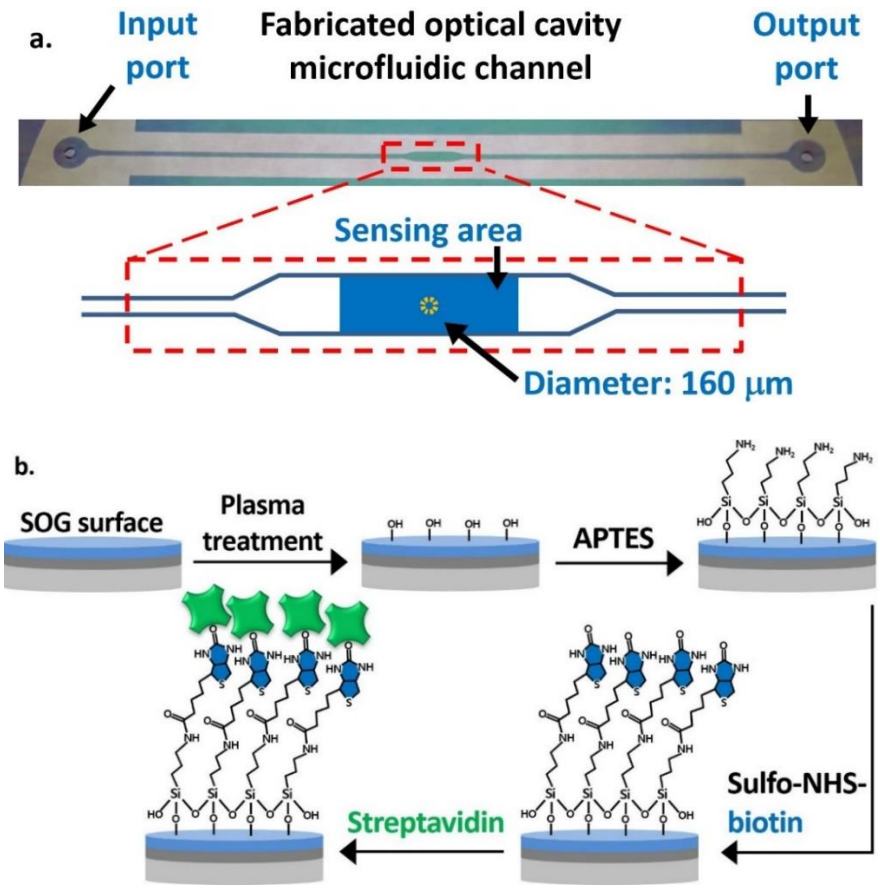

Figure 4.3. (a) Top view of the fabricated optical cavity microfluidic channel indicating the sensing area at the center and the area for the data process. (b) The functionalization procedure of the SOG surface for the immobilization of streptavidin.

4.4. Fine-tuning of the Optical Cavity Width using Polymer Swelling

The optical response of any type of optical resonators is very sensitive to its cavity or resonator size. Due to possible errors during the fabrication process, the cavity widths of the fabricated OCSs show some variations. Even with a larger fabrication tolerance using the differential detection method, it is challenging to successfully fabricate the OCSs with the width within the accuracy of 40 nm, which leads to a low success rate to produce measurable samples [171]. We overcome this problem using the polymer swelling property [185-187]. When our microfluidic channel is filled with DI water, SU8 and UV epoxy slowly swells over time. This swelling causes the optical cavity width to increase. We intentionally fabricated OCSs with a slightly smaller width and fine-tuned it by filling the channel with DI water. As the cavity width gets larger, the intensities of laser diodes at 830 nm and 904 nm are changing along its resonant characteristics. We monitored the intensities during the swelling process and stopped it when the intensity of a laser diode at 830 nm is decreasing, while that of a laser diode at 904 nm is increasing. This indicates the optical cavity has reached a measurable condition, and we can anticipate the optical response upon the immobilization of biomolecules on the functionalized surface as simulated at this condition. The time it takes for this fine-tuning process varies from less than 1 hour to more than 10 hours, as the initial optical cavity widths differ. The swelling rate is rapid at the beginning and then slows over time. With this fine-tuning process, we were able to achieve a very high success rate of producing measurable samples (> 90%).

4.5. Measurement Results

4.5.1. Streptavidin Detection

Streptavidin is a 52.8 kDa protein with a dimension of 5.6 nm × 4.2 nm × 4.2 nm [183]. For a monolayer of streptavidin with a height of 5.6 nm, the simulated differential value change due to this monolayer is 0.1266. For measurements, DI water was introduced first through the microfluidic channel for optical cavity width fine-tuning. When the optical cavity reached the measurable condition, 15 μL of streptavidin was then introduced with a flow rate of about 0.9 μL/min for about 17 minutes. Finally, the channel was rinsed with 15 μL of DI water. Representative trends of four different concentrations of streptavidin in DI water, 300 ng/mL, 1 μg/mL, 3 μg/mL, and 10 μg/mL, are shown in Figure 4.4 along with the negative control. The average differential value for 2 minutes before the introduction of streptavidin is set to be 0 as the baseline. The change in the differential value due to the binding of streptavidin is measured by averaging differential values between 25-27 minutes, which is 8-10 minutes after DI water is introduced for rinsing. For the negative control (black), the sensing area was blocked with BSA everywhere without sulfo-NHS-biotin. As expected, when 1 μg/mL of streptavidin was introduced into the negative control channel, no obvious change in the differential value was found, while there were some fluctuations during the period with streptavidin. This could be due to binding and unbinding activities of streptavidin on the BSA passivated surface. Clearly, some loosely attached streptavidin molecules were removed in the DI water rinse, and the differential values stabilized. The differential value change for the negative control is -0.00213 which is close to the average standard deviation of DI water (σ = 0.00274). For 10 μg/mL concentration (yellow), the

differential value starts changing in 2 minutes and reaches to 0.074 in 5.5 minutes with a slope of 0.0235/min. after the introduction of streptavidin (at t = 0). The change slows down from 5.5 minutes but keeps increasing up to 0.095 with a slope of 0.00163/min. until the DI water is introduced (at t = 17 min.) for the rinse. As soon as the channel is rinsed, the change decreases slightly and reaches 0.085 (at t = 27 min.) on average. The result for the concentration of 3 μg/mL (green) shows that the differential value starts slowly increasing at around 5 minutes and reaches to 0.04 with a slope of 0.0023/min. The change stops for about 3 minutes after the DI water rinse and then increases again to 0.055 with a slower slope of 0.0014/min. This could be due to the binding of residual streptavidin molecules on the surface during the DI water rinse. The changes in differential values for the streptavidin concentrations of 1 μg/mL and 300 ng/mL started at 8 minutes and 12 minutes, respectively, with slower slopes (1 μg/mL: 0.00176/min and 300 ng/mL: 0.00089/min). After the introduction of DI water, they show a similar trend that the differential value decreases for about 3 minutes and increase for the rest of 7 minutes reaching to 0.027 and 0.16, respectively. Those changes after the DI water rinse could be also caused by the unbound molecules.

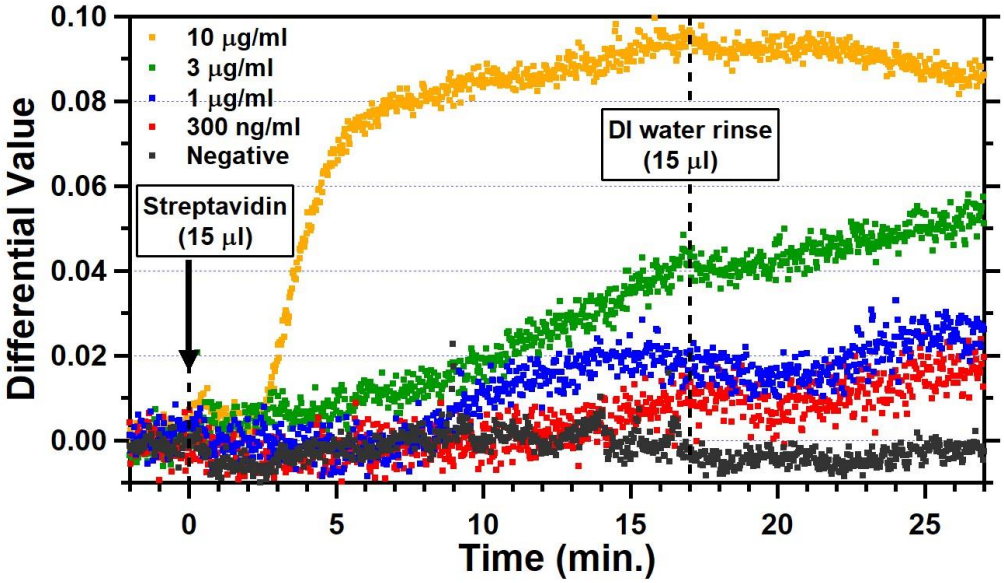

Figure 4.4. Real-time measurements for 30 minutes showing the changing differential values after the introduction of 15 μL of streptavidin for four different concentrations and the negative control (10 μg/mL: yellow, 3 μg/mL: green, 1 μg/mL: blue, 300 ng/mL: red, and negative control: black).

The triplicate test results of four different concentrations are shown in Figure 4.5. The average differential value changes were 0.074 ± 0.018 (10 μg/mL), 0.039 ± 0.0091 (3 μg/mL), 0.024 ± 0.003 (1 μg/mL), and 0.013 ± 0.001 (300 ng/mL). The LOD of our OCB biosensor was determined by the average sensor response crossing the 3σ line (0.00821), which was 71.3 ng/mL (1.35 nM). The differential value of 10 μg/mL did not reach the anticipated value for a monolayer of streptavidin (0.1266). There are a few possible hypotheses to explain this: (1) streptavidin molecules on the sensing area are oriented to where the smaller side of the molecule is in the beam propagation direction, (2) the actual refractive index change due to the immobilization of the streptavidin is less than the monolayer with the refractive index of 1.45 used for simulation, or (3) the functionalization and passivation processes were not sufficient to allow streptavidin molecules to form a densely-packed monolayer on the sensing area without losing them

through non-specific bindings on other passivated surfaces. Out of these, the third is most likely. Even if the layer created by the immobilized streptavidin molecules is thinner with a lower refractive index and the differential value for a monolayer of streptavidin is about 0.074 (average differential value change for 10 μg/mL), it is clear we were not able to form a densely packed streptavidin only on the sensing area. Based on the given size of the streptavidin, the total amount of streptavidin to form a monolayer covering the entire sensing area of 2.5 mm^2 is estimated to be 12.4 ng. For the streptavidin concentration of 1 μg/mL, the total amount of streptavidin in 15 μL of sample fluid is 15 ng. This indicates that, if all available streptavidin molecules are attached densely only on the sensing area, then there are more molecules than necessary to form a monolayer. If a monolayer is formed and the assumption of the differential value change (0.074) for a monolayer of streptavidin is valid, then the differential value is supposed to reach to that level with 1 μg/mL. However, since the differential value change for 1 μg/mL of concentration is only 0.024, the result clearly shows no monolayer was formed. This suggests the sensing area is not well functionalized with active biotin, and/or we lost many streptavidin molecules in other areas. If we improve the functionalization and passivation processes to block other areas from target biomolecules for being attached so that all available target molecules are attached densely only on the sensing area, the result can be significantly improved.

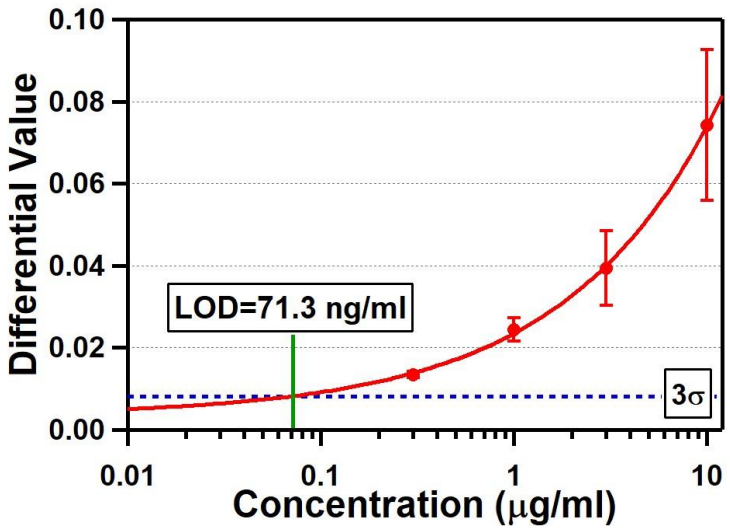

Figure 4.5. Differential values measured in triplicate versus four concentrations of streptavidin in a log scale.

4.5.2. C-reactive Protein Detection

CRP is a 115 kDa serum protein with a hydrated volume of 197.3 mm^3 and one of the most frequently used cardiac biomarkers with high specificity to diagnose and monitor cardiovascular diseases (CVDs), which are the leading cause of death worldwide [188]. The American Heart Association (AHA) and the Center for Diseases Control and Prevention (CDC) defined the risks for CVDs to be low for a concentration of CRP in humans below 1 μg/mL, moderate for a CRP concentration between 1-3 μg/mL, and high for a CRP concentration over 3 μg/mL [189]. The level of human CRP is also increased 1,000-fold within 24-48 hours in response to infection, inflammation, and tissue damage [190]. Figure 4.6 shows the measurement results for three different concentrations of CRP (10 μg/mL, 1 μg/mL, and 100 ng/mL) using the OCB. For CRP detection, we followed the same fabrication and functionalization processes used for the streptavidin detection. To functionalize the sensing area with the CRP antibody, we first introduced 30 μL of streptavidin with a concentration of 100 μg/mL to the microfluidic channel and

incubated at least 30 minutes so that streptavidin molecules are immobilized on the biotin on the sensing area. After rinsing the channel with DI water to remove unbound streptavidin molecules, 30 μL of biotin conjugated CRP antibody with a concentration of 100 μg/mL was introduced and incubated at least 30 minutes so that biotin part of it was attached to the streptavidin-coated surface, while the CRP antibody covered the surface. The microfluidic channel was rinsed with DI water to remove unbound CRP antibody molecules and filled with it for fine-tuning of the optical cavity through polymer swelling. When the optical cavity was ready for the experiments, we introduced 15 μL of CRP protein spiked in tris-HCl buffer with a flow rate of about 0.9 μL/min for about 17 minutes. Finally, the microfluidic channel was rinsed with DI water, and the average differential value changes were determined. The measured average differential value changes were 0.141 (10 μg/mL), 0.061 (1 μg/mL), and 0.018 (100 ng/mL). Based on the measured average standard deviation at the baseline data with DI water ($\sigma = 0.00284$), the LOD for CRP detection is determined to be 43.3 ng/mL (377 pM).

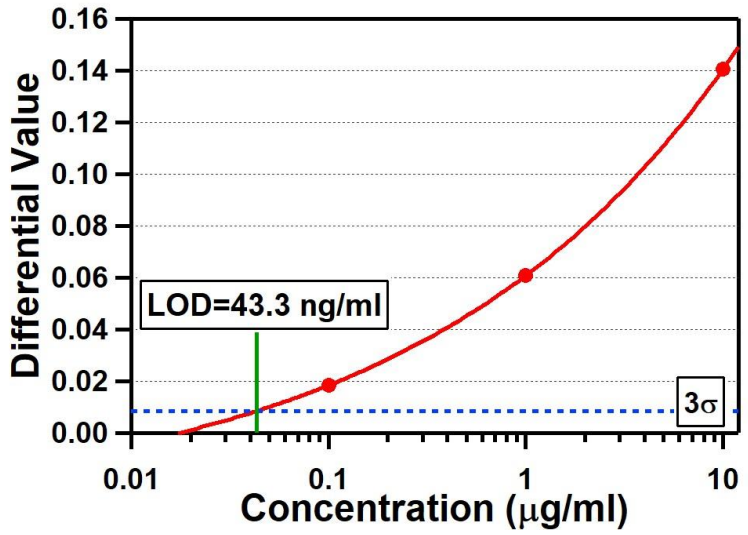

Figure 4.6. Differential values versus three concentrations of CRP in a log scale.

4.5.3. Discussion of the LOD

The LOD of our OCB for the streptavidin detection (1.35 nM) can be improved further. First, the sensing area (2.5 mm^2) where streptavidin was allowed to be attached was larger than the area that was used for data processing (0.02 mm^2: the area of a 160 μm diameter circle). If we properly functionalize only this area with sulfo-NHS-biotin so that streptavidin molecules can be attached within the area of 0.02 mm^2, then the LOD of the OCB becomes 10.9 pM assuming streptavidin molecules are attached on the sensing area uniformly. Second, as we discussed earlier, the current functionalization and passivation processes need to be improved further to allow more streptavidin molecules to be attached only at the sensing area. If we consider the sensing area of 0.02 mm^2 and lose only about 20 % of target molecules (equivalently, 15 μL of 1 μg/mL streptavidin forms a monolayer on 2.5 mm^2), then we can estimate the LOD can be improved further by an order of magnitude to 1.09 pM. Finally, the LOD will be improved proportionally by the amount of sample fluid. This is simply because, to be able to detect the differential value changes, we need a certain number of target biomolecules on the sensing area regardless of the total volume of sample fluid. For a lower concentration sample, the sample fluid with a larger volume will contain enough biomolecules to cause the differential value change to greater than 3σ. For example, the LOD can go down to 109 fM, which is 10 times smaller concentration than 1.09 pM from the previous LOD estimation, with a sample volume of 150 μL (i.e., 10 times of 15 μL volume used previous analysis). The same analysis can be applied to the LOD for the CRP detection. For the smaller sensing area of 0.02 mm^2, the LOD for CRP can be improved to 3.016 pM from 377 pM with the sensing area of 2.5 mm^2. With improved functionalization and

passivation processes assuming only 20% of target molecules will be lost, the LOD for CRP will be improved further to 302 fM. Finally, with the sample volume of 150 μL, the LOD can reach to 30.2 fM.

4.5.4. Discussion on the Optimal Optical Cavity Design

The design presented in the work was optimized for a silver thickness of 20 nm. It is possible to design an optical cavity structure with a better LOD with a thicker silver layer. A thicker silver layer will increase the reflectance of the partially reflective mirrors which will, in turn, sharpen the resonant response of the optical cavity. With a sharp resonant response, the intensity changes of two wavelengths will be steeper for the sensing layer thickness increase than that with the current design. This will enhance the differential value change and, therefore, improve the LOD. However, a thicker silver layer will also increase the absorption of light, increasing the optical loss of two laser diodes. The optical loss at each partially reflective mirror will reduce the sharpness of the resonant response. Therefore, an improved optical cavity design with a thicker silver is possible, but it has to be experimentally optimized due to these conflicting phenomena.

CHAPTER FIVE

Portable & Three-laser System

This chapter published as: D. Rho, C. Breaux, and S. Kim, "Demonstration of a Low-Cost and Portable Optical Cavity-Based Sensor through Refractive Index Measurements," *Sensors (Basel),* vol. 19, no. 9, May 12 2019, doi: 10.3390/s19092193 [167],

D. Rho and S. Kim, "Low-cost optical cavity based sensor with a large dynamic range," *Optics Express,* vol. 25, no. 10, pp. 11244-11253, May 15 2017, doi: 10.1364/OE.25.011244 [171].

The presented measurement results were done on an optical table. The optical table not only offers a rigid surface to mount and align optical components readily but also helps to minimize the noise by isolating the optical system from ambient vibrations. Portability with a stand-alone system is required to be employed as a POC biosensor. A prototype of the portable OCB was built using a commercial 3D-printer, and its capability of detecting small refractive index changes was demonstrated in this chapter [167].

Also, the OCB with three-laser system was proposed for the demonstration of a chained differential detection method to improve a dynamic range and fabrication tolerance. The design and measurement results of three-laser system were presented, and repeatability tests using two-laser system and three-laser system were compared and analyzed in this chapter [171].

5.1. Demonstration of the Portability

5.1.1. Simulation Results

The simulation results for the optical cavity structure are shown in Figure 5.1(a) for the refractive index range between 1.328-1.338 [167]. The design parameters using 830 nm and 880 nm wavelengths are a cavity width of 10.14 µm, a silver thickness of 18 nm, and a SOG thickness of 400 nm. The efficiency of 880 nm decreases, while the efficiency of 830 nm increases over the refractive index range of our interest that includes 1.333. Figure 5.1(b) shows the simulation results within the refractive index range from 1.3329 to 1.3338. In this range, the efficiency of 830 nm has a slope of 143.91/RIU with a R^2 of 0.996, and the efficiency of 880 nm has a slope of -66.19/RIU with a R^2 of 0.9942. As the efficiencies change in opposite directions, the differential value has a higher slope of 439.31/RIU and shows better linearity with a R^2 of 0.999 compared to the individual wavelength efficiency.

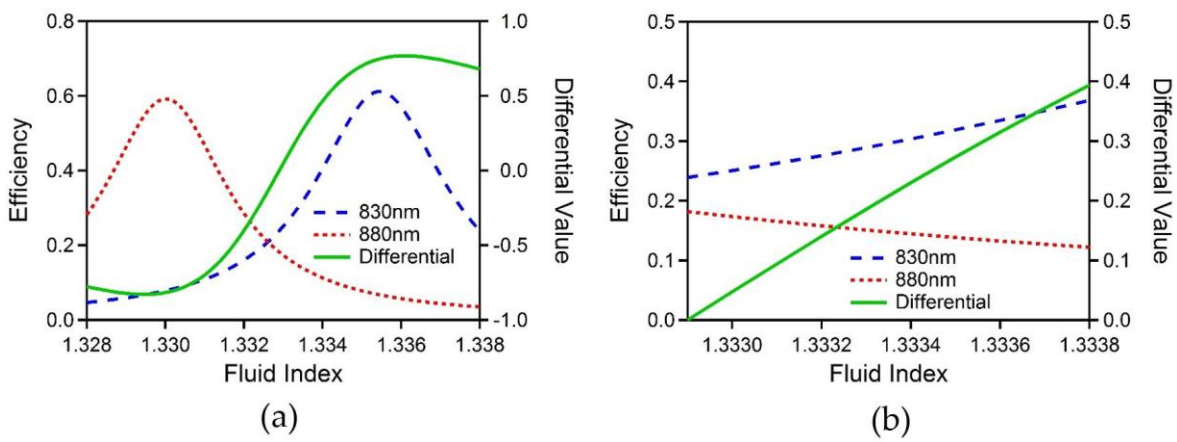

Figure 5.1. (a) Simulation results showing efficiencies of 830 nm (blue dashed line) and 880 nm (red dotted line) and differential value (green solid line) versus the refractive index inside the optical cavity in the range between 1.328 and 1.338. (b) Simulation results as shown in Figure 2a with the range of refractive index between 1.3329 and 1.3338.

5.1.2. Portable System

Figure 5.2(a) shows a fabricated optical cavity sample including 6 fluidic channels. The optical cavity sample with 3D printed input and output adapters attached is placed on the sample holder of the portable system shown in Figure 5.2(b). A prototype of the portable system for the optical cavity-based sensor was fabricated using a 3D printer (Creator Pro, FLASHFORGEUSA), which enables rapid materialization of the design and allows the system to be upgraded efficiently. All structural components, excluding hardware and certain optical mounts, were fabricated via fused deposition modeling with polylactic acid (PLA). The system was designed in tiers that were assembled after printing the parts. The bottom level contains the electrical components including a laser diode driver, an Arduino for servo motor control, and a multi-channeled output power supply with its switch. The middle level houses the optical components including 830 nm and 880 nm laser diodes with collimators, kinematic mounts, two servo motors, a 50:50 beam splitter, and a right-angled mirror as shown in Figure 5.2(c). In order to measure the intensities of laser diodes and obtain differential values in real-time using one camera, two servo motors are used to alternately block the light from one laser diode at a time with one second intervals. The servo horns are affixed with gears, and the servo motors rotate to move 3D-printed gear rack blocking plates back and forth as shown in Figure 5.2(d). The top level consists of the sample holder, a plate fixed to the sample holder below, and the CMOS camera fixed to a camera mount. For precise and simple optical alignment, the parts mounted in the top level are designed to be more adjustable with thumbscrews. The overall dimensions for the portable system are approximately 6.5 inches wide by 8.5 inches in length by 11 inches in height, weighing

no more than 10 lbs. All parts in the system can be bought off-the-shelf, and the total cost to build is about $1,500.

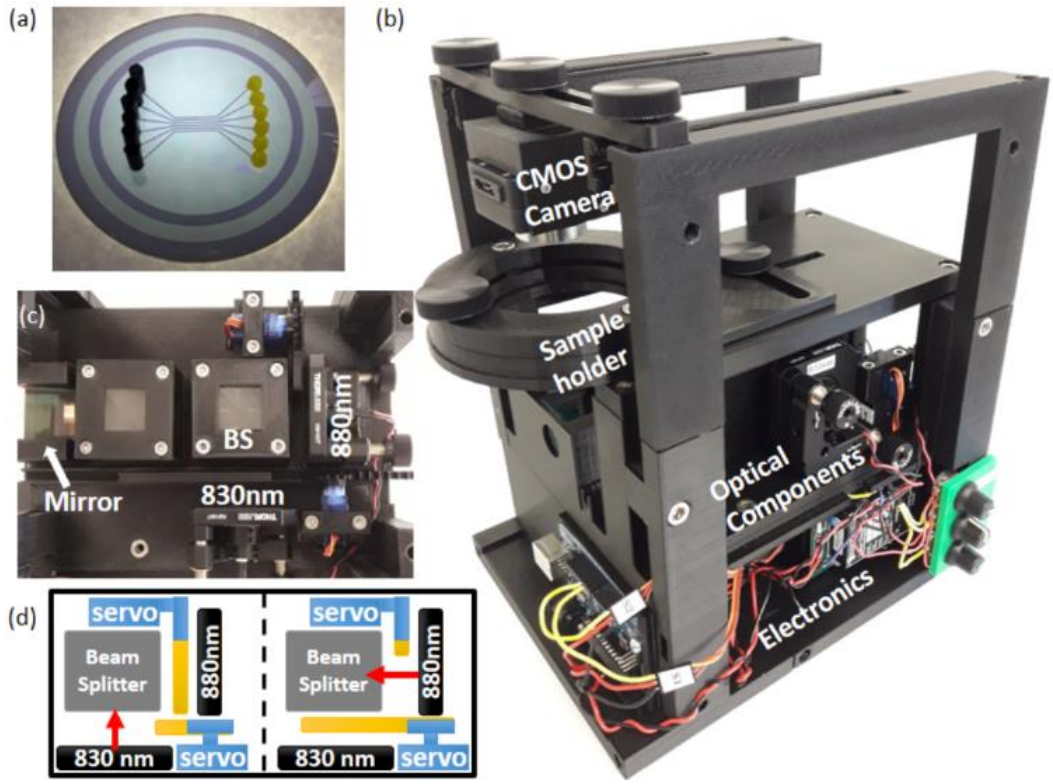

Figure 5.2. (a) Fabricated optical cavity sample including 6 fluidic channels. 3D printed adapters are attached to inlets and outlets. (b) Prototype of portable optical cavity-based sensor. (c) Optical components mounted on the middle level plate of the portable system. (d) Schematic of servo motors (blue parts) with blocking plates (yellow parts) to block laser diodes alternately.

5.1.3. Refractive Index Measurement Results

The refractive index measurements using the portable system were performed on a table with wheels to demonstrate the sensitivity of the portable system in typical user settings. The fluidic channel of an optical cavity sample was aligned with the center of the collimated laser beams, and the CMOS camera continuously captured images of beam profiles to measure laser intensities in real-time. A 40 × 40 pixel array of the CMOS images was selected near the middle of the channel to calculate the average pixel

intensity. Based on the size of a pixel, the chosen pixel area is approximately equal to the area of 140 μm × 140 μm.

DI water (n = 1.3329) and DMSO (n = 1.4787) are mixed with different ratios to produce 5 refractive index fluids, 1.3329, 1.3332, 1.3334, 1.3336, and 1.3338, which were confirmed with a digital refractometer (PA202, MISCO). The channel was initially filled with DI water to acquire baseline intensities for 20 seconds. DI water in the channel was then replaced with a refractive index fluid of 1.3332. After another 20 seconds, DI water was again introduced to the channel to recover the baseline. The same procedure was then repeated for the rest of three refractive index fluids to calculate the changes in both intensities from the baseline signal. During the measurements, the portable system is covered with an enclosure to avoid ambient light reaching the CMOS camera. Throughout the measurement, the volume of each fluid introduced was 2 μL, and the fluids were controlled by a mini vacuum pump connected to an output port via tygon tubing. The entire time spent measuring 5 refractive index fluids was about 8 minutes.

Since the refractive index measurements were performed on a relatively unstable table, the measured intensities were noisier than those with an optical table. One of the major noise sources may be the vibrations introduced to the portable system from the internal parts and surroundings. Such noise due to the vibration could be common among the measured channel and other areas around it including adjacent, unused empty channels. To effectively cancel out common variations, we employed a referencing technique [173]. The referencing technique is designed to remove common variations from the measured data using the reference data collected from the adjacent empty channel using the equation below.

$$I_P = I_D - I_R \frac{I_{D_0}}{I_{R_0}} + I_{D_0} \tag{5.1}$$

I_P is the processed average pixel intensity, I_D and I_R are the average intensity measured at the tested channel and the average intensity measured at the empty channel (as a reference), respectively. I_{D_0} and I_{R_0} are the initial values of I_D and I_R, respectively. The collimated beam and CMOS imaging area are large enough to collect the data from multiple channels including the test channel and adjacent one. To lower the noise level further, a low-pass filter was applied digitally to the processed intensities.

Figure 5.3 shows the measurement results. The average pixel intensities of two laser diodes and the calculated differential values are shown in the figure with their respective linear fits as a function of the refractive index fluids. The error bars indicate +/- standard deviation of each data point, but they are too small to be visible.

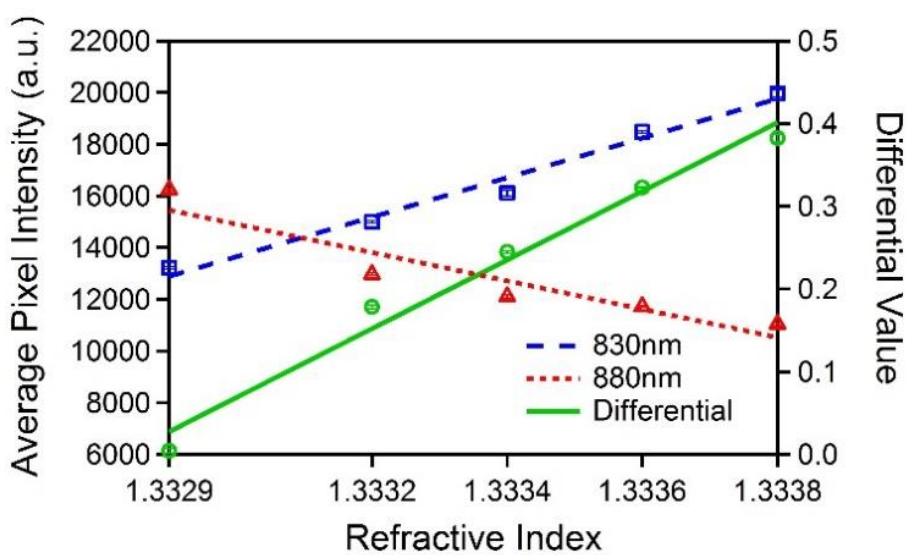

Figure 5.3. Measurement results showing the average pixel intensities for 830 nm (blue dashed line) and 880 nm (red dotted line) and differential value (green solid line) versus the refractive indices in the same range (1.3329-1.3338) as shown in Figure 5.1(b).

As the refractive index increases from 1.3329 to 1.3338, the average intensity of 830 nm increases from 13,223 to 19,972, and the average intensity of 880 nm decreases from 16,253 to 11,051. The corresponding differential value is increased from 0 to 0.383 with a slope of 415.1/RIU. The measured differential value slope is close to the slope of 439.31/RIU obtained in the simulation.

Based on the measurement results, the LOD is estimated using the slope and standard deviation. The standard deviation is obtained by taking an average of 5 measurements at each refractive index fluid. The LOD of the differential value was 1.73×10^{-5} RIU, which is comparable with other methods reported that are not low-cost nor portable [191-197].

5.2. Demonstration of Three-laser System

5.2.1. Repeatability Test of Two-laser System

A repeatability test was performed for the design used in Section 3.1 [171]. Three more samples were fabricated with the same process. Figure 5.4 shows the measurement results of these three new samples compared to the sample we measured for Figure 3.6 (first sample). The slopes of differential values for first, second, third, and fourth samples were similar to one another, which are 32.943/RIU, 28.11/RIU, 29.449/RIU, and 32.002/RIU, respectively. In addition, they show good linearity in the dynamic range of 0.025 with the coefficients of determination (R^2) of 0.9907, 0.9977, 0.9831, and 0.9946, respectively. However, despite the similarities, the differential values have shifted slightly, and each sample has a dynamic range in a different refractive index region. For example, the first sample has the dynamic range in between the refractive

index of 1.32–1.345. However, the second sample, which is shifted the most from the first sample, has the dynamic range in between 1.3–1.325. The horizontal shift of the differential value is mainly due to cavity width variations among samples. Based on the simulation, we found that the second sample has a cavity width larger than the first sample by 33 nm while the fourth sample's cavity width is larger by 8 nm. Further simulations show that a 50 nm deviation (about 2.3% from the designed width of 2.2 μm) in the cavity width shifts the dynamic range by 0.03 in the refractive index. This result also implies our design for the two-laser system has a very tight fabrication tolerance to maintain the dynamic range around 1.33. This is problematic because the optical cavity structure is mainly proposed for biosensing applications. In other words, if these four samples are used for biosensing applications, the second and third samples will not show the response change upon the adsorption of target biomarkers because their dynamic ranges do not include 1.33.

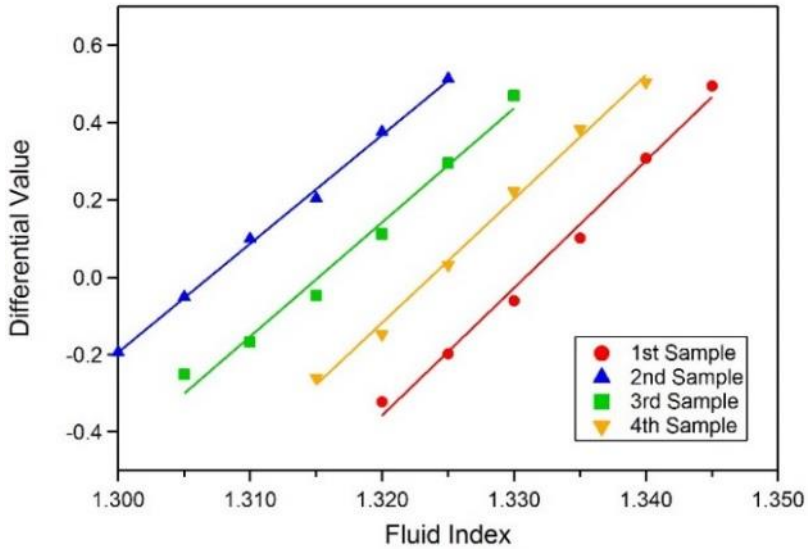

Figure 5.4. The repeatability test results. The 1st sample data is from Figure 3.6.

The cavity width of the optical cavity sensor is mainly determined by the SU8 thicknesses on both substrates and the manual bonding process. It is not an easy task to fabricate consistent samples with this tight fabrication tolerance, and it will eventually increase the cost of sample fabrications. One way to improve this fabrication tolerance is to increase the dynamic range. With a large dynamic range, it is possible for any sample to have a dynamic range including 1.33, even with some fabrication errors. To increase the dynamic range and improve the fabrication tolerance, we proposed a three-laser system with a chained differential detection method.

5.2.2. Schematic

A schematic of the three-laser system is shown in Figure 5.5. Again, we optimized the optical cavity structure for the available low-cost off-the-shelf laser diodes. The final wavelengths used for the optimized structure are 780 nm, 808 nm, and 904 nm wavelengths. Two beam splitters combine the collimated light waves from three different laser diodes. The light waves propagate through the optical cavity along the same path, and the CMOS camera captures each laser beam profile to measure the average intensities of the three laser diodes sequentially.

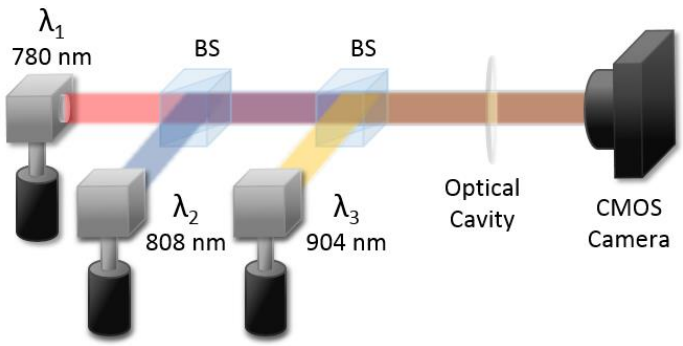

Figure 5.5. Schematic diagram of three-laser system using laser diodes at 780 nm, 808 nm, and 904 nm wavelengths.

5.2.3. Simulation Results

The optimized optical cavity structure for the three-laser system has a cavity width of 3.5 μm and a silver thickness of 8 nm. The simulation results are shown in Figure 5.6. Figure 5.6(a) shows the efficiency changes for the three wavelengths between the refractive index of 1.3 and 1.45. The resonant response curves overlap one another to create repeated patterns in which at least two of the three wavelengths are changing their intensities in opposite directions throughout the entire range of the refractive index. We selectively chose those two wavelengths at different index ranges to calculate the differential values. For example, between the refractive index of 1.314 and 1.337, efficiencies of 780 nm and 808 nm are changing the most in the opposite directions while the efficiency of 904 nm does not change much. Therefore, those two wavelengths are used to obtain the differential values in that range. Similarly, the differential values are calculated using 780 nm and 904 nm wavelengths from 1.337 to 1.351 index. In the range of 1.351–1.371, we used 808 nm and 904 nm wavelengths to calculate the differential values. Figure 5.6(b) shows the calculated differential values in these different ranges with different sets of wavelengths that are used. This mechanism is named the chained differential detection method. By utilizing it, we can obtain seven linear regions of differential values between the refractive index of 1.314 and 1.45. Figure 5.6(c) shows the concatenated differential values, which have a slope of 35.724/RIU with a coefficient of determination of 0.998. The dynamic range obtained by the chaining action is 1.314–1.45 ($\Delta n = 0.136$), which is more than five times greater than the dynamic range of the two-laser system ($\Delta n = 0.025$).

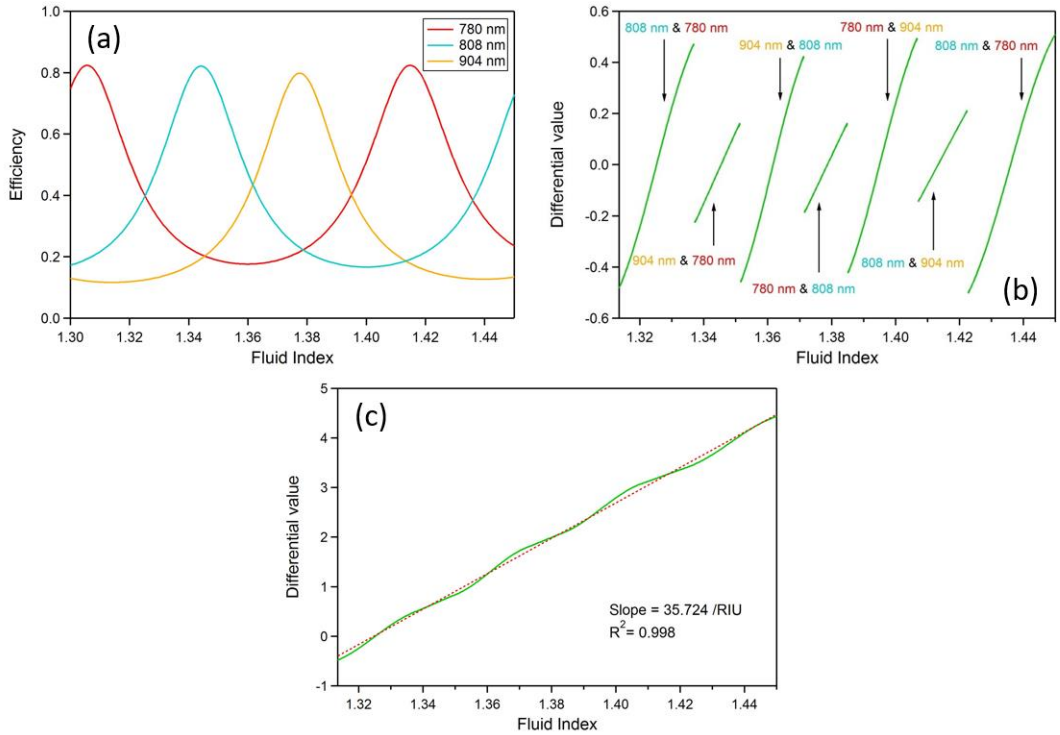

Figure 5.6. Simulation results for the optimized optical cavity structure for the three-laser system. (a) Efficiencies of 780 nm (red), 808 nm (sky blue), and 904 nm (yellow) as a function of the refractive index from 1.3 to 1.45. (b) Calculated differential values with different sets of two wavelengths in seven different sections. (c) Concatenated differential values.

5.2.4. Measurement Results

To experimentally demonstrate the optical cavity sensor with a chained differential detection method, we fabricated the optical cavity structure with the same process used for the fabrication of samples for the two-laser system except for thicker SU8 layers on both substrates (slower spin speed) in order to obtain the cavity width of 3.5 μm. The test setup for the three-laser system is also the same, except for the use of three laser diodes and two beam splitters, as shown in Figure 5.7. The results of the refractive index measurements using the three-laser system are shown in Figure 5.8. Figure 5.8(a) shows the measured intensities of the 780 nm, 808 nm, and 904 nm wavelengths in the refractive index range of 1.3–1.395. The results are very similar to the

simulation results in that the measured intensities of the three wavelengths overlap each other and form a repeating pattern. The differential values are obtained by using different combinations of two wavelengths changing the most in opposite directions. Initially, for the refractive index range of 1.3–1.33, 780 nm and 808 nm are used to calculate the differential value. Then, 780 nm and 904 nm are used for the range of 1.33–1.34 while 808 nm and 904 nm are used for 1.34–1.365. For the index range of 1.365–1.375, 808 nm and 780 nm are used. Lastly, 904 nm and 780 nm are used for the range of 1.375–1.395. The combined differential values in the different refractive index ranges with different sets of wavelengths are shown in Figure 5.8(b). Figure 5.8(c) shows the concatenated differential values that have a slope of 40.548/RIU and a coefficient of determination of 0.994 within the dynamic range of 1.3–1.395 ($\Delta n = 0.095$). This experimentally measured dynamic range is more than three times greater than that of the two-laser system. Note that this is the measurable dynamic range with the refractive index fluids we used, and the actual dynamic range could be more than five times greater than that of the two-laser system based on the simulations.

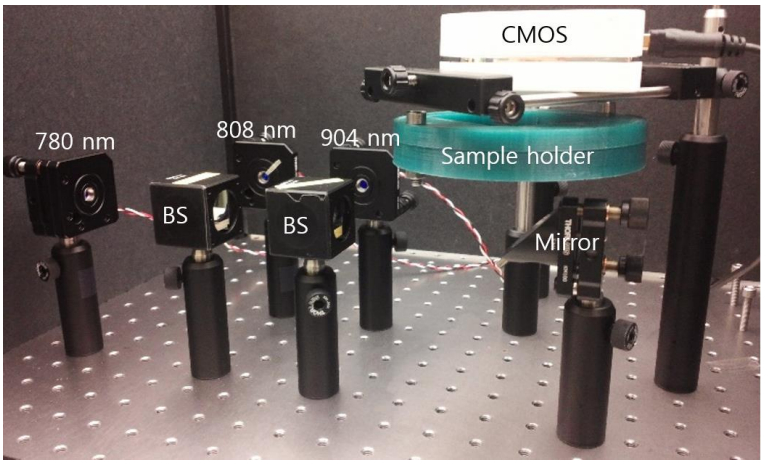

Figure 5.7. The measurement setup for the three-laser system.

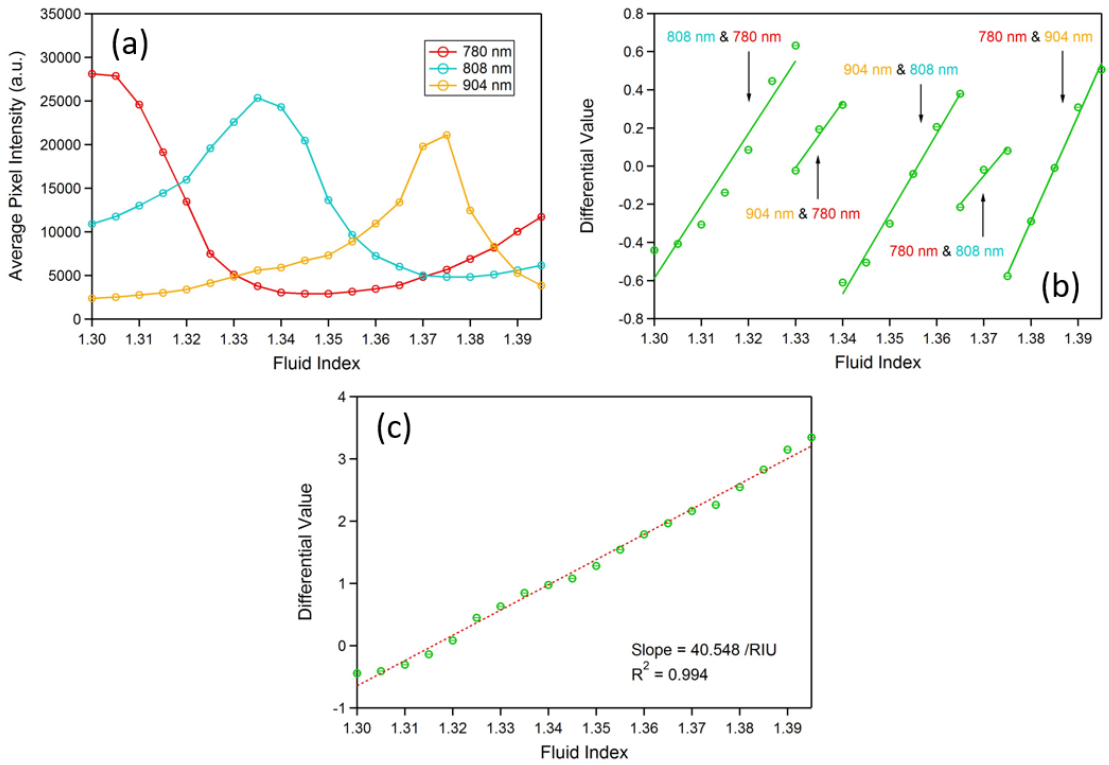

Figure 5.8. Measurement results. (a) Intensities of 780 nm (red), 808 nm (sky blue), and 904 nm (yellow) as a function of the refractive index from 1.3 to 1.395. (b) Calculated differential values in five different sections with selected wavelengths. (c) Concatenated differential values.

5.2.5. Repeatability Test

A repeatability test is also performed using the three-laser system. We fabricated two more samples with the same process used for the sample for Figure 5.8 and conducted refractive index measurements. Figure 5.9 shows the concatenated differential values of all three samples as a function of the refractive index between 1.3 and 1.385. All of them are changing linearly with the slope of 39.407/RIU (first sample used for Figure 8), 40.488/RIU (second sample), and 39.726/RIU (third sample). The coefficients of determination are 0.994 (first sample), 0.995 (second sample), and 0.99 (third sample). As expected from the two-laser system repeatability test, the cavity width variations among three samples cause the resonant response curve shifts. However,

because of its large dynamic range, the differential values still have linear changes near the refractive index of 1.33. This means the optical cavity sensor with a chained differential detection method using the three-laser system has not only a larger dynamic range but also a larger fabrication tolerance. Because of the large dynamic range, this optical cavity sensor can measure a wide range of refractive index of fluids. And because of its large fabrication tolerance, the optical cavity sensor with some fabrication errors can still be used for biosensing.

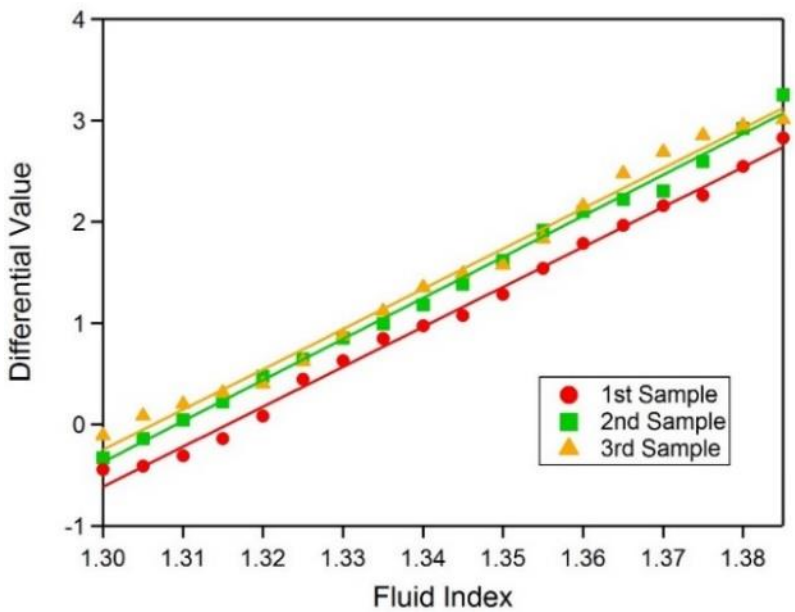

Figure 5.9. The concatenated differential values of three samples using the three-laser system.

CHAPTER SIX

Conclusions and Future Work

6.1. Conclusions

As proof-of-concepts of the OCB, the refractive index measurements and the detection of biotinylated BSA were performed. For the refractive index measurements, the optical cavity structure is designed to have a cavity width of 2.2 μm and a silver thickness of 8 nm. By employing the differential detection method, the responsivity and dynamic range are improved compared to the intensity change of individual wavelength. The measurement results match very well with the simulation results.

The detection of biotinylated BSA was successfully demonstrated with an optical cavity structure having a cavity width of 2.5 μm, a silver thickness of 14 nm, and a SOG thickness of 100 nm. As the sensing layer thickness increases inside the optical cavity, the intensities of 780 nm and 850 nm are linearly increased and decreased, respectively. Biotinylated BSA with a concentration of 3 μM was introduced and immobilized on the streptavidin-coated surface. The real-time detection results match very well with the simulation results. The total change of 0.179 in the differential value corresponds to a sensing layer thickness of 14.1 nm, which is reasonable considering the dimension of BSA. The potential of the multiplexability was also discussed by analyzing each pixel in CMOS images.

After modifying the optical cavity structure and improve the surface functionalization process, streptavidin and CRP biomarker detections were performed to

experimentally demonstrate the biosensing capability of the OCB and LOD. For a silver thickness of 20 nm, the optimized optical cavity structure has a cavity height of 8 μm and a SOG thickness of 400 nm for 830 nm and 904 nm wavelengths. The fabricated devices have dimensions on average including 22 nm of silver, 410 nm of SOG, 6.4 μm of SU8, and 1.08 μm of UV glue. The polymer swelling property was utilized to fine-tune the optical cavity width. For the streptavidin detection results in triplicate, the LOD of the OCB was determined to be 1.35 nM with four different concentrations. Human CRP was selected to demonstrate our OCB to detect an actual biomarker for the first time. With biotin-conjugated CRP antibody as the receptor molecules, the OCB successfully detected CRP with a LOD of 377 pM. Using a small sample volume of 15 μL, all measurements were done in a short time less than 30 minutes once the optical cavity reached to the measurable condition after the fine-tuning process. The LOD of our OCB can be improved further into the femto-molar range for both streptavidin and CRP by reducing the sensing area, improving the functionalization and passivation processes, and increasing the sample volume. The LOD of the OCB could be possibly improved with a thicker silver layer, but it must be experimentally optimized.

To promote the realization of the OCB as a POC device further, the portability in a stand-alone system was validated. A prototype of a portable optical cavity sensor was built using a commercial 3D printer and incorporating off-the-shelf optical components. The LOD for refractive index detection was calculated to be 1.73×10^{-5} RIU providing the potential for high sensitivity using the portable optical cavity-based sensor.

Also, three-laser system was proposed to improve the fabrication tolerance, and the preliminary tests were conducted through the refractive index measurements. The

measurement results matched very well with the simulation results again for the three-laser system. The concatenated differential values with the three-laser system had the responsivity of 40.548/RIU with a dynamic range of 0.095, which is more than three times greater than that of the two-laser system. The repeatability test using the three-laser system shows that the increased dynamic range effectively improves the fabrication tolerance.

6.2. Future Work

The biosensing capability of the OCB has been successfully demonstrated, but only one cardiac biomarker has been detected. More biosensing tests need to be performed using the OCB for various kinds of biomarkers indicating cancers, cardiovascular diseases, or infectious diseases to evaluate a range of application. Also, based on the validated portability and feasibility of three-laser system, the detection of biomarkers can be conducted in a stand-alone system including low-cost laser diodes at three different wavelengths.

To improve the portable system further, the OCB can be incorporated with an automated fluidic delivery system using microfluidics. So far, input and output ports have been manually attached on fabricated optical cavity samples using double sided tapes, and test fluids have been delivered to the microfluidic channel using a bulky syringe pump and a vacuum pump with tygon tubing. By employing a microfluidic platform in a portable OCB, we can simplify the test procedure without the need of manual preparation steps for the fluid delivery and reduce the total test time with more precise fluidic control.

The CRP and streptavidin detections have been performed by preparing and diluting them in tris-HCl buffer and DI water, respectively. To be a promising POC

device without the need of purification steps for the sample preparation, the capability of detecting target biomarkers in crude clinical samples such as blood and plasma should be demonstrated. As discussed in the section 4.5.3, the passivation and functionalization procedure need to be further improved to enhance the sensitivity and selectivity of the OCB for the use of crude samples.

A potential for the multiplexability of the OCB has been evaluated and discussed in the section 3.2.5, which is an integral characteristic of a POC biosensor. To validate the simultaneous detection of multiple biomarkers, a sample fluid needs to be spiked with them, and corresponding specific receptors need to be properly immobilized on different locations within the sensing area using a micro-plotter. Each pixel area in the captured images can be analyzed to determine the presence and concentration of the spiked biomarkers.

BIBLIOGRAPHY

[1] L. Qlark Jr, "Monitor and control of blood and tissue oxygen tensions," *ASAIO Journal,* vol. 2, no. 1, pp. 41-48, 1956.

[2] MarketsAndMarkets, "Biosensors Market by Type (Sensor patch and embedded device), Product (Wearable and nonwearable), Technology (Electrochemical and optical), Application (POC, Home Diagnostics, Research Lab, Food & Beverages), and Geography - Global Forecast to 2024," 2019. [Online]. Available: https://www.marketsandmarkets.com/Market-Reports/biosensors-market-798.html?gclid=Cj0KCQjwtZH7BRDzARIsAGjbK2aQ_v8cUM9AoNHPEXhqI-N-WJrEJ0xpNp2fi_NcchGjTOcE213nyloaAv9aEALw_wcB

[3] P. Mehrotra, "Biosensors and their applications - A review," *J Oral Biol Craniofac Res,* vol. 6, no. 2, pp. 153-9, May-Aug 2016, doi: 10.1016/j.jobcr.2015.12.002.

[4] V. Garzon, D. G. Pinacho, R. H. Bustos, G. Garzon, and S. Bustamante, "Optical Biosensors for Therapeutic Drug Monitoring," *Biosensors (Basel),* vol. 9, no. 4, Nov 11 2019, doi: 10.3390/bios9040132.

[5] N. Cheng *et al.*, "Recent advances in biosensors for detecting cancer-derived exosomes," *Trends in biotechnology,* vol. 37, no. 11, pp. 1236-1254, 2019.

[6] R. Shandilya, A. Bhargava, N. Bunkar, R. Tiwari, I. Y. Goryacheva, and P. K. Mishra, "Nanobiosensors: Point-of-care approaches for cancer diagnostics," *Biosensors and Bioelectronics,* vol. 130, pp. 147-165, 2019.

[7] B. Bohunicky and S. A. Mousa, "Biosensors: the new wave in cancer diagnosis," *Nanotechnol Sci Appl,* vol. 4, pp. 1-10, Dec 30 2010, doi: 10.2147/NSA.S13465.

[8] M. I. o. T. Department of Instrumentation & Control Engineering. Schematic Diagram of a Biosensor Working of Biosensors [Online] Available: https://www.slideshare.net/meenasundar/micro-electro-mechanical-systems-mems-class-materials-lecture-04

[9] A. C. Society. Screening Tests for Prostate Cancer [Online] Available: https://www.cancer.org/cancer/prostate-cancer/detection-diagnosis-staging/tests.html

[10] M. A. Morales and J. M. Halpern, "Guide to Selecting a Biorecognition Element for Biosensors," *Bioconjug Chem,* vol. 29, no. 10, pp. 3231-3239, Oct 17 2018, doi: 10.1021/acs.bioconjchem.8b00592.

[11] H. H. Nguyen, S. H. Lee, U. J. Lee, C. D. Fermin, and M. Kim, "Immobilized Enzymes in Biosensor Applications," *Materials (Basel),* vol. 12, no. 1, Jan 2 2019, doi: 10.3390/ma12010121.

[12] J. P. Chambers, B. P. Arulanandam, L. L. Matta, A. Weis, and J. J. Valdes, "Biosensor recognition elements," *Current Issues in Molecular Biology,* vol. 10, pp. 1-12, 2008.

[13] Q. Gui, T. Lawson, S. Shan, L. Yan, and Y. Liu, "The Application of Whole Cell-Based Biosensors for Use in Environmental Analysis and in Medical Diagnostics," *Sensors (Basel),* vol. 17, no. 7, Jul 13 2017, doi: 10.3390/s17071623.

[14] N. Gupta, V. Renugopalakrishnan, D. Liepmann, R. Paulmurugan, and B. D. Malhotra, "Cell-based biosensors: Recent trends, challenges and future perspectives," *Biosens Bioelectron,* vol. 141, p. 111435, Sep 15 2019, doi: 10.1016/j.bios.2019.111435.

[15] Q. Liu and P. Wang, *Cell-based biosensors: principles and applications*. Artech House, 2009.

[16] J. Wang, "Electrochemical nucleic acid biosensors," *Analytica chimica acta,* vol. 469, no. 1, pp. 63-71, 2002.

[17] A. Saadati *et al.*, "Recent advances on application of peptide nucleic acids as a bioreceptor in biosensors development," *TrAC Trends in Analytical Chemistry,* vol. 114, pp. 56-68, 2019, doi: 10.1016/j.trac.2019.02.030.

[18] G. Wu, R. H. Datar, K. M. Hansen, T. Thundat, R. J. Cote, and A. Majumdar, "Bioassay of prostate-specific antigen (PSA) using microcantilevers," *Nature biotechnology,* vol. 19, no. 9, pp. 856-860, 2001.

[19] D. Grieshaber, R. MacKenzie, J. Vörös, and E. Reimhult, "Electrochemical biosensors-sensor principles and architectures," *Sensors,* vol. 8, no. 3, pp. 1400-1458, 2008.

[20] I. H. Cho, D. H. Kim, and S. Park, "Electrochemical biosensors: perspective on functional nanomaterials for on-site analysis," *Biomater Res,* vol. 24, p. 6, 2020, doi: 10.1186/s40824-019-0181-y.

[21] H. Kumar and Neelam, "Enzyme-based electrochemical biosensors for food safety: a review," *Nanobiosensors in Disease Diagnosis,* 2016, doi: 10.2147/ndd.S64847.

[22] M. S. Belluzo, M. É. Ribone, and C. M. Lagier, "Assembling amperometric biosensors for clinical diagnostics," *Sensors,* vol. 8, no. 3, pp. 1366-1399, 2008.

[23] A. Mujahid, A. Afzal, and F. L. Dickert, "An Overview of High Frequency Acoustic Sensors-QCMs, SAWs and FBARs-Chemical and Biochemical Applications," *Sensors (Basel),* vol. 19, no. 20, Oct 11 2019, doi: 10.3390/s19204395.

[24] M. Pohanka, "Overview of Piezoelectric Biosensors, Immunosensors and DNA Sensors and Their Applications," *Materials (Basel),* vol. 11, no. 3, Mar 19 2018, doi: 10.3390/ma11030448.

[25] J. Suthar, E. S. Parsons, B. W. Hoogenboom, G. R. Williams, and S. Guldin, "Acoustic Immunosensing of Exosomes Using a Quartz Crystal Microbalance with Dissipation Monitoring," *Anal Chem,* vol. 92, no. 5, pp. 4082-4093, Mar 3 2020, doi: 10.1021/acs.analchem.9b05736.

[26] M. C. Dixon, "Quartz crystal microbalance with dissipation monitoring: enabling real-time characterization of biological materials and their interactions," *Journal of biomolecular techniques: JBT,* vol. 19, no. 3, p. 151, 2008.

[27] D. E. Gaddes, M. C. Demirel, W. B. Reeves, and S. Tadigadapa, "Remote calorimetric detection of urea via flow injection analysis," *Analyst,* vol. 140, no. 23, pp. 8033-40, Dec 7 2015, doi: 10.1039/c5an01306b.

[28] M. Yakovleva, S. Bhand, and B. Danielsson, "The enzyme thermistor--a realistic biosensor concept. A critical review," *Anal Chim Acta,* vol. 766, pp. 1-12, Mar 5 2013, doi: 10.1016/j.aca.2012.12.004.

[29] S. D. Gan and K. R. Patel, "Enzyme immunoassay and enzyme-linked immunosorbent assay," *J Invest Dermatol,* vol. 133, no. 9, p. e12, 2013.

[30] S. Zhang, A. Garcia-D'Angeli, J. P. Brennan, and Q. Huo, "Predicting detection limits of enzyme-linked immunosorbent assay (ELISA) and bioanalytical techniques in general," *Analyst,* vol. 139, no. 2, pp. 439-445, 2014.

[31] Abnova. ELISA Pairs Kits [Online] Available: http://www.abnova.com/support/resources.asp?switchfunctionid=%7B70196CA1-59B1-40D0-8394-19F533EB108F%7D

[32] G. G. Gutiérrez-Zúñiga and J. L. Hernández-López, "Sensitivity improvement of a sandwich-type ELISA immunosensor for the detection of different prostate-specific antigen isoforms in human serum using electrochemical impedance spectroscopy and an ordered and hierarchically organized interfacial supramolecular architecture," *Analytica chimica acta,* vol. 902, pp. 97-106, 2016.

[33] D. Quesada-González and A. Merkoçi, "Nanomaterial-based devices for point-of-care diagnostic applications," *Chemical Society Reviews,* vol. 47, no. 13, pp. 4697-4709, 2018.

[34] H. Inan *et al.*, "Photonic crystals: emerging biosensors and their promise for point-of-care applications," *Chemical Society Reviews,* vol. 46, no. 2, pp. 366-388, 2017.

[35] M. Alhajj and A. Farhana, "Enzyme Linked Immunosorbent Assay (ELISA)," in *StatPearls [Internet]*: StatPearls Publishing, 2020.

[36] A. D. Powers and S. P. Palecek, "Protein analytical assays for diagnosing, monitoring, and choosing treatment for cancer patients," *Journal of healthcare engineering,* vol. 3, 2012.

[37] G. Dutta and P. B. Lillehoj, "Wash-free, label-free immunoassay for rapid electrochemical detection of PfHRP2 in whole blood samples," *Sci Rep,* vol. 8, no. 1, p. 17129, Nov 20 2018, doi: 10.1038/s41598-018-35471-8.

[38] M. Zarei, "Advances in point-of-care technologies for molecular diagnostics," *Biosensors and Bioelectronics,* vol. 98, pp. 494-506, 2017.

[39] M. L. Sin, K. E. Mach, P. K. Wong, and J. C. Liao, "Advances and challenges in biosensor-based diagnosis of infectious diseases," *Expert review of molecular diagnostics,* vol. 14, no. 2, pp. 225-244, 2014.

[40] A. Salek-Maghsoudi *et al.*, "Recent advances in biosensor technology in assessment of early diabetes biomarkers," *Biosensors and Bioelectronics,* vol. 99, pp. 122-135, 2018.

[41] N. M. Noah and P. M. Ndangili, "Current Trends of Nanobiosensors for Point-of-Care Diagnostics," *J Anal Methods Chem,* vol. 2019, p. 2179718, 2019, doi: 10.1155/2019/2179718.

[42] C. Chen and J. Wang, "Optical biosensors: an exhaustive and comprehensive review," *Analyst,* vol. 145, no. 5, pp. 1605-1628, Mar 2 2020, doi: 10.1039/c9an01998g.

[43] S. Mariani and M. Minunni, "Surface plasmon resonance applications in clinical analysis," *Analytical and bioanalytical chemistry,* vol. 406, no. 9-10, pp. 2303-2323, 2014.

[44] J. F. Masson, "Surface Plasmon Resonance Clinical Biosensors for Medical Diagnostics," *ACS Sens,* vol. 2, no. 1, pp. 16-30, Jan 27 2017, doi: 10.1021/acssensors.6b00763.

[45] Biacore. Surface plasmon resonance-Technical note 1 [Online] Available: http://www.proteomics.iastate.edu/seminars/BIACore/TechnologyNotes/TechnologyNote1.pdf

[46] J. Homola, "Surface plasmon resonance sensors for detection of chemical and biological species," *Chemical reviews,* vol. 108, no. 2, pp. 462-493, 2008.

[47] B. A. Prabowo, A. Purwidyantri, and K. C. Liu, "Surface Plasmon Resonance Optical Sensor: A Review on Light Source Technology," *Biosensors (Basel),* vol. 8, no. 3, Aug 26 2018, doi: 10.3390/bios8030080.

[48] M. A. Cooper, "Optical biosensors in drug discovery," *Nature reviews Drug discovery,* vol. 1, no. 7, pp. 515-528, 2002.

[49] Y. Huang, H. Ho, S. Wu, and S. Kong, "Detecting phase shifts in surface plasmon resonance: a review," *Advances in Optical Technologies,* vol. 2012, 2012.

[50] X. Fan, I. M. White, S. I. Shopova, H. Zhu, J. D. Suter, and Y. Sun, "Sensitive optical biosensors for unlabeled targets: A review," *analytica chimica acta,* vol. 620, no. 1-2, pp. 8-26, 2008.

[51] M. De la Guardia and A. G. Illueca, *Food protected designation of origin: methodologies and applications*. Newnes, 2013.

[52] X. D. Hoa, A. Kirk, and M. Tabrizian, "Towards integrated and sensitive surface plasmon resonance biosensors: a review of recent progress," *Biosensors and bioelectronics,* vol. 23, no. 2, pp. 151-160, 2007.

[53] S. Roh, T. Chung, and B. Lee, "Overview of the characteristics of micro-and nano-structured surface plasmon resonance sensors," *Sensors,* vol. 11, no. 2, pp. 1565-1588, 2011.

[54] N. A. S. Omar *et al.*, "Quantitative and Selective Surface Plasmon Resonance Response Based on a Reduced Graphene Oxide-Polyamidoamine Nanocomposite for Detection of Dengue Virus E-Proteins," *Nanomaterials (Basel),* vol. 10, no. 3, Mar 21 2020, doi: 10.3390/nano10030569.

[55] P. Singh, "SPR Biosensors: Historical Perspectives and Current Challenges," *Sensors and Actuators B: Chemical,* vol. 229, pp. 110-130, 2016, doi: 10.1016/j.snb.2016.01.118.

[56] W. Wang *et al.*, "A label-free fiber optic SPR biosensor for specific detection of C-reactive protein," *Sci Rep,* vol. 7, no. 1, p. 16904, Dec 4 2017, doi: 10.1038/s41598-017-17276-3.

[57] Q. Liu, Y. Liu, S. Chen, F. Wang, and W. Peng, "A low-cost and portable dual-channel fiber optic surface plasmon resonance system," *Sensors,* vol. 17, no. 12, p. 2797, 2017.

[58] A. Bonyár, "Label-Free Nucleic Acid Biosensing Using Nanomaterial-Based Localized Surface Plasmon Resonance Imaging: A Review," *ACS Applied Nano Materials,* 2020, doi: 10.1021/acsanm.0c01457.

[59] D. Rho, C. Breaux, and S. Kim, "Label-Free Optical Resonator-Based Biosensors," *Sensors,* vol. 20, no. 20, 2020, doi: 10.3390/s20205901.

[60] M. D. Baaske, M. R. Foreman, and F. Vollmer, "Single-molecule nucleic acid interactions monitored on a label-free microcavity biosensor platform," *Nat Nanotechnol,* vol. 9, no. 11, pp. 933-9, Nov 2014, doi: 10.1038/nnano.2014.180.

[61] X.-C. Y. Bo-Qiang Shen, Yanyan Zhi, Li Wang, Donghyun Kim, Qihuang Gong, Yun-Feng Xiao, "Detection of Single Nanoparticles Using the Dissipative Interaction in a High-Q Microcavity," *Physical Review Applied,* vol. 5, no. 2, 2016, doi: 10.1103/PhysRevApplied.5.024011.

[62] A. F. G. Judith Su, Brian M Stoltz, "Label-free detection of single nanoparticles and biological molecules using microtoroid optical resonators," *Light, Science & Applications,* vol. 5, no. 1, 2016-01-01 2016, doi: 10.1038/lsa.2016.1.

[63] J. Su, "Label-Free Biological and Chemical Sensing Using Whispering Gallery Mode Optical Resonators: Past, Present, and Future," *Sensors (Basel),* vol. 17, no. 3, Mar 8 2017, doi: 10.3390/s17030540.

[64] M. R. Foreman, J. D. Swaim, and F. Vollmer, "Whispering gallery mode sensors," *Advances in optics and photonics,* vol. 7, no. 2, pp. 168-240, 2015.

[65] E. Primiceri *et al.*, "Key enabling technologies for point-of-care diagnostics," *Sensors,* vol. 18, no. 11, p. 3607, 2018.

[66] Z. Feng and L. Bai, "Advances of Optofluidic Microcavities for Microlasers and Biosensors," *Micromachines (Basel),* vol. 9, no. 3, Mar 9 2018, doi: 10.3390/mi9030122.

[67] M. Baaske and F. Vollmer, "Optical resonator biosensors: molecular diagnostic and nanoparticle detection on an integrated platform," *Chemphyschem,* vol. 13, no. 2, pp. 427-36, Feb 2012, doi: 10.1002/cphc.201100757.

[68] A. N. Nordin, "Optical-resonator-based biosensing systems: current status and future prospects," *Nanobiosensors in disease diagnosis,* vol. 5, p. 41, 2016.

[69] G. C. Righini and S. Soria, "Biosensing by WGM microspherical resonators," *Sensors,* vol. 16, no. 6, p. 905, 2016.

[70] M. Taleuzzaman, "Limit of Blank (LOB), Limit of Detection (LOD), and Limit of Quantification (LOQ)," *Organic and Medicinal Chemistry International Journal,* vol. 7, no. 5, p. 5, 2018, doi: 10.19080/OMCIJ.2018.07.555722.

[71] Y. V. H. Ricard Boqué. "The Limit of Detection." LCGC Europe. https://www.chromatographyonline.com/view/limit-detection (accessed 08/30/2020, 2020).

[72] P. Liu *et al.*, "An optofluidics biosensor consisted of high-finesse Fabry-Pérot resonator and micro-fluidic channel," *Applied Physics Letters,* vol. 100, no. 23, 2012, doi: 10.1063/1.4726188.

[73] H. Wu *et al.*, "An ultra-low detection-limit optofluidic biosensor based on all glass Fabry-Perot cavity," *Opt Express,* vol. 22, no. 26, pp. 31977-83, Dec 29 2014, doi: 10.1364/OE.22.031977.

[74] K. E. You, N. Uddin, T. H. Kim, Q. H. Fan, and H. J. Yoon, "Highly sensitive detection of biological substances using microfluidic enhanced Fabry-Perot etalon-based optical biosensors," *Sensors and Actuators B: Chemical,* vol. 277, pp. 62-68, 2018, doi: 10.1016/j.snb.2018.08.146.

[75] L. H. Chen *et al.*, "Fabry–Perot fiber-optic immunosensor based on suspended layer-by-layer (chitosan/polystyrene sulfonate) membrane," *Sensors and Actuators B: Chemical,* vol. 188, pp. 185-192, 2013, doi: 10.1016/j.snb.2013.06.093.

[76] T. Takahashi, T. Hizawa, N. Misawa, M. Taki, K. Sawada, and K. Takahashi, "Surface stress sensor based on MEMS Fabry–Perot interferometer with high wavelength selectivity for label-free biosensing," *Journal of Micromechanics and Microengineering,* vol. 28, no. 5, p. 054002, 2018.

[77] L. Tu, L. Huang, and W. Wang, "A novel micromachined Fabry-Perot interferometer integrating nano-holes and dielectrophoresis for enhanced biochemical sensing," *Biosens Bioelectron,* vol. 127, pp. 19-24, Feb 15 2019, doi: 10.1016/j.bios.2018.12.013.

[78] T. Zhang, Z. Gong, R. Giorno, and L. Que, "A nanostructured Fabry-Perot interferometer," *Optics express,* vol. 18, no. 19, pp. 20282-20288, 2010.

[79] C. Song, P. Deng, and L. Que, "Rapid multiplexed detection of beta-amyloid and total-tau as biomarkers for Alzheimer's disease in cerebrospinal fluid," *Nanomedicine,* vol. 14, no. 6, pp. 1845-1852, Aug 2018, doi: 10.1016/j.nano.2018.05.013.

[80] N. Gaber, Y. M. Sabry, M. Erfan, F. Marty, and T. Bourouina, "High-Q Fabry(-)Perot Micro-Cavities for High-Sensitivity Volume Refractometry," *Micromachines (Basel),* vol. 9, no. 2, Jan 31 2018, doi: 10.3390/mi9020054.

[81] T. Zhang, Y. He, J. Wei, and L. Que, "Nanostructured optical microchips for cancer biomarker detection," *Biosensors and Bioelectronics,* vol. 38, no. 1, pp. 382-388, 2012.

[82] R. Casquel *et al.*, "Engineering vertically interrogated interferometric sensors for optical label-free biosensing," *Analytical and Bioanalytical Chemistry,* pp. 1-13, 2020.

[83] Y. Guo, H. Li, K. Reddy, H. S. Shelar, V. R. Nittoor, and X. Fan, "Optofluidic Fabry–Pérot cavity biosensor with integrated flow-through micro-/nanochannels," *Applied Physics Letters,* vol. 98, no. 4, 2011, doi: 10.1063/1.3548673.

[84] E. P. Ivanova *et al.*, "Highly selective trapping of enteropathogenic E. coli on Fabry–Pérot sensor mirrors," *Biosensors and Bioelectronics,* vol. 35, no. 1, pp. 369-375, 2012.

[85] H. Zhu, J.-J. He, L. Shao, and M. Li, "Ultra-high sensitivity optical sensors based on cascaded two Fabry-Perot interferometers," *Sensors and Actuators B: Chemical,* vol. 277, pp. 152-156, 2018, doi: 10.1016/j.snb.2018.08.091.

[86] H. Zhang *et al.*, "Porous silicon optical microcavity biosensor on silicon-on-insulator wafer for sensitive DNA detection," *Biosens Bioelectron,* vol. 44, pp. 89-94, Jun 15 2013, doi: 10.1016/j.bios.2013.01.012.

[87] R. Caroselli, D. Martin Sanchez, S. Ponce Alcantara, F. Prats Quilez, L. Torrijos Moran, and J. Garcia-Ruperez, "Real-Time and In-Flow Sensing Using a High Sensitivity Porous Silicon Microcavity-Based Sensor," *Sensors (Basel),* vol. 17, no. 12, Dec 5 2017, doi: 10.3390/s17122813.

[88] P. Li *et al.*, "Spectrometer-free biological detection method using porous silicon microcavity devices," *Opt Express,* vol. 23, no. 19, pp. 24626-33, Sep 21 2015, doi: 10.1364/OE.23.024626.

[89] S. Li, J. Huang, and L. Cai, "A porous silicon optical microcavity for sensitive bacteria detection," *Nanotechnology,* vol. 22, no. 42, p. 425502, Oct 21 2011, doi: 10.1088/0957-4484/22/42/425502.

[90] T. V. N. Van Hoi Pham, The Anh Nguyen, Van Dai Pham and Huy Bui, "Nano porous silicon microcavity sensor for determination organic solvents and pesticide in water," *Advances in Natural Sciences: Nanoscience and Nanotechnology,* 2014.

[91] T. Cao, Y. Zhao, C. A. Nattoo, R. Layouni, and S. M. Weiss, "A smartphone biosensor based on analysing structural colour of porous silicon," *Analyst,* vol. 144, no. 13, pp. 3942-3948, 2019.

[92] P. Li, Z. Jia, and G. Lü, "Hydatid detection using the near-infrared transmission angular spectra of porous silicon microcavity biosensors," *Scientific Reports,* vol. 7, no. 1, pp. 1-8, 2017.

[93] F. S. Krismastuti, A. Cavallaro, B. Prieto-Simon, and N. H. Voelcker, "Toward Multiplexing Detection of Wound Healing Biomarkers on Porous Silicon Resonant Microcavities," *Adv Sci (Weinh),* vol. 3, no. 6, p. 1500383, Jun 2016, doi: 10.1002/advs.201500383.

[94] M. Zhang, Z. Jia, X. Lv, and X. Huang, "Biological detection based on the transmitted light image from a porous silicon microcavity," *IEEE Sensors Journal,* pp. 1-1, 2020, doi: 10.1109/jsen.2020.2985778.

[95] S. K. Ramakrishan, M. Martin Fernandez, T. Cloitre, V. Agarwal, F. J. G. Cuisinier, and C. Gergely, "Porous silicon microcavities redefine colorimetric ELISA sensitivity for ultrasensitive detection of autoimmune antibodies," *Sensors and Actuators B: Chemical,* vol. 272, pp. 211-218, 2018, doi: 10.1016/j.snb.2018.05.154.

[96] Y. Zhao, G. Gaur, S. T. Retterer, P. E. Laibinis, and S. M. Weiss, "Flow-Through Porous Silicon Membranes for Real-Time Label-Free Biosensing," *Anal Chem,* vol. 88, no. 22, pp. 10940-10948, Nov 15 2016, doi: 10.1021/acs.analchem.6b02521.

[97] M.-j. Yin, B. Gu, Q.-F. An, C. Yang, Y. L. Guan, and K.-T. Yong, "Recent development of fiber-optic chemical sensors and biosensors: Mechanisms, materials, micro/nano-fabrications and applications," *Coordination Chemistry Reviews,* vol. 376, pp. 348-392, 2018, doi: 10.1016/j.ccr.2018.08.001.

[98] A. B. Socorro-Leránoz, D. Santano, I. Del Villar, and I. R. Matias, "Trends in the design of wavelength-based optical fibre biosensors (2008–2018)," *Biosensors and Bioelectronics: X,* vol. 1, 2019, doi: 10.1016/j.biosx.2019.100015.

[99] Y. W. Huang, J. Tao, and X. G. Huang, "Research Progress on F-P Interference-Based Fiber-Optic Sensors," *Sensors (Basel),* vol. 16, no. 9, Sep 3 2016, doi: 10.3390/s16091424.

[100] X. Liu, M. Jiang, T. Dong, Q. Sui, and X. Geng, "Label-Free Immunosensor Based on Optical Fiber Fabry–Perot Interferometer," *IEEE Sensors Journal,* vol. 16, no. 20, pp. 7515-7520, 2016, doi: 10.1109/jsen.2016.2600632.

[101] X. Liu, M. Jiang, Q. Sui, S. Luo, and X. Geng, "Optical fiber Fabry–Perot interferometer for microorganism growth detection," *Optical Fiber Technology,* vol. 30, pp. 32-37, 2016, doi: 10.1016/j.yofte.2016.01.014.

[102] X. Wu, H. Liu, X. Wang, and H. Jiang, "Fiber-Optic Biological/Chemical Sensing System Based on Degradable Hydrogel," *IEEE Sensors Journal,* vol. 18, no. 1, pp. 45-52, 2018, doi: 10.1109/jsen.2017.2771398.

[103] M. S. Cano-Velazquez, L. M. Lopez-Marin, and J. Hernandez-Cordero, "Fiber optic interferometric immunosensor based on polydimethilsiloxane (PDMS) and bioactive lipids," *Biomed Opt Express,* vol. 11, no. 3, pp. 1316-1326, Mar 1 2020, doi: 10.1364/BOE.379518.

[104] C. Elosua *et al.*, "Micro and Nanostructured Materials for the Development of Optical Fibre Sensors," *Sensors (Basel),* vol. 17, no. 10, Oct 11 2017, doi: 10.3390/s17102312.

[105] R. Flores, R. Janeiro, and J. Viegas, "Optical fibre Fabry-Pérot interferometer based on inline microcavities for salinity and temperature sensing," *Scientific reports,* vol. 9, no. 1, pp. 1-9, 2019.

[106] S. Chen, Y. Liu, Q. Liu, and W. Peng, "Temperature-Compensating Fiber-Optic Surface Plasmon Resonance Biosensor," *IEEE Photonics Technology Letters,* vol. 28, no. 2, pp. 213-216, 2016, doi: 10.1109/lpt.2015.2492603.

[107] C.-B. Yu *et al.*, "Highly sensitive and selective fiber-optic Fabry-Perot volatile organic compounds sensor based on a PMMA film," *Optical Materials Express,* vol. 7, no. 6, pp. 2111-2116, 2017.

[108] R. Kanawade, A. Kumar, D. Pawar, D. Late, S. Mondal, and R. K. Sinha, "Fiber optic Fabry–Perot interferometer sensor: an efficient and fast approach for ammonia gas sensing," *JOSA B,* vol. 36, no. 3, pp. 684-689, 2019.

[109] R. Oliveira, L. Bilro, and R. Nogueira, "Fabry-Pérot cavities based on photopolymerizable resins for sensing applications," *Optical Materials Express,* vol. 8, no. 8, pp. 2208-2221, 2018.

[110] S. Kumaraswamy and R. Tobias, "Label-free kinetic analysis of an antibody–antigen interaction using biolayer interferometry," in *Protein-Protein Interactions*: Springer, 2015, pp. 165-182.

[111] I. Ziu, E. T. Laryea, F. Alashkar, C. G. Wu, and S. Martic, "A dip-and-read optical aptasensor for detection of tau protein," *Analytical and Bioanalytical Chemistry,* vol. 412, no. 5, pp. 1193-1201, 2020.

[112] R. L. Petersen, "Strategies Using Bio-Layer Interferometry Biosensor Technology for Vaccine Research and Development," *Biosensors (Basel),* vol. 7, no. 4, Oct 31 2017, doi: 10.3390/bios7040049.

[113] J. Wallner, G. Lhota, D. Jeschek, A. Mader, and K. Vorauer-Uhl, "Application of Bio-Layer Interferometry for the analysis of protein/liposome interactions," *J Pharm Biomed Anal,* vol. 72, pp. 150-4, Jan 2013, doi: 10.1016/j.jpba.2012.10.008.

[114] D. Verzijl, T. Riedl, P. Parren, and A. F. Gerritsen, "A novel label-free cell-based assay technology using biolayer interferometry," *Biosens Bioelectron,* vol. 87, pp. 388-395, Jan 15 2017, doi: 10.1016/j.bios.2016.08.095.

[115] G. L. Ciesielski, V. P. Hytonen, and L. S. Kaguni, "Biolayer Interferometry: A Novel Method to Elucidate Protein-Protein and Protein-DNA Interactions in the Mitochondrial DNA Replisome," *Methods Mol Biol,* vol. 1351, pp. 223-31, 2016, doi: 10.1007/978-1-4939-3040-1_17.

[116] S. Auer, T. Koho, H. Uusi-Kerttula, T. Vesikari, V. Blazevic, and V. P. Hytönen, "Rapid and sensitive detection of norovirus antibodies in human serum with a biolayer interferometry biosensor," *Sensors and Actuators B: Chemical,* vol. 221, pp. 507-514, 2015, doi: 10.1016/j.snb.2015.06.088.

[117] C. Rath *et al.*, "Comparison of different label-free imaging high-throughput biosensing systems for aptamer binding measurements using thrombin aptamers," *Anal Biochem,* vol. 583, p. 113323, Oct 15 2019, doi: 10.1016/j.ab.2019.05.012.

[118] A. Mechaly, H. Cohen, O. Cohen, and O. Mazor, "A biolayer interferometry-based assay for rapid and highly sensitive detection of biowarfare agents," *Anal Biochem,* vol. 506, pp. 22-7, Aug 1 2016, doi: 10.1016/j.ab.2016.04.018.

[119] V. Kamat and A. Rafique, "Designing binding kinetic assay on the bio-layer interferometry (BLI) biosensor to characterize antibody-antigen interactions," *Anal Biochem,* vol. 536, pp. 16-31, Nov 1 2017, doi: 10.1016/j.ab.2017.08.002.

[120] H. Muller-Esparza, M. Osorio-Valeriano, N. Steube, M. Thanbichler, and L. Randau, "Bio-Layer Interferometry Analysis of the Target Binding Activity of CRISPR-Cas Effector Complexes," *Front Mol Biosci,* vol. 7, p. 98, 2020, doi: 10.3389/fmolb.2020.00098.

[121] S. Gao *et al.*, "Enzyme-linked, aptamer-based, competitive biolayer interferometry biosensor for palytoxin," *Biosens Bioelectron,* vol. 89, no. Pt 2, pp. 952-958, Mar 15 2017, doi: 10.1016/j.bios.2016.09.085.

[122] S. Gao, X. Zheng, and J. Wu, "A biolayer interferometry-based competitive biosensor for rapid and sensitive detection of saxitoxin," *Sensors and Actuators B: Chemical,* vol. 246, pp. 169-174, 2017, doi: 10.1016/j.snb.2017.02.078.

[123] S. Gao *et al.*, "Gonyautoxin 1/4 aptamers with high-affinity and high-specificity: From efficient selection to aptasensor application," *Biosens Bioelectron,* vol. 79, pp. 938-44, May 15 2016, doi: 10.1016/j.bios.2016.01.032.

[124] H. Zhang, W. Li, H. Luo, G. Xiong, and Y. Yu, "Quantitative determination of testosterone levels with biolayer interferometry," *Chem Biol Interact,* vol. 276, pp. 141-148, Oct 1 2017, doi: 10.1016/j.cbi.2017.05.013.

[125] C. F. Markwalter, I. K. Jang, R. A. Burton, G. J. Domingo, and D. W. Wright, "Biolayer interferometry predicts ELISA performance of monoclonal antibody pairs for Plasmodium falciparum histidine-rich protein 2," *Anal Biochem,* vol. 534, pp. 10-13, Oct 1 2017, doi: 10.1016/j.ab.2017.07.010.

[126] A. Sultana and J. E. Lee, "Measuring protein-protein and protein-nucleic Acid interactions by biolayer interferometry," *Curr Protoc Protein Sci,* vol. 79, pp. 19 25 1-19 25 26, Feb 2 2015, doi: 10.1002/0471140864.ps1925s79.

[127] G. Lin and Y. K. Chembo, "Monolithic total internal reflection resonators for applications in photonics," *Optical Materials: X,* p. 100017, 2019, doi: 10.1016/j.omx.2019.100017.

[128] A. B. Matsko and V. S. Ilchenko, "Optical resonators with whispering-gallery modes-part I: basics," *IEEE Journal of Selected Topics in Quantum Electronics,* vol. 12, no. 1, pp. 3-14, 2006, doi: 10.1109/jstqe.2005.862952.

[129] C. Chen and J. Wang, "Optical biosensors: an exhaustive and comprehensive review," *The Analyst,* vol. 145, no. 5, pp. 1605-1628, 2020, doi: 10.1039/c9an01998g.

[130] Y. D. G. C. Righini, P. F´eron, M. Ferrari, G. Nunzi Conti, D. Ristic and S. Soria, "Whispering gallery mode microresonators: Fundamentals and applications," *La Rivista del Nuovo Cimento,* vol. 34, no. 7, p. 24, 2011, doi: 10.1393/ncr/i2011-10067-2.

[131] W. Pongruengkiat and S. Pechprasarn, "Whispering-Gallery Mode Resonators for Detecting Cancer," *Sensors (Basel),* vol. 17, no. 9, Sep 13 2017, doi: 10.3390/s17092095.

[132] L. Cai, J. Pan, and S. Hu, "Overview of the coupling methods used in whispering gallery mode resonator systems for sensing," *Optics and Lasers in Engineering,* vol. 127, p. 105968, 2020, doi: 10.1016/j.optlaseng.2019.105968.

[133] M. R. Foreman, J. D. Swaim, and F. Vollmer, "Whispering gallery mode sensors," *Adv Opt Photonics,* vol. 7, no. 2, pp. 168-240, Jun 30 2015, doi: 10.1364/AOP.7.000168.

[134] S. A. Iwao Teraoka, "Theory of resonance shifts in TE and TM whispering gallery modes by nonradial perturbations for sensing applications," *Journal of the Optical Society of America B,* vol. 23, no. 7, 2006, doi: 10.1364/JOSAB.23.001381.

[135] T. Reynolds *et al.*, "Dynamic Self-Referencing Approach to Whispering Gallery Mode Biosensing and Its Application to Measurement within Undiluted Serum," *Anal Chem,* vol. 88, no. 7, pp. 4036-40, Apr 5 2016, doi: 10.1021/acs.analchem.6b00365.

[136] Z. C. Zhenyi Xie, Yong Liu, Qingwen Zhang, Jun Zou, Liyang Shao, Yi Wang, Jianjun He, Mingyu Li, "Highly-sensitive optical biosensor based on equal FSR cascaded microring resonator with intensity interrogation for detection of progesterone molecules," *Optics Express,* vol. 25, no. 26, pp. 33193-33201, 2017, doi: 10.1364/OE.25.033193.

[137] H. Ghali, H. Chibli, J. L. Nadeau, P. Bianucci, and Y. A. Peter, "Real-Time Detection of Staphylococcus Aureus Using Whispering Gallery Mode Optical Microdisks," *Biosensors (Basel),* vol. 6, no. 2, p. 20, May 3 2016, doi: 10.3390/bios6020020.

[138] A. H. Tomoya Taniguchi, Takeshi Ikeda, Masataka Fukuyama, Yoshiteru Amemiya, Akio Kuroda, Shin Yokoyama, "Detection of antibody-antigen reaction by silicon nitride slot-ring biosensors using protein G," *Optics Communications,* vol. 365, pp. 16-23, 04/2016 2016, doi: 10.1016/j.optcom.2015.11.068.

[139] Y. G. Hao Li, Yuze Sun, Karthik Reddy, Xudong Fan, "Analysis of single nanoparticle detection by using 3-dimensionally confined optofluidic ring resonators," *Optics Express,* vol. 18, no. 24, pp. 25081-25088, 2010, doi: 10.1364/OE.18.025081.

[140] Z. Guo *et al.*, "Hyperboloid-Drum Microdisk Laser Biosensors for Ultrasensitive Detection of Human IgG," *Small,* vol. 16, no. 26, p. 2000239, 2020, doi: 10.1002/smll.202000239.

[141] M. de Goede *et al.*, "Al2O3:Yb(3+) integrated microdisk laser label-free biosensor," *Opt Lett,* vol. 44, no. 24, pp. 5937-5940, Dec 15 2019, doi: 10.1364/OL.44.005937.

[142] X. H. Rui Duan, Yanzeng Li, Hanyang Li, "Detection of acetylcholinesterase and its inhibitors by liquid crystal biosensor based on whispering gallery mode," *Sensors and Actuators B: Chemical,* vol. 308, 2020, doi: 10.1016/j.snb.2020.127672.

[143] R. Duan, Y. Li, H. Li, and J. Yang, "Detection of heavy metal ions using whispering gallery mode lasing in functionalized liquid crystal microdroplets," *Biomed Opt Express,* vol. 10, no. 12, pp. 6073-6083, Dec 1 2019, doi: 10.1364/BOE.10.006073.

[144] L. Fu, Q. Lu, X. Liu, X. Chen, X. Wu, and S. Xie, "Combining whispering gallery mode optofluidic microbubble resonator sensor with GR-5 DNAzyme for ultra-sensitive lead ion detection," *Talanta,* vol. 213, p. 120815, Jun 1 2020, doi: 10.1016/j.talanta.2020.120815.

[145] E. Ozgur *et al.*, "Ultrasensitive Detection of Human Chorionic Gonadotropin Using Frequency Locked Microtoroid Optical Resonators," *Analytical Chemistry,* vol. 91, no. 18, pp. 11872-11878, 2019, doi: 10.1021/acs.analchem.9b02630.

[146] Y. Wang, H. Zhang, Y. Cui, W. Lin, B. Liu, and D. Xiang, "Real-time conformational change monitoring of G-quadruplex using capillary-based biocompatible whispering gallery mode microresonator," *IEEE Sensors Journal,* pp. 1-1, 2020, doi: 10.1109/jsen.2020.3002913.

[147] U. S. Ying-Jen Chen, Chung-Hsuan (Benjamin) Huang, Frank Vollmer, "Combining Whispering-Gallery Mode Optical Biosensors with Microfluidics for Real-Time Detection of Protein Secretion from Living Cells in Complex Media," *Small Journal,* vol. 14, no. 22, 2018, doi: 10.1002/smll.201703705.

[148] E. Kim, M. D. Baaske, I. Schuldes, P. S. Wilsch, and F. Vollmer, "Label-free optical detection of single enzyme-reactant reactions and associated conformational changes," *Sci Adv,* vol. 3, no. 3, p. e1603044, Mar 2017, doi: 10.1126/sciadv.1603044.

[149] S. M. Rakesh Narang, Mehdi Mohammadi Ashani, Hamid Sadabadi, Hossein Hejazi, Mohammad Hossein Zarifi, Amir Sanati-Nezhad, "Sensitive, Real-time and Non-Intrusive Detection of Concentration and Growth of Pathogenic Bacteria using Microfluidic-Microwave Ring Resonator Biosensor," *Scientific Reports,* vol. 8, no. 1, 12-2018 2018, doi: 10.1038/s41598-018-34001-w.

[150] I. Brice, K. Grundsteins, A. Atvars, J. Alnis, R. Viter, and A. Ramanavicius, "Whispering gallery mode resonator and glucose oxidase based glucose biosensor," *Sensors and Actuators B: Chemical,* vol. 318, p. 128004, 2020, doi: 10.1016/j.snb.2020.128004.

[151] R. Duan, Y. Li, H. Li, and J. Yang, "Real-time monitoring of the enzymatic reaction of urease by using whispering gallery mode lasing," *Opt Express,* vol. 27, no. 24, pp. 35427-35436, Nov 25 2019, doi: 10.1364/OE.27.035427.

[152] S. S. Jonas Flueckiger, Valentina Donzella, Ahmed Sherwali, Daniel M. Ratner, Lukas Chrostowski, Karen C. Cheung, "Sub-wavelength grating for enhanced ring resonator biosensor," *Optics Express,* vol. 24, no. 14, p. 14, 2016/07/11 2016, doi: 10.1364/OE.24.015672.

[153] Y. Kim and H. Lee, "On-chip label-free biosensing based on active whispering gallery mode resonators pumped by a light-emitting diode," *Opt Express,* vol. 27, no. 23, pp. 34405-34415, Nov 11 2019, doi: 10.1364/OE.27.034405.

[154] R. S. M. Rizwana Khanum, Nayan Mani Das, "Observation of defect-assisted enhanced visible whispering gallery modes in ytterbium-doped ZnO microsphere," *Journal of Applied Physics,* vol. 121, no. 21, 2017-06-07 2017, doi: 10.1063/1.4984205.

[155] V. D. T. Yue Wang, Kheng Swee Leck, Beng Hau Ian Tan, Zeng Wang, Tingchao He, Claus-Dieter Ohl, Hilmi Volkan Demir, Handong Sun, "Robust Whispering-Gallery-Mode Microbubble Lasers from Colloidal Quantum Dots," *Nano Lett.,* vol. 17, no. 4, p. 6, 2017, doi: 10.1021/acs.nanolett.7b00447.

[156] K. S.-C. Lucía Labrador-Páez, Miguel Hernández-Rodríguez, Inocencio R. Martín, Tal Carmon, Leopoldo L. Martin, "Liquid whispering-gallery-mode resonator as a humidity sensor," *Optics Express,* vol. 25, no. 2, 01-2017 2017, doi: 10.1364/OE.25.001165.

[157] S. M. V. R. Anand, Boni Samuel, P. Radhakrishnan, M. Kailasnath, "Thermo-optic tuning of whispering gallery mode lasing from a dye-doped hollow polymer optical fiber," *Opt. Lett.,* vol. 42, no. 15, p. 4, 2017-08-01 2017, doi: 10.1364/OL.42.002926.

[158] A. Ahmed, J. V. Rushworth, N. A. Hirst, and P. A. Millner, "Biosensors for whole-cell bacterial detection," *Clin Microbiol Rev,* vol. 27, no. 3, pp. 631-46, Jul 2014, doi: 10.1128/CMR.00120-13.

[159] S. Berneschi *et al.*, "Optical whispering gallery mode resonators for label-free detection of water contaminants," *TrAC Trends in Analytical Chemistry,* vol. 126, p. 115856, 2020, doi: 10.1016/j.trac.2020.115856.

[160] K. Wada, Z. Zhou, L. Fu, S. Xie, Q. Lu, and X. Chen, "Label-free DNA detection based on whispering gallery mode optofluidic microcavity biosensor," presented at the Nanophotonics and Micro/Nano Optics IV, 2018. [Online]. Available: https://www.spiedigitallibrary.org/conference-proceedings-of-spie/10823/2501139/Label-free-DNA-detection-based-on-whispering-gallery-mode-optofluidic/10.1117/12.2501139.full.

[161] R. Duan, Y. Li, B. Shi, H. Li, and J. Yang, "Real-time, quantitative and sensitive detection of urea by whispering gallery mode lasing in liquid crystal microdroplet," *Talanta,* vol. 209, p. 120513, Mar 1 2020, doi: 10.1016/j.talanta.2019.120513.

[162] X. Zhang, L. Liu, and L. Xu, "Ultralow sensing limit in optofluidic micro-bottle resonator biosensor by self-referenced differential-mode detection scheme," *Applied Physics Letters,* vol. 104, no. 3, p. 033703, 2014, doi: 10.1063/1.4861596.

[163] P. Toren, E. Ozgur, and M. Bayindir, "Label-Free Optical Biodetection of Pathogen Virulence Factors in Complex Media Using Microtoroids with Multifunctional Surface Functionality," *ACS Sens,* vol. 3, no. 2, pp. 352-359, Feb 23 2018, doi: 10.1021/acssensors.7b00775.

[164] H. Wan, J. Chen, C. Wan, Q. Zhou, J. Wang, and Z. Zhang, "Optofluidic microcapillary biosensor for label-free, low glucose concentration detection," *Biomedical Optics Express,* vol. 10, no. 8, p. 3929, 2019, doi: 10.1364/boe.10.003929.

[165] T. A. Brooks and L. H. Hurley, "The role of supercoiling in transcriptional control of MYC and its importance in molecular therapeutics," *Nat Rev Cancer,* vol. 9, no. 12, pp. 849-61, Dec 2009, doi: 10.1038/nrc2733.

[166] A. C. Society. Survival rates for cancers [Online] Available: https://www.cancer.org/cancer/prostate-cancer/detection-diagnosis-staging/survival-rates.html
https://www.cancer.org/cancer/lung-cancer/detection-diagnosis-staging/survival-rates.html
https://www.cancer.org/cancer/bladder-cancer/detection-diagnosis-staging/survival-rates.html

[167] D. Rho, C. Breaux, and S. Kim, "Demonstration of a Low-Cost and Portable Optical Cavity-Based Sensor through Refractive Index Measurements," *Sensors (Basel)*, vol. 19, no. 9, May 12 2019, doi: 10.3390/s19092193.

[168] D. Rho, S. Cho, C. Joy, and S. Kim, "Demonstration of an optical cavity sensor with a differential detection method by refractive index measurements," in *2015 Texas Symposium on Wireless and Microwave Circuits and Systems (WMCS)*, 2015: IEEE, pp. 1-4.

[169] D. Rho and S. Kim, "Label-free real-time detection of biotinylated bovine serum albumin using a low-cost optical cavity-based biosensor," *Opt Express*, vol. 26, no. 15, pp. 18982-18989, Jul 23 2018, doi: 10.1364/OE.26.018982.

[170] D. Rho and S. Kim, "Large dynamic range optical cavity based sensor using a low cost three-laser system," *Conf Proc IEEE Eng Med Biol Soc*, vol. 2017, pp. 1393-1396, Jul 2017, doi: 10.1109/EMBC.2017.8037093.

[171] D. Rho and S. Kim, "Low-cost optical cavity based sensor with a large dynamic range," *Opt Express*, vol. 25, no. 10, pp. 11244-11253, May 15 2017, doi: 10.1364/OE.25.011244.

[172] C. Joy and S. Kim, "Benefits of a scaled differential calculation method for use in a Fabry-Perot based optical cavity biosensor," in *2017 Texas Symposium on Wireless and Microwave Circuits and Systems (WMCS)*, 2017: IEEE, pp. 1-4.

[173] S. Cho, J. H. Brake, C. Joy, and S. Kim, "Refractive index measurement using an optical cavity based biosensor with a differential detection," in *Optical Diagnostics and Sensing XV: Toward Point-of-Care Diagnostics*, 2015, vol. 9332: International Society for Optics and Photonics, p. 93320Z.

[174] V. S.-Y. Lin, K. Motesharei, K.-P. S. Dancil, M. J. Sailor, and M. R. Ghadiri, "A porous silicon-based optical interferometric biosensor," *Science*, vol. 278, no. 5339, pp. 840-843, 1997.

[175] S. Zhu, F. Pang, S. Huang, F. Zou, Y. Dong, and T. Wang, "High sensitivity refractive index sensor based on adiabatic tapered optical fiber deposited with nanofilm by ALD," *Optics Express*, vol. 23, no. 11, pp. 13880-13888, 2015.

[176] E. Özkumur *et al.*, "Quantification of DNA and protein adsorption by optical phase shift," *Biosensors and Bioelectronics*, vol. 25, no. 1, pp. 167-172, 2009.

[177] E. Ozkumur *et al.*, "Quantification of DNA and protein adsorption by optical phase shift," *Biosens Bioelectron*, vol. 25, no. 1, pp. 167-72, Sep 15 2009, doi: 10.1016/j.bios.2009.06.033.

[178] A. M. Hamed, "Image processing of corona virus using interferometry," *Optics and Photonics Journal*, vol. 6, no. 05, p. 75, 2016.

[179] L. Ma *et al.*, "Label-Free Analysis of Single Viruses with a Resolution Comparable to That of Electron Microscopy and the Throughput of Flow Cytometry," *Angewandte Chemie International Edition,* vol. 55, no. 35, pp. 10239-10243, 2016.

[180] Y. Pang, H. Song, and W. Cheng, "Using optical trap to measure the refractive index of a single animal virus in culture fluid with high precision," *Biomedical optics express,* vol. 7, no. 5, pp. 1672-1689, 2016.

[181] S. Satyanarayana, R. N. Karnik, and A. Majumdar, "Stamp-and-stick room-temperature bonding technique for microdevices," *Journal of Microelectromechanical Systems,* vol. 14, no. 2, pp. 392-399, 2005.

[182] J. Kim, E. C. Jensen, M. Megens, B. Boser, and R. A. Mathies, "Integrated microfluidic bioprocessor for solid phase capture immunoassays," *Lab on a Chip,* vol. 11, no. 18, pp. 3106-3112, 2011.

[183] X. Fan, *Advanced photonic structures for biological and chemical detection*. Springer, 2009.

[184] M. Zhu, M. Z. Lerum, and W. Chen, "How to prepare reproducible, homogeneous, and hydrolytically stable aminosilane-derived layers on silica," *Langmuir,* vol. 28, no. 1, pp. 416-23, Jan 10 2012, doi: 10.1021/la203638g.

[185] K. Wouters and R. Puers, "Diffusing and swelling in SU-8: insight in material properties and processing," *Journal of Micromechanics and Microengineering,* vol. 20, no. 9, p. 095013, 2010.

[186] C. Liu *et al.*, "Diffusion of water into SU-8 microcantilevers," *Physical Chemistry Chemical Physics,* vol. 12, no. 35, pp. 10577-10583, 2010.

[187] G. Hill *et al.*, "SU-8 MEMS Fabry-Perot pressure sensor," *Sensors and Actuators A: Physical,* vol. 138, no. 1, pp. 52-62, 2007.

[188] A. Qureshi, Y. Gurbuz, and J. H. Niazi, "Biosensors for cardiac biomarkers detection: A review," *Sensors and Actuators B: Chemical,* vol. 171-172, pp. 62-76, 2012, doi: 10.1016/j.snb.2012.05.077.

[189] Y. N. Yang, H. I. Lin, J. H. Wang, S. C. Shiesh, and G. B. Lee, "An integrated microfluidic system for C-reactive protein measurement," *Biosens Bioelectron,* vol. 24, no. 10, pp. 3091-6, Jun 15 2009, doi: 10.1016/j.bios.2009.03.034.

[190] W. M. Fakanya and I. E. Tothill, "Detection of the inflammation biomarker C-reactive protein in serum samples: towards an optimal biosensor formula," *Biosensors,* vol. 4, no. 4, pp. 340-357, 2014.

[191] A. E. Cetin *et al.*, "Handheld high-throughput plasmonic biosensor using computational on-chip imaging," *Light: Science & Applications,* vol. 3, no. 1, pp. e122-e122, 2014.

[192] S. Surdo, F. Carpignano, L. M. Strambini, S. Merlo, and G. Barillaro, "Capillarity-driven (self-powered) one-dimensional photonic crystals for refractometry and (bio) sensing applications," *RSC Advances,* vol. 4, no. 94, pp. 51935-51941, 2014.

[193] Z. Xu, K. Han, I. Khan, X. Wang, and G. L. Liu, "Liquid refractive index sensing independent of opacity using an optofluidic diffraction sensor," *Optics letters,* vol. 39, no. 20, pp. 6082-6085, 2014.

[194] F. Sequeira *et al.*, "Refractive index sensing with D-shaped plastic optical fibers for chemical and biochemical applications," *Sensors,* vol. 16, no. 12, p. 2119, 2016.

[195] F. Purr, M. Bassu, R. Lowe, B. Thürmann, A. Dietzel, and T. Burg, "Asymmetric nanofluidic grating detector for differential refractive index measurement and biosensing," *Lab on a Chip,* vol. 17, no. 24, pp. 4265-4272, 2017.

[196] J. Yang *et al.*, "In-fiber refractive index sensor based on single eccentric hole-assisted dual-core fiber," *Optics Letters,* vol. 42, no. 21, pp. 4470-4473, 2017.

[197] B. Yang, B. Yang, J. Zhang, Y. Yin, Y. Niu, and M. Ding, "A Sensing Peak Identification Method for Fiber Extrinsic Fabry–Perot Interferometric Refractive Index Sensing," *Sensors,* vol. 19, no. 1, p. 96, 2019.